

Theory of Thermal Conductivity

vorgelegt von

M. Sc.
Hagen-Henrik Kowalski

an der Fakultät II – Mathematik und Naturwissenschaften
der Technischen Universität Berlin
zur Erlangung des akademischen Grades

Doktor der Naturwissenschaften
Dr. rer. nat.

genehmigte Dissertation

Promotionsausschuss:
Vorsitzender: Prof. Dr. Mario Dähne
Gutachter: Prof. Dr. Andreas Knorr
Gutachter: Prof. Dr. Matthias Scheffler

Tag der wissenschaftlichen Aussprache: 30. November 2022

Berlin 2023

Erklärung der Urheberschaft

Ich erkläre hiermit an Eides statt, dass ich die vorliegende Arbeit ohne Hilfe Dritter und ohne Benutzung anderer als der angegebenen Hilfsmittel angefertigt habe; die aus fremden Quellen direkt oder indirekt übernommenen Gedanken sind als solche kenntlich gemacht. Die Arbeit wurde bisher in gleicher oder ähnlicher Form in keiner anderen Prüfungsbehörde vorgelegt und auch noch nicht veröffentlicht.

Ort, Datum

Unterschrift

Acknowledgements

I first want to thank Christine Müller without her by my side I would not have been able to finish this work. As my deepest support, and my harshest critic she guided the way whenever I lost it and helped me to push through the hardest of problems. Next, I thank Christian Carbogno who shaped my scientific understanding and supported my research endeavors where he could. I was in the unique position of having a second close mentor in Mariana Rossi who helped wrap my head around the world of Path Integrals. Moreover, I want to thank Matthias Scheffler who gave me the opportunity to do my research at a world-leading institution. Finally, I want to thank Emre Ahmetcik who has been my closest friend for more than 20 years. His never-wavering and unconditional support was and remains invaluable

The career of a young theoretical physicist consists of treating the harmonic oscillator
in ever-increasing levels of abstraction.

Sydney Coleman

Abstrakt

Bisher ist wenig über das Zusammenspiel von Kern-Quanten-Fluktuationen (QNFs) und starken anharmonischen Effekten bei Berechnungen der Wärmeleitfähigkeit bekannt: Störungsformalismen berücksichtigen typischerweise QNFs, berücksichtigen aber nur die führende anharmonische Ordnung und sind daher vermutlich nur im Tieftemperaturbereich gültig. Umgekehrt umfassen die üblichen Molekulardynamikansätze (MD) alle klassisch zugänglichen Ordnungen der Anharmonizität, ignorieren aber die QNFs. In dieser Arbeit quantifizieren wir die klassischen und quantitativen anharmonischen Beiträge zur Kernbewegung, indem wir ab initio MD- und ab initio path-integral MD (PIMD)-Simulationen im Hinblick auf ein Anharmonizitätsmaß analysieren. Zu diesem Zweck haben wir das Anharmonizitätsmaß auf den pfadintegralen Formalismus erweitert. Unsere Berechnungen zeigen, dass weder QNFs noch anharmonische Effekte im Allgemeinen vernachlässigbar sind, insbesondere im Fall von weichen Bindungen. Wir beginnen die Diskussion, indem wir unseren Ansatz an Lennard-Jones-Argon und Tersoff-Silizium testen. Dies ermöglicht nicht nur ein schnelles Prototyping, sondern auch den Vergleich, wie Quantenkernfluktuationen die Anharmonizität in hoch anharmonischen bzw. harmonischen Systemen verändern. Weitere ab initio-Berechnungen werden für Lithiumhydrid und Dünnschicht-Pentacen durchgeführt, die nicht nur wegen der hohen Schwingungsfrequenzen, sondern auch wegen ihrer industriellen Relevanz ausgewählt wurden. Diese Beispiele zeigen, dass anharmonische Beiträge, die ausschließlich von QNFs stammen, weit über die Raumtemperatur hinaus relevant sein können. Darüber hinaus führt eine große Nullpunktsbewegung zu starken anharmonischen Effekten, die über den Bereich der Störungstheorie hinausgehen, selbst bei 0 K. Tiefere qualitative Einblicke werden durch die Untersuchung der frequenz aufgelösten Anharmonizität gewonnen. Dabei zeigt sich, dass QNFs die Anharmonizität vor allem bei niederfrequenten Moden erhöhen. Anschließend erörtern wir die Auswirkungen dieser Erkenntnisse auf zuverlässige Wärmeleitfähigkeitsberechnungen. Schließlich leiten wir den Wärmestrom für (Thermostatted) Ring Polymer Dynamics und Centroid Molecular Dynamics ab und schlagen mögliche Verfeinerungsstrategien vor.

Abstract

To date, little is known about the interplay of nuclear-quantum fluctuations (QNFs) and strong anharmonic effects in thermal conductivity calculations: Perturbative formalisms typically account for QNFs, but consider only the leading anharmonic order, and are thus supposed to be valid in the low-temperature limit. Conversely, usual molecular dynamics (MD) approaches include all classical accessible orders of anharmonicity, but ignore QNFs. In this work, we quantify classical and quantum anharmonic contributions to nuclear motion by analyzing ab initio MD and ab initio path-integral MD (PIMD) simulations in terms of an anharmonicity measure [112]. To this end, we extended the anharmonicity measure to the path-integral formalism. Our calculations reveal that neither QNFs nor anharmonic effects are generally negligible, particularly in the case of soft bonding. We start the discussion by testing our approach on Lennard-Jones Argon and Tersoff Silicon. This not only allows for rapid prototyping but also allows for the comparison of how quantum nuclear fluctuations change the anharmonicity in highly anharmonic and harmonic systems respectively. Further ab initio calculations are performed for Lithium Hydride and thin-film Pentacene, chosen not only for the high vibrational frequencies but also the industrial relevance. These examples reveal that anharmonic contributions coming solely from QNFs can be relevant well beyond room temperature. Furthermore, large zero-point motion induces strong anharmonic effects beyond the realm of perturbation theory even at 0 K. Deeper qualitative insights are gained by investigating the frequency-resolved anharmonicity. This reveals that QNFs increase the anharmonicity dominantly at low-frequency modes. We then discuss the implications of these findings for reliable thermal conductivity calculations. Finally, we derive the heat flux for (Thermostatted) Ring Polymer Dynamics and Centroid Molecular Dynamics and suggest possible refinement strategies.

Contents

1	Introduction	13
2	Theory	17
2.1	Assessing and Describing the Potential-Energy Surface	18
2.1.1	Analytical Models for the Potential-Energy surface: Semi-Empirical Force Fields	19
2.1.2	Numerically determining the Potential-Energy Surface: First-Principles Methods	21
2.1.3	Including van der Waals Interaction	31
2.2	Nuclear Motion	32
2.2.1	The Harmonic Approximation	33
2.2.2	Anharmonic Effects	38
2.2.3	Equilibrium Molecular Dynamics: The Nuclei as a Classical Particle	44
2.2.4	The Quantum Canonical-Ensemble	46
2.2.5	The Path Integral Formalism	47
2.2.6	Sampling the Potential Energy Surface by Chance: Harmonic Sampling	55
2.2.7	Real Time Correlation Functions	58
2.3	Measuring Anharmonicity	62
3	The Interplay of Quantum Nuclear and Anharmonic Fluctuations	67
3.1	Validation of the Anharmonicity Score	67
3.1.1	Vibrational Properties of Tersoff Silicon	68
3.1.2	Vibrational Properties of Solid Lennard-Jones Argon	69
3.1.3	The Anharmonicity Score Tested on Tersoff Silicon and Lennard- Jones Argon	70
3.1.4	How does this Relate to the Thermal Conductivity	77
3.1.5	Lithium Hydrate	84
3.1.6	The Anharmonicity of Lithium Hydride	90
3.1.7	Thin Film Pentacene	93
3.1.8	The Anharmonicity of Thin-Film Pentacene	98
4	Going Beyond what is Currently Possible: Thermal Conductivity from Path Integral Based Methods	105
4.1	Deriving the Heat-Flux Estimator	105
4.1.1	The Heatflux	105

Contents

4.1.2	The (T)RPMD Heat Flux Estimator	106
4.1.3	The CMD Heat Flux Estimator	108
4.1.4	Outlook	109
5	Conclusion	113
	Bibliography	117
A	New CV estimator	125
B	Harmonic Analysis for Path Integral MD	127
C	Publications	133
C.1	Optimizations of the Eigensolvers in the ELPA Library: Testing Autotuning under Production Conditions	133
C.1.1	A Parallel Solver for the Generalized Eigenvalue Problem: Optimized GPU Offloading from Autotuning	135
D	Thermostats	137
D.1	Classical	137
D.1.1	Nose-Hoover Thermostat	137
D.1.2	Langevin Thermostat	137
D.1.3	Stochastic Velocity Rescaling Thermostat	138
D.2	Quantum	139
D.2.1	Path Integral Langevin Dynamics	139

1 Introduction

Materials science is a key field in today's world that lays the foundation for enabling better or even completely new technologies. Examples cover nearly all aspects of our life and include emissive display technologies, based on organic light-emitting diodes (OLED) [151], as well as fundamental advances that are crucial for the transport industry as a whole, such as thermal barrier coating, which is necessary for the development of efficient turbines [5] in airplanes. Substantial efforts have also been made toward the recuperation of electric energy from otherwise wasted heat via the thermoelectric effect [4].

To this end, computational materials science has become a key ingredient to achieving these goals. In particular, high-throughput formalisms that enable scanning over material space in an efficient fashion, i.e., without requiring a tedious syncretization of the compounds of interest, have gained a lot of traction in this regard. This led to the advent of large material databases like the *Materials Project* or *NOMAD-Repository*. At the core is the *Findable, Accessible, Interoperable, and Re-purposable* (FAIR) paradigm, to facilitate cooperation progress across the entire field of material research. This is achieved by making the data platform-agnostic, thus removing the barrier artificially imposed by different standards, and easy to understand and use. Furthermore, this search can nowadays be further accelerated by machine-learning-based algorithms. Such ML methods can be trained on the existing data present in the aforementioned databases. In turn, even faster predictions that largely avoid running first-principles calculations could be achieved. Descriptor-based approaches like sure independence screening and sparsifying operator [7] (Sisso) for example, have successfully been applied in the classification of Perovskites [7] of Oxides and Halides. Conversely, Neural Networks allow for accurate representations of interatomic potentials [9]. Other approaches to learning interatomic potentials rely on Kernel-Ridge Regression [10] and show great enough accuracy to reliably predict the thermal conductivity of Zirconia.

For the challenges outlined above, it is essential that the employed computational techniques achieve predictive accuracy in the prediction of macroscopic material properties. This includes not only accurately describing electronic properties like band structures, which are essential to the description of optical properties, but also an accurate description of the nuclear dynamics. The latter determines many essential material properties. For instance, the specific heat measures the temperature increase due to the supplied energy per unit mass. This increases the system's internal energy which increases the nuclear displacements. If a compound exhibits multiple minima at different nuclear configurations,

1 Introduction

different structures can be observed. Additionally, the nuclear motion weakens chemical bonds and thus causes the crystal lattice to expand. The instantaneous energy of an atom is also not constant but changes with time, i.e., energy is transported through the crystal. This causes an energy flux in the crystal, which can be visualized in frequency space as the Fourier transform of its autocorrelation function.

In this field, substantial progress has been made over the last decades, in particular, this holds for two at first sight subtle, but in practice very important effects: Anharmonic and Quantum-Nuclear Fluctuations, as summarized below.

Anharmonicity In the harmonic approximation, the potential-energy surface is approximated by a Taylor expansion truncated at the second order, whereby this expansion is done in terms of the atomic displacements around their equilibrium positions. In Fourier space the associated equations of motion analytically reduce to an eigenvalue problem, which is solved by the eigenfrequencies of the system. The vibrational modes are given by sine and cosine functions for which the time evolution is fully determined by the initial conditions of the equations of motion. Accordingly, we easily can find analytical expressions for the vibrational spectra, specific heat capacity, free energy, and entropy. Importantly, these analytical expressions are not only known for classical but also for quantum harmonic oscillators. That, together with the comparatively low computational cost and availability of packages [91] to extract the necessary constants from standard density functional theory (DFT), made the harmonic approximation a widely used tool to investigate the dynamics of the nuclei.

However, not all material properties can be accurately captured by harmonic calculations. Additionally, phase transitions, temperature-dependent renormalizations, and other phenomena cannot be described by the harmonic approximation directly. However many mechanisms are even impossible to capture by describing the dynamics solely in terms of the harmonic approximation. These include thermal expansion, reaction rates, or heat transport. In these cases, additional orders in the Taylor expansion, i.e., 3rd and higher-order contributions to the PES description, need to be accounted for. In some cases, this even requires disregarding a Taylor expansion completely and to describe the dynamics of the PES exactly, e.g., by *ab initio* molecular dynamics methods. For instance, thermodynamic integration allows the calculation of the free-energy differences between two different states describes by the potentials V_1 and V_2 via the relation:

$$\Delta F(T) = \int_0^1 \langle V_2 - V_1 \rangle_T d\lambda. \quad (1.1)$$

Here λ is the coupling between both potentials $V(\lambda) = V_1 + \lambda(V_2 - V_1)$. Since the free energy determines the relative stability of different phases of matter, this approach naturally lends itself to the calculation of phase diagrams.

In this work, we will particularly focus on the problem of describing vibrational heat transport. The underlying physics cannot be described in the harmonic approximation alone, a fact that even eluded Erwin Schrödinger [1]. He was eventually proven wrong by Rudolf Peierls [2], who demonstrated that accounting for anharmonic effects is necessary to describe heat transport, i.e., the capability of a specific solid to conduct heat. Formally, it is described by the thermal conductivity tensor κ , which is defined through Fourier’s Law [107]:

$$\mathbf{J} = -\kappa \nabla T . \quad (1.2)$$

Here, κ serves as a proportionality constant between the temperature gradient ∇T and the heat flux \mathbf{J} , which naturally develops to contrast the temperature gradient and works to reestablish thermodynamic equilibrium.¹ Macroscopically, the heat flux is directly linked to the time-dependent occupation number of each vibrational mode. However, in the harmonic approximation, the occupation number is constant for all times and by extension the heat flux too. Accordingly, there can be no exchange of heat between modes in the harmonic approximation. However, any anharmonic contribution can be treated as a small perturbation to the harmonic system which forms the basis of some widely used methods to predict the thermal conductivity. By assuming that the occupation obeys the linearized Boltzmann transport equation [107] we can use the aforementioned perturbative approach to extract κ . In practise [92], the linearized Boltzmann transport equation is often approximated as a decay rate problem but iterative solvers and a recently published direct solution have also been described [108]. Perturbative methods are often the most accessible, despite the increased computational effort compared to the harmonic approximation, since the general approach to extracting the necessary constants is largely the same as in the harmonic approximation. Its cost can also be greatly alleviated by exploiting available degrees of symmetry. However, such an approach is insufficient especially for highly anharmonic materials which require a molecular dynamics approach. Here the fluctuation-dissipation theorem can be exploited to relate the heat flux autocorrelation to the thermal conductivity via the Green-Kubo relations [96, 97]. While this approach was long unfeasible via any DFT-based approach due to the prohibitively long time scales at which phonons decay. However recent breakthroughs made a DFT Green-Kubo implementation possible [95] by extrapolating to longer time scales and larger systems.

For the latter case, let us emphasize that such strongly anharmonic effects are often assumed to be only relevant at very high temperatures. This follows the argument that close to equilibrium, i.e., whenever the nuclear displacements are small, approximating the PES with a Taylor expansion (with or without higher-order corrections) should largely hold. While this qualitative argument is certainly true, little is known about its quantitative relevance in practical calculations. In other words, it is unclear how small the nuclear displacements have to be for this argument to hold, when and how this approximation

¹While in general lattice vibrations, electron transport, mass transport, and photons each contribute to the thermal conductivity κ , $\kappa_{\text{vibration}}$, i.e., the lattice thermal conductivity that stems from the vibration of the nuclei is by far dominant in semiconductors and insulators at non-incandescent temperatures [106].

breaks down, and how this varies across materials.

Quantum Nuclear Fluctuations Also due to their Fermionic character, electrons are often used as textbook examples for quantum-mechanical particles. Conversely, nuclei are often described classically, since the (thermal) de Broglie wavelength,

$$\lambda = \frac{2\pi\hbar}{p} \quad (1.3)$$

of an electron is 200 orders of magnitudes larger than the wavelength of the proton, which allows taking such an approximation in many cases. Nonetheless, quantum-nuclear fluctuations play a decisive role in solids when it comes to describing their dynamics. For instance, the specific heat is constant for classical nuclei while quantum-nuclear fluctuations lead to the characteristic T^3 dependence at lower temperatures. While this effect can be rationalized in the harmonic approximation, a concurrent description of quantum-nuclei and anharmonic effects is much more challenging. In the 1980s, path integral-based [68] approaches have been developed and successfully applied where QNFs and anharmonicity are equally important. Here a natural isomorphism between the classical partition function of a ring polymer and the quantum partition function is used. In practice, this requires running multiple classical or *ab initio* molecular dynamics simulations. For instance, such path integral methods have successfully been used to predict reaction rates [75] or diffusion coefficients [76].

Let us emphasize that generally quantum-nuclear fluctuations are regarded as being most important at low temperatures, at which the thermal de Broglie wavelength is larger. As is the case for the anharmonicity, such a qualitative argument certainly holds. Quantitatively, however, little is known to which extent QNFs remain relevant even at elevated temperatures and how this varies across different materials and compounds, especially in solids. In that case, the relevant quantity is not only the mass but also the strength of the interaction, which determines the shape of the vibrational potential. For instance, it was recently shown that such QNFs can affect the relative stability of polymers in molecular crystals [123].

As summarized above, QNFs are often assumed to be important in the low-temperature regime, but negligible at higher temperatures. Conversely, anharmonic effects are often thought to be essential to describe the high-temperature limit but to be irrelevant at low temperatures. In this work, we systematically explore to which extent these assumptions hold in realistic materials. A particular focus is laid on identifying those thermodynamic regions for which both QNFs and anharmonic effects are non-negligible and to discuss how the interplay of these two effects affects the prediction of macroscopic properties, in particular heat transport.

2 Theory

The quantum mechanical behavior of a non relativistic material with N_{el} electrons ($\mathbf{r} = \mathbf{r}_1, \dots, \mathbf{r}_{N_{\text{el}}}$) and N nuclei ($\mathbf{R} = \mathbf{R}_1 \dots \mathbf{R}_N$) is described by the Schödinger Equation:

$$\hat{H}(\mathbf{r}, \mathbf{R})\Psi(\mathbf{r}, \mathbf{R}) = E\Psi(\mathbf{r}, \mathbf{R}). \quad (2.1)$$

Here, $\Psi(\mathbf{r}, \mathbf{R})$ is the many-body wavefunction of the combined electronic-nuclear systems, $E(\mathbf{r}, \mathbf{R})$ its energy, and $H(\mathbf{r}, \mathbf{R})$ the Hamiltonian describing the behavior of the nuclei and the electrons [13]:

$$\hat{H}(\mathbf{r}, \mathbf{R}) = \hat{T}_{\text{el}} + \hat{T}_{\text{nuc}} + \hat{V}_{\text{el-nuc}}(\mathbf{r}, \mathbf{R}) + \hat{V}_{\text{el-el}}(\mathbf{r}) + \hat{V}_{\text{nuc-nuc}}(\mathbf{R}). \quad (2.2)$$

T_{el} and T_{nuc} are the kinetic energies of the electrons and the nuclei. With m_e and M_I being the respective masses (in contrast to the nuclei the electron mass is identical for all electrons and thus has no index). The real space expression of the kinetic energy operators is given by:

$$\hat{T}_{\text{el}} = -\frac{1}{2} \sum_i \frac{\nabla_{\mathbf{r}_i}^2}{m_e} \quad \text{and} \quad \hat{T}_{\text{nuc}} = -\frac{1}{2} \sum_I \frac{\nabla_{\mathbf{R}_I}^2}{M_I}. \quad (2.3)$$

The electrostatic electron-nuclei, electron-electron, and nuclei-nuclei interactions are described by the potential energy operators $V_{\text{el-nuc}}(\mathbf{r}, \mathbf{R})$, $V_{\text{el-el}}(\mathbf{r})$, and $V_{\text{nuc-nuc}}(\mathbf{R})$ defined in real space by:

$$\hat{V}_{\text{el-nuc}}(\mathbf{r}, \mathbf{R}) = - \sum_{i,I} \frac{Z_I}{|\mathbf{r}_i - \mathbf{R}_I|} \quad (2.4)$$

$$\hat{V}_{\text{el-el}}(\mathbf{r}) = \frac{1}{2} \sum_{i,j} \frac{1}{|\mathbf{r}_i - \mathbf{r}_j|} \quad (2.5)$$

$$\hat{V}_{\text{nuc-nuc}}(\mathbf{R}) = \frac{1}{2} \sum_{I,J} \frac{Z_I Z_J}{|\mathbf{R}_I - \mathbf{R}_J|}. \quad (2.6)$$

Here \mathbf{r}_i is the position of the i^{th} electron, and \mathbf{R}_I denotes the one of the I^{th} nucleus with charge Z_I . The combined electronic-nuclear systems is fully characterized through the solution of Eq. (2.1) given by the function $\Psi(\mathbf{r}, \mathbf{R})$. Solving Eq. 2.1, is however a formidable problem due to the coupling of the fast (electron) and slow (nuclei) degrees of freedom. Due to the much larger mass of the nucleus compared to the electrons ($M_I \gg m_e$) one can, in many cases, assume that the dynamics of the nuclei and electrons occur at different time scales. This should by no means imply that no (notable) exceptions [110,

111, 115, 116] exist in which this assumption is not valid. This is called the Born-Oppenheimer approximation [12] and it implies that the electrons adapt to every movement of the nucleus instantaneously, which allows to treat the electronic $\Psi_{\text{el}}(\mathbf{r}, \{\mathbf{R}\})$ and the nuclear system $\Psi_{\text{nuc}}(\mathbf{R})$ consecutively by approximating the full state in a product ansatz $\Psi(\mathbf{r}, \mathbf{R}) \approx \Psi_{\text{el}}(\mathbf{r}, \{\mathbf{R}\})\Psi_{\text{nuc}}(\mathbf{R})$. The curved brackets $\{\}$ denote that the positions of the nuclei enter the electronic wavefunction $\Psi_{\text{el}}(\mathbf{r}, \{\mathbf{R}\})$ only parametrically. Accordingly, two separated Schrödinger equations emerge, one governing the electronic degrees of freedom:

$$\underbrace{(\hat{T}_{\text{el}} + \hat{V}_{\text{el-nuc}}(\mathbf{r}, \{\mathbf{R}\}) + \hat{V}_{\text{el-el}}(\mathbf{r}))}_{H_{\text{el}}}\Psi_{\text{el}}(\mathbf{r}, \{\mathbf{R}\}) = E_{\text{el}}(\{\mathbf{R}\})\Psi_{\text{el}}(\mathbf{r}, \{\mathbf{R}\}). \quad (2.7)$$

The energy obtained from the electronic Schrödinger equation $E_{\text{el}}(\{\mathbf{R}\})$ subsequently determines the potential for the second Schrödinger equation describing the dynamics of the nuclei:

$$\underbrace{(T_{\text{nuc}} + V_{\text{nuc-nuc}}(\mathbf{R}) + E_{\text{el}}(\{\mathbf{R}\}))}_{H_{\text{nuc}}}\Psi_{\text{nuc}}(\mathbf{R}) = E_{\text{nuc}}\Psi_{\text{nuc}}(\mathbf{R}). \quad (2.8)$$

Numerical approaches to solve these equations are discussed in the following sections (electrons: Sec. 2.1.2; nuclei: Sec. 2.2).

2.1 Assessing and Describing the Potential-Energy Surface

The relevant equation describing the nuclear dynamics of solids is the nuclear Schrödinger Equation as presented in Eq. (2.8). However, this requires sufficient knowledge of the so-called potential-energy surface (PES) and thus of the solution of the electronic Schrödinger Equation (2.7). While the Born-Oppenheimer approximation significantly reduces the degrees of freedom, directly solving the electronic Schrödinger equation still presents a formidable task. Accordingly, further approximations are typically made which differ in accuracy and computational cost. Two different approaches will be used for different purposes in this work. Firstly semi-empirical potentials colloquially referred to as "force fields" (FFs), which approximate the potential-energy surface using analytical expressions depending on sets of material-specific parameters resulting in comparatively low computational cost. Accordingly, force fields allow the sampling of larger systems on long-time scales and, in the scope of this work, are utilized for prototyping and validation. Secondly, *ab initio* methods, in which the potential-energy surface is calculated by approximately solving Eq. (2.7) offer generally higher accuracy compared to force fields at significantly higher computational cost, restricting simulations to smaller systems and shorter time scales. However, due to their superior accuracy, *ab initio* methods are employed in this work to investigate Lithium Hydride and thin-film Pentacene.

2.1.1 Analytical Models for the Potential-Energy surface: Semi-Empirical Force Fields

In contrast to *ab-initio* methods, semi-empirical force-fields (FFs), solely describe the nuclei. Instead of generating the PES by solving the electronic problem for different configurations, semi-empirical force fields have a predefined functional form with free parameters. These parameters can then be determined from higher-level computational methods or experiments. The force fields relevant for this work are the Lennard-Jones potential, to describe solid Argon and the Tersoff potential to model diamond Silicon.

Lennard-Jones Potential

The Lennard-Jones Potential [51] certainly is one of the most studied and widely known force fields. It consists of an attractive term introduced by van der Waals interaction which leads to a functional form proportional to $\frac{1}{R^6}$ (for a more comprehensive explanation please see sec 2.1.3) and repulsive term due to the Pauli exclusion principle. In contrast to the attractive term, the functional form of the repulsive term is somewhat arbitrary, any term proportional to $\frac{1}{R^{n>6}}$ would suffice, however historically $n = 12$ is typically chosen and thus is proportional to $\frac{1}{R^{12}}$. Completely assembled the Lennard-Jones potential can be written as:

$$E^{\text{LJ}} = 4\epsilon \sum_I \left(\frac{\sigma^{12}}{|\mathbf{R}_I|^{12}} - \frac{\sigma^6}{|\mathbf{R}_I|^6} \right). \quad (2.9)$$

Here ϵ and σ are free parameters with the dimensions of energy and position respectively. The Lennard-Jones potential is designed for systems composed of atoms with closed shells, i.e. noble gases that bond almost exclusively through van der Waals interactions (exceptions such as Helium Hydrate exist). The numerical values to model Lennard-Jones argon were measured multiple times over the years for this work we used $\epsilon = 0.0103$ eV and $\sigma = 3.405$ Å taken from Ref. [128].

Tersoff Potential

Another well-established potential is the Tersoff potential [52] which was designed to describe covalent systems, specifically group IV semiconductors and their binaries [53]. Later it was also successfully parametrized for different group III-V compound semiconductors, notably gallium arsenide and indium arsenide [54]. Unlike the Lennard-Jones potential, the Tersoff potential is not a pure two-body potential but also includes three-body interactions, additionally accounting for bond order, however, interactions beyond the nearest-neighbor shell are neglected. Its functional form as implemented in the LAMMPS Molecular

2 Theory

Dynamics Simulator [143] is given by:

$$\begin{aligned}
E^{\text{Tersoff}} &= \frac{1}{2} \sum_I \sum_{J \neq I} V_{IJ} \\
V_{IJ} &= f_{\text{C}}(r_{IJ} + \delta)[f_{\text{R}}(r_{IJ} + \delta) + b_{IJ}f_{\text{A}}(r_{IJ} + \delta)] \\
f_{\text{C}} &= \begin{cases} 1, & r < R - D \\ \frac{1}{2} - \sin\left(\frac{\pi(r-R)}{2D}\right), & R - D < r < R + D \\ 0, & r > R + D \end{cases} \\
f_{\text{R}} &= Ae^{-\lambda_1 r} \\
f_{\text{A}} &= -Be^{-\lambda_2 r} \\
b_{IJ} &= (1 + \beta^n \zeta_{IJ}^n)^{-\frac{1}{2n}} \\
\zeta_{IJ} &= \sum_{K \neq I, J} (f_{\text{C}}(r_{IK} + \delta)g[\Theta_{IJK}(r_{IJ}, r_{IK})])e^{\lambda_3^2(r_{IJ} - r_{IK})^m} \\
g(\Theta) &= \gamma_{IJK} \left(1 + \left(\frac{c}{d}\right)^2 - \left(\frac{c^2}{d^2 + (\cos(\Theta) - \cos(\Theta_0))^2}\right)\right) \quad (2.10)
\end{aligned}$$

The two Morse potentials describe the pairwise attractive and repulsive interactions f_{R} and f_{A} while the bond-order term b_{IJ} weakens the attraction, taking bonding as well as anti-bonding orbitals into account. However, it fails to describe conjugated bonding partially caused by restricting all interactions to the nearest neighbor shell [55]. In total the Tersoff potential depends on 12 parameters which have to be fitted to experiments or *ab initio* calculations. For this work the parameters were taken from Ref. [53] as implemented into LAMMPS [143] to model the behavior of diamond Silicon. Most parameters are either only relevant for two-body, $n, \beta, \lambda_{1,2}$ (in $\frac{1}{\text{units of length}}$), A (in units of energy), and B (in units of energy) or three-body m (either 1 or 3), γ, λ_3 (in $\frac{1}{\text{units of length}}$), c, d , and Θ_0 interactions. Conversely R and D (both in units of length) define the cutoff distance and enter all interaction terms.

Other Force Fields

The Lennard-Jones and Tersoff potentials are by far not the only known force fields and the development of new ones remains an active field of research. Accordingly, over time, a large variety of different potentials has been published, each with varying degrees of accuracy, computational demand, and applicability. Especially the last point can present a major hurdle, for example, the REBO potential [55] improves on the Tersoff potential to better describe small hydrocarbon molecules however it lacks the capability to describe intermolecular interactions. To address this van der Waals interactions and torsion can be included which improves the accuracy for molecular crystals but decreases the accuracy for group IV semiconductors leading to "adequate" performance [56]. However, different increasingly complex force fields can indeed describe vastly different molecules and materials.

A notable example is ReaxFF [57], which not only offers high accuracy but is also capable of simulation bond breaking. However, this leads to a comparatively complex functional form. Driven by advances in the field of machine learning and artificial intelligence, other new force fields have been developed in recent years. Potential benefits include that the functional form does not have to be predetermined and increasing accuracy as the field matures. Gaussian Approximation Potentials (GAP) [58], for instance, employ Gaussian basis functions to approximate the potential energy surface. Recently the developers of the popular LAMMPS packages have begun implementing neural network interatomic potentials [59] which makes this approach readily available. Other implementations based on Kernel-Ridge Regression [10] and artificial neural networks [9] were successfully used in conjunction with *ab initio* methods to access time and size scales at or near *ab initio* accuracy. The Kernel-Based method has been implemented directly into the VASP [10] *ab initio* simulation package.

2.1.2 Numerically determining the Potential-Energy Surface: First-Principles Methods

In contrast to semi-empirical force fields *ab-initio* methods do not require the use of free parameters. Rather the electronic eigenvalue problem in Eq. (2.7) is solved under controlled approximations to obtain the forces.

Exchange and Correlation Energy

Two important concepts are those of exchange and correlation interactions. Exchange interaction arises due to the exchange symmetry of the wave function. A closed expression can be derived from the Fock space representation of $V_{\text{el-el}}$ by truncating the correlation expansion at the second-order or by equivalently approximating the eigenfunctions of the electronic Hamiltonian (Eq. (2.7)) by a single Slater determinant:

$$V_{\text{el-el}} \approx \underbrace{\frac{1}{2} \int \frac{n(\mathbf{r})n(\hat{\mathbf{r}})}{|\mathbf{r} - \hat{\mathbf{r}}|} d\mathbf{r}d\hat{\mathbf{r}}}_{\text{Hartree energy}} - \underbrace{\frac{1}{2} \sum_{i,j}^{N_{\text{el}}} \int \frac{\psi_i^*(\mathbf{r})\psi_j(\mathbf{r})\psi_j^*(\hat{\mathbf{r}})\psi_i(\hat{\mathbf{r}})}{|\mathbf{r} - \hat{\mathbf{r}}|} d\mathbf{r}d\hat{\mathbf{r}}}_{\text{exact exchange}}. \quad (2.11)$$

Here $n(\mathbf{r})$ is the electron density and ψ_i an eigenfunction of the free Hamiltonian. The Hartree energy is the classical Coulomb interaction and does not account for the Pauli exclusion principle. Conversely, the exact exchange interaction includes the Pauli exclusion. Correlation interaction is often defined as all interactions not included in the exact exchange¹. See Eq. (2.28) and following for a more in-depth analysis of these effects.

¹The exact exchange includes spin correlation.

Density Functional Theory

The *ab-initio* method of choice for this work is Density-Functional Theory (DFT). The original idea was developed by Walter Kohn and Pierre Hohenberg in the early 1960s. They found that the electronic ground state of a system is fully described by the respective electronic density

$$n(\mathbf{r}) = N_{\text{el}} \int |\Psi(\mathbf{r}, \mathbf{r}_2, \dots, \mathbf{r}_{N_{\text{el}}})|^2 d\mathbf{r}_2 \dots d\mathbf{r}_{N_{\text{el}}}, \quad (2.12)$$

which only depends on three cartesian coordinates. Formally, this massively reduces the complexity of the problem.

The essence of DFT is captured in the two Hohenberg-Kohn theorems [15]:

Theorem 2.1.1 (First HK-Theorem). *For any system of interacting particles in an external potential exists a bijection between the density and the external potential.*

Theorem 2.1.2 (Second HK-Theorem). *A functional $E_{\text{el}}[n]$ of the density exists, the density which minimizes this functional is the ground state density, and the minimum of this functional is the ground state energy.*

The functional $E_{\text{el}}[n]$ can be written as:

$$E_{\text{el}}[n] = E_{\text{ext}}[n] + F[n] \quad (2.13)$$

Here, $F[n]$ is the functional that contains all interactions between the electrons $V[n]$ as well as their kinetic energy $T[n]$ and takes the form

$$F[n] = T[n] + V[n]. \quad (2.14)$$

Finally $E_{\text{ext}}[n]$ is the interaction energy with an external potential. In our specific case, it is given by $V_{\text{el-nuc}}$ of Eq. (2.6)

$$E_{\text{ext}}[n] = \int v_{\text{ext}}(\mathbf{r})n(\mathbf{r})d\mathbf{r} = - \sum_I \int \frac{Z_I n(\mathbf{r})}{|\mathbf{r} - \mathbf{R}_I|} d\mathbf{r}. \quad (2.15)$$

Although formally exact, DFT is not particularly useful in this formulation, given that no closed analytical expression for $F[n]$ has been found so far, accordingly different approximations are developed to this day. Interestingly though the earliest examples, most notably the Thomas-Fermi [18, 19] (TF) and von Weizäcker [20] (vW) functionals derived in 1925 and 37 respectively, actually predate the discovery of the HK theorems. While both sought a solution to the electronic problem, their focus was on finding an approximation to the kinetic energy functional. Llewellyn Thomas and Enrico Fermi both independently

derived their functional by assuming a free-electron gas model in which the density is only slowly varying in space:

$$T_{\text{TF}} = c_0 \int n^{\frac{5}{3}} d\mathbf{r}. \quad (2.16)$$

The vW functional is a generalization of the TF functional and was derived from a spatially linearized one-electron wave function leading to a functional depending on the density gradient:

$$T_{\text{vW}} = -\frac{1}{2} \int \nabla \sqrt{n} \cdot \nabla \sqrt{n} d\mathbf{r}. \quad (2.17)$$

Direct approaches to numerically solve Eq. 2.14 are called orbital-free DFT. In practice this requires approximations to the unknown kinetic energy functional, however, the TF and vW functionals suffer from poor accuracy [21, 22]. More recent approximations are often based on perturbation theory² [24] or explicitly including non-locality [25]. Still even the most advanced functionals are only reliable for light metal alloys [24]. As discussed in the next section, these problems can be partially circumvented in the *Kohn-Sham formalism* [17]. This, however, requires dropping the formally appealing description in terms of an electron density and to reintroduce individual electronic states.

Kohn-Sham Formalism

The central idea of the *Kohn-Sham formalism* [17] is the introduction of a supplementary, **non-interacting** electronic system which can be described by single-particle states $\tilde{\psi}_1(\mathbf{r}), \dots, \tilde{\psi}_{N_{\text{el}}}(\mathbf{r})$. Before we discuss the mapping of the general problem we first illustrate the idea for a simplified non-interacting example. This constitutes a special case for which Eq. (2.13) is known exactly and the electron density is:

$$\tilde{n}(\mathbf{r}) = \sum_i^{N_{\text{el}}} |\tilde{\psi}_i(\mathbf{r})|^2 d\mathbf{r}. \quad (2.18)$$

Decomposing $F[\tilde{n}]$ using corollary 2.14 reveals:

$$F[\tilde{n}] = T[\tilde{n}] + V[\tilde{n}] = \tilde{T}_s[\tilde{n}]. \quad (2.19)$$

Here $\tilde{T}_s[\tilde{n}]$ is the kinetic energy functional of a **non-interacting** system. Accordingly the electronic energy functional reduces to:

$$\tilde{E}_{\text{el}}[\tilde{n}] = E_{\text{ext}}[\tilde{n}] + \tilde{T}_s[\tilde{n}]. \quad (2.20)$$

This includes only the external potential $E_{\text{ext}}[\tilde{n}]$, already defined in Eq. (2.15), and the **non-interacting** kinetic energy \tilde{T}_s (discussed in more detail below). The variational minimum of this functional is the ground state energy of the non-interacting system and

²The zeroth and second-order of the exact perturbation expansion of $T[n]$ are directly proportional to the TF and vW functional respectively. However, this expansion diverges after the 6'th order.

2 Theory

the corresponding density is the one of the ground state. The variational differential is given by:

$$\delta \left(\tilde{E}_{\text{el}}[\tilde{n}] - \mu \left[\int \tilde{n}(\mathbf{r}) d^3r - N_e \right] \right) = 0 \quad (2.21)$$

A Lagrange parameter μ was introduced to keep the number of particles fixed. This yields the following equation:

$$\frac{\delta \tilde{T}_s[\tilde{n}]}{\delta n} + v_{\text{ext}} = 0. \quad (2.22)$$

A direct solution would require the use of an approximate expression for the functional derivative $\delta \tilde{T}_s[\tilde{n}]/\delta n$. However, this can be circumvented by reintroducing the single-particle representation, given that for this particular system the kinetic energy is determined by the operator $\hat{T}_s = -\frac{1}{2} \sum_i^{N_{\text{el}}} \nabla^2$ the kinetic energy functional can be rewritten as:

$$\tilde{T}_s[\tilde{n}] = -\frac{1}{2} \sum_i^{N_{\text{el}}} \int \tilde{\psi}_i^* \nabla^2 \tilde{\psi}_i d\mathbf{r}. \quad (2.23)$$

Using this form of $\tilde{T}_s[\tilde{n}]$ allows to reformulate Eq. 2.22 in terms of functional derivatives of $\psi(\mathbf{r})$:

$$\frac{\delta \tilde{T}_s[\tilde{n}]}{\delta n} = -\frac{1}{2} \sum_i^{N_{\text{el}}} \int \frac{\delta \tilde{\psi}_i^*}{\delta n} \nabla^2 \tilde{\psi}_i d\mathbf{r} - \frac{1}{2} \sum_i^{N_{\text{el}}} \int \tilde{\psi}_i^* \nabla^2 \frac{\delta \tilde{\psi}_i}{\delta n} d\mathbf{r} = -v_{\text{ext}}. \quad (2.24)$$

This is fulfilled if all ψ_i^3 are solutions of the Schrödinger equation

$$\left(-\frac{1}{2} \nabla^2 + v_{\text{ext}}(\mathbf{r}) \right) \tilde{\psi}_i(\mathbf{r}) = \epsilon_i \tilde{\psi}_i(\mathbf{r}), \quad (2.25)$$

which can be solved at a reasonable computational cost, since the electrons are treated independently from each other. The electronic density calculated from its eigenfunctions is precisely the one of the systems ground state. More importantly taking the expectation value of Eq. (2.25) reveals an exact expression of $\tilde{T}_s[\tilde{n}]$:

$$\begin{aligned} \sum_i \int \tilde{\psi}_i^* (\hat{T}_s + v_{\text{ext}}) \tilde{\psi}_i d\mathbf{r} &= \sum_i \epsilon_i \\ \iff \sum_i \int \tilde{\psi}_i^* \hat{T}_s \tilde{\psi}_i d\mathbf{r} &= \sum_i \epsilon_i - \underbrace{\sum_I \int \frac{Z_I \tilde{n}(\mathbf{r})}{|\mathbf{r} - \mathbf{R}_I|} d\mathbf{r}}_{E_{\text{ext}}[\tilde{n}]} \\ \tilde{T}_s[\tilde{n}] &= \sum_i \epsilon_i - E_{\text{ext}}[\tilde{n}]. \end{aligned} \quad (2.26)$$

Finally combining this expression with Eq. 2.20 reveals the ground state energy:

$$\tilde{E}_{\text{el}} = \sum_i \epsilon_i - E_{\text{ext}}[\tilde{n}] + E_{\text{ext}}[\tilde{n}] = \sum_i \epsilon_i. \quad (2.27)$$

³The functional derivatives $\frac{\delta \tilde{\psi}}{\delta n}$ are distributions for which the second derivatives are defined as $\int \tilde{\psi}^* \nabla^2 \delta \tilde{\psi} / \delta n d\mathbf{r} = \int (\nabla^2 \tilde{\psi}^*) \delta \tilde{\psi} / \delta n d\mathbf{r}$

This result might seem obvious but this could not be further from the truth. In fact, this statement is only true since the associate Schrödinger equation is a linear differential equation⁴.

In the following, we now show how an interacting system can be mapped to a **non-interacting** one. For this purpose, the functional $F[n]$, has to be cast in a more practical form. Again starting from Eq. 2.14, we proceed in a similar way as before with the distinction that we also have to account for the exchange and correlation interactions between the electrons. Accordingly, we have to further decompose $T[n]$ and $V[n]$:

$$\begin{aligned} F[n] &= T[n] + V[n] \\ &= \tilde{T}_s[n] + E_H[n] + E_{xc}[n] \end{aligned} \quad (2.28)$$

Here the exchange correlation functional $E_{xc}[n]$ subsumes all exchange correlation interactions from the kinetic $T[n]$ and potential $V[n]$ energy functionals. The remaining contributions are the **non-interacting** kinetic energy $\tilde{T}_s[n]$ and electrostatic Hartree energy $E_H[n]$, describing electrostatic mean-field repulsion $E_H[n] = \frac{1}{2} \int \frac{n(\mathbf{r})n(\hat{\mathbf{r}})}{|\mathbf{r}-\hat{\mathbf{r}}|} d\mathbf{r}d\hat{\mathbf{r}}$. Inserted into Eq. (2.13) we can write the electronic energy functional of the interacting system in terms of an effectively **non-interacting** system in which $E_{\text{ext}}[n] + E_H[n] + E_{xc}[n] \hat{=} E_{\text{eff}}$ is identified as the external potential:

$$E_{\text{el}}[n] = \tilde{T}_s[n] + \underbrace{E_{\text{ext}}[n] + E_H[n] + E_{xc}[n]}_{E_{\text{eff}}[n]}. \quad (2.29)$$

This system is required⁵ to exhibit the exact same density as the interacting systems that is sought after:

$$n(\mathbf{r}) \stackrel{!}{=} \tilde{n}(\mathbf{r}) = \sum_i^{N_{\text{el}}} \int |\tilde{\psi}_i(\mathbf{r})|^2 d\mathbf{r}. \quad (2.30)$$

Minimizing this functional with respect to the density yields the following expression:

$$\frac{\delta \tilde{T}_s[n]}{\delta n} + \underbrace{v_{\text{ext}} + v_H + v_{xc}}_{v_{\text{eff}}(\mathbf{r})} = 0, \quad (2.31)$$

which takes the exact same form as the respective equation for a non-interacting system (2.22). By this means, we have found a mapping between the equation governing an interacting system in an external potential v_{ext} and the one of a non-interacting system in a different potential v_{eff} . Accordingly, also the **non-interacting** problem can be solved by finding the solution to the single-particle, **non-interacting** Schrödinger equation

$$\underbrace{\left(-\frac{1}{2}\nabla^2 + v_{\text{eff}}(\mathbf{r})\right)}_{h_{\text{KS}}} \psi_i(\mathbf{r}) = \epsilon_i \psi_i(\mathbf{r}). \quad (2.32)$$

⁴The Hamilton operator must neither depend on its eigenfunctions nor the associated densities.

⁵A detailed discussion of this so called *v-representability* requirement and its validity can be found in Ref. [16].

2 Theory

This equation is called the Kohn-Sham (KS) equation [17]. Again, it can be solved to determine the ground state density $n(\mathbf{r})$ within reasonable computational effort. In contrast to Eq. (2.25), however Eq. (2.32) is no longer a linear differential equation since the density itself enters $v_{\text{eff}}(\mathbf{r})$, so that a *self-consistent field* approach is typically used in practical calculations: Starting from an (educated) initial guess for the density $n^{(0)}(\mathbf{r})$, the electronic energy (see below) is minimized in i iterations by refining the density $n^{(i)}(\mathbf{r})$ until self-consistence is numerically achieved up to a user-defined parameter ϵ , e.g., $\int |n^{(i)}(\mathbf{r}) - n^{(i+1)}(\mathbf{r})| d\mathbf{r} < \epsilon$. However any practical application again requires an exact expression for $\tilde{T}_s[n]$, luckily the process is largely the same as for the non-interacting system:

$$\begin{aligned} -\sum_i \int \psi_i^* \nabla \psi_i d\mathbf{r} &= \sum_i \epsilon_i - \int v_{\text{eff}}[n_{\text{in}}] n(\mathbf{r}) d\mathbf{r} \\ \tilde{T}_s[n] &= \sum_i \epsilon_i - E_{\text{ext}}[n] - 2E_{\text{H}}[n] - \int v_{\text{xc}}[n] n(r) dr^3. \end{aligned} \quad (2.33)$$

Combined with Eq. (2.29) the electronic energy reads:

$$E_{\text{el}}[n] = \sum_i^{\text{occ}} \epsilon_i - E_{\text{H}}[n] - \int v_{\text{xc}}[n] n(r) dr^3 + E_{\text{xc}}[n]. \quad (2.34)$$

Please note that the electronic energy of the interacting systems is not just the sum of the eigenvalues! For the ground-state density, this yields the potential energy surface for the nuclei:

$$E_{\text{tot}} = E_{\text{el}}[n] + E_{\text{nuc}}. \quad (2.35)$$

For his works with Pierre Hohenberg and Lu Jeu Sham, Walter Kohn was ultimately awarded the Nobel Prize for Chemistry in 1998.

Approximative Exchange-Correlation Functionals

In principle, the previously introduced Kohn-Sham formalism provides a practical route to calculate the (exact) electronic ground state. However, a closed analytical form for the thereto required XC functional $E_{\text{xc}}[n]$ is not known, so approximative XC functionals have to be used in practical calculations instead. Different flavors with different levels of accuracy and computational cost exist: Here, we limit ourselves to introducing the concepts behind the approximations used for the calculations in this thesis; the influence of the approximations on the actual computational results are discussed for the practical examples of Lithium Hydride and thin-film Pentacene relevant for this work at a later point.

The Local Density Approximation (LDA): In this approximation, the XC energy density $\epsilon_{\text{xc}}[n]$ at each point in space \mathbf{r} is approximated by the value of the respective XC

energy density $\epsilon_{xc}^{LDA}[n]$ that a homogeneous electron gas (jellium model) would exhibit at that density $n(\mathbf{r})$ [17]:

$$E_{xc} = \int n(\mathbf{r})\epsilon_{xc}^{LDA}(n(\mathbf{r}))d\mathbf{r} . \quad (2.36)$$

The Generalized Gradient Approximation (GGA): In the spirit of a Taylor expansion, GGA XC functionals do not only take into account the local value of the density $n(\mathbf{r})$, but also its gradient $\nabla_{\mathbf{r}}n(\mathbf{r})$. Formally, this is achieved by introducing an enhancement factor $F_{xc}[n(\mathbf{r}), \nabla_{\mathbf{r}}n(\mathbf{r})]$:

$$E_{xc} = \int n(\mathbf{r})\epsilon_{xc}^{LDA}(n(\mathbf{r}))F_{xc}(n(\mathbf{r}), \nabla_{\mathbf{r}}n(\mathbf{r}))d\mathbf{r} . \quad (2.37)$$

Due to the fact that some freedom exists in the definition of $F_{xc}(n(\mathbf{r}), \nabla_{\mathbf{r}}n(\mathbf{r}))$, many different flavours of GGAs exist: Some, like the PBE functional [29] and its adaption for solid materials (PBEsol [30]) are formulated to fulfill fundamental properties that the exact XC functional is known to fulfill. Others, like BLYP are specifically constructed to reproduce experimental data.

Hybrid XC Functionals: Both LDA and GGAs suffer from a spurious self-interaction that results in the erroneous tendency of electrons to delocalize [31]. In part, this can be corrected for [32] by replacing a fraction of the GGA exchange with the exact (Hartree-Fock) exchange

$$E_x^{HF} = -\frac{1}{2} \sum_{i,j}^{N_{el}} \int \frac{\psi_i^*(\mathbf{r})\psi_j(\mathbf{r})\psi_j^*(\hat{\mathbf{r}})\psi_i(\hat{\mathbf{r}})}{\mathbf{r} - \hat{\mathbf{r}}} d\mathbf{r}d\hat{\mathbf{r}} . \quad (2.38)$$

Popular examples for such a functionals are the PBE0 functional [32]

$$E_{xc}^{PBE0} = \frac{1}{4}E_x^{HF} + \frac{3}{4}E_x^{PBE} + E_c^{PBE} \quad (2.39)$$

or HSE-type functionals [34], in which the bare Coulomb interaction in Eq. (2.38) is additionally screened.

Practical Numerical Solution and Implementation

In this section, we shortly summarize some practical aspects that need to be considered when performing KS calculations.

Solving the KS Equations: To efficiently implement Eq. (2.32) in computer code and exploit fast linear algebra libraries, the eigenfunctions ψ_i of the KS Hamiltonian are approximated in a truncated expansion in terms of basis functions ζ :

$$\psi_i = \sum_j c_{ij}\zeta_j(\mathbf{r}). \quad (2.40)$$

Accordingly, Eq. (2.32) becomes a generalized eigenvalue problem:

$$\sum_j h_{li} c_{ij} = \epsilon_i \sum_j o_{li} c_{ij} \quad (2.41)$$

With the matrix elements of the Kohn-Sham Hamiltonian h_{ks}

$$h_{li} = \int \zeta_l(\mathbf{r}) h_{ks} \zeta_i(\mathbf{r}) d\mathbf{r} \quad (2.42)$$

and the overlap integral

$$o_{li} = \int \zeta_l(\mathbf{r}) \zeta_i(\mathbf{r}) d\mathbf{r}. \quad (2.43)$$

These approximations, i.e., the convergence of the results of interest with respect to the functional, number of basis functions included, needs to be explicitly investigated to ensure the validity of the results.

In this particular work, the all-electron, full potential code *FHI-aims* [100] was used ⁶, which utilizes atom-centered, numeric orbitals

$$\zeta_j(\mathbf{r}) = \frac{u_{nl}(\mathbf{r} - \mathbf{R}_{at})}{r} Y_{lm}(\Phi, \Theta) \quad (2.44)$$

as basis set. Here $Y_{lm}(\Phi, \Theta)$ are spherical harmonics and $u_{nl}(\mathbf{r} - \mathbf{R}_{at})$ are numerically defined radial functions with \mathbf{R}_{at} being the coordinates of the nucleus to which this specific atomic orbital belongs.

Accelerating the Kohn-Sham Eigenvalue Problem: ELPA As discussed in the previous sections, the Kohn-Sham formalism requires solving a series of eigenproblems the cost of which scales cubically with the number of basis functions. For LDA and GGA exchange-correlation functionals, the generalized eigenvalue problem is the largest computational bottleneck when the number of basis functions is high. Accordingly, the development of faster and massively parallelized eigensolvers is a major priority to speed up DFT calculations for larger and more realistic systems. This led to a cooperation between the Bergische University Wuppertal, Technical University Munich, and the Max Planck Society to develop the "Eigenvalue Solvers For Petaflop Applications" (ELPA) library. It includes the eigensolver ELPA 1 [35] and its extension ELPA 2 [36]. ELPA 1 solves the generalised symmetric eigenvalue problem $\mathbf{h}\mathbf{c} = \epsilon\mathbf{o}\mathbf{c}$ in four steps:

- Step 1: Decompose \mathbf{o} into the product of a lower triangle matrix and its conjugate transpose (Cholesky decomposition).
- Step 2: Reducing the generalised symmetric eigenvalue problem to a equivalent symmetric eigenvalue problem using the Cholesky decomposition from Step 1.

⁶All-electron means that all electrons are treated on the same level. Conversely, pseudo-potential codes only treat the core electrons approximately by effectively including them in a pseudo-potential.

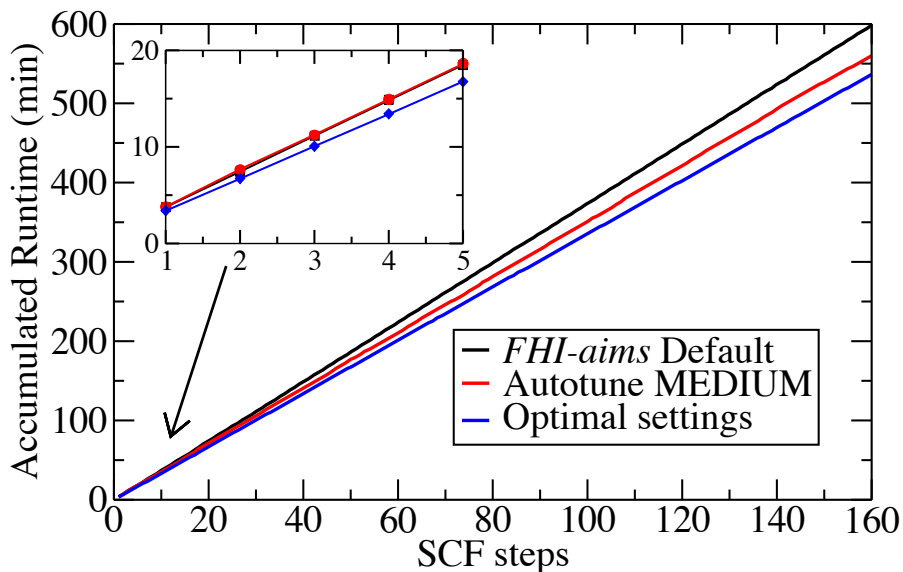


Figure 2.1: Accumulated run times for A-DNA for three different cases: FHI-aims default setting, MEDIUM level autotuning, and optimal settings as determined by autotuning.

- Step 3: Solve the symmetric eigenvalue problem.
- Step 4: Apply the inverse transformation to the eigenvectors, calculated in step 3.

For larger systems, the introduction of additional steps can be computational beneficial, as done in ELPA 2:

- Step 2.5: Transform the symmetric eigenvalue problem to a banded form and further into tridiagonal form.
- Step 3.5: Backtransformation of the eigenvectors.

The implementation of ELPA 1 and 2 scales exceptionally well with the number of CPU cores, furthermore GPU acceleration is also supported. ELPA 2 was further optimized to use the AVX instruction sets AVX, AVX2, and AVX512. Another functionality tailored to DFT applications is the Autotuning feature, during the SCF cycle all permitted modes are tested (e.g. ELPA 1 + GPU or ELPA 2 + AVX512) after which the most optimal setting is used for all subsequent SCF steps. To demonstrate the potential saving we generated ten geometries where the atomic positions were randomly displaced by fractions of Å. This simulates the variance of positions typically encountered in *ab initio* Molecular Dynamics simulations. We then performed DFT calculations using FHI-aims default setting, autotuning with the MEDIUM preset, and the optimal settings as determined by autotuning MEDIUM. The comparison in Fig. 2.1 demonstrates that, while autotuning introduces a slight computational overhead at the beginning of the simulation, the relative distance to the optimal settings becomes negligible for long simulations. We also found that the

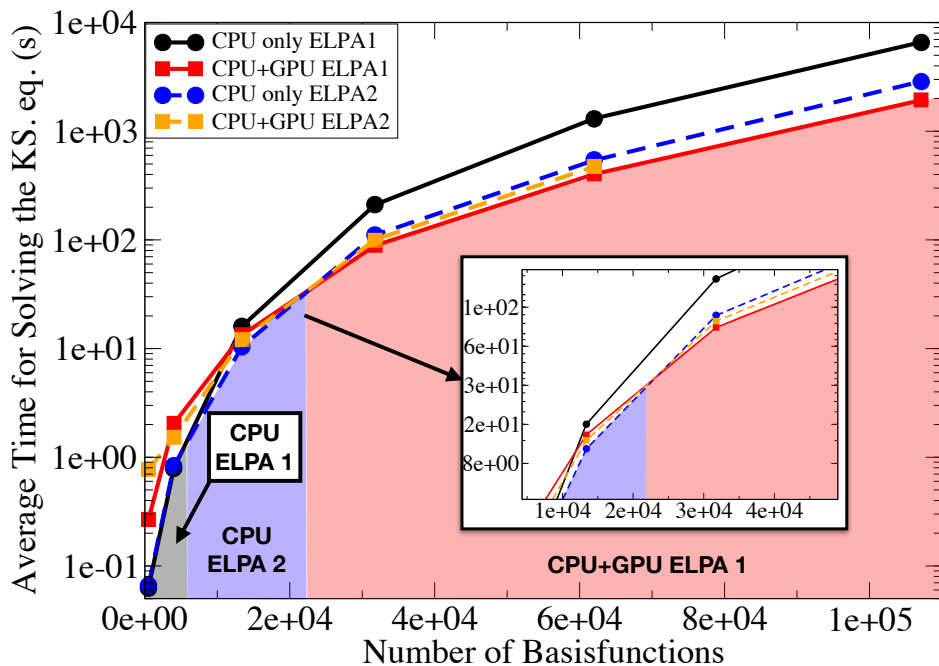


Figure 2.2: Computational time per SCF-step with increasing numbers of basis functions for CPU-only and CPU-GPU calculations. The shaded areas show the fastest settings.

optimal settings are transferable across differently displaced geometries. Accordingly, the computational overhead is negligibly compared to the performance gains [37]. Furthermore, we found that the combined CPU+GPU implementation (only some of the steps are GPU accelerated) leads to substantial performance gains if the number of basis functions is large enough [38]. However, the number of basis functions at which this "break-even" point occurs strongly depends on the number of nodes in use and decreases if fewer nodes are used. Importantly, for the results shown in Fig. ??, GPU acceleration was used for tridiagonalization, solution, and back transformation. For production calculations, it can be beneficial to limit the GPU accelerated to only a smaller subset of operations, which presents another application of autotuning. A more detailed description can be found in the Appendix of this work.

Periodic Boundary Conditions: Obviously, performing DFT calculations for macroscopic materials in a naive approach would be excruciatingly computationally expensive due to the massive number of electron N_{el} that needs to be accounted for. For crystalline materials with translational periodicity, this can be circumvented by applying *periodic boundary conditions*: As sketched in Fig. 2.3, a crystal is thereby described by a finite number of atoms in the primitive unit cell, which is spanned up by the lattice vectors $A = [\mathbf{A}_1, \mathbf{A}_2, \mathbf{A}_3]$. This unit cell is infinitely repeated as described by the translation vector $\mathbf{T}(\mathbf{n}) = A \cdot \mathbf{n}$ with $\mathbf{n} = [n_1, n_2, n_3]$, $n_i \in \mathbb{Z}$.

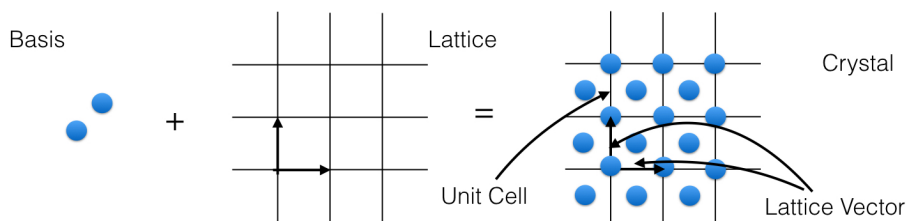


Figure 2.3: Sketch showing how a formally infinite crystal is modeled using periodic boundary conditions starting from a unit cell that contains basis atoms. This unit cell is infinitely repeated in space using the lattice vectors (see text).

Such a description in terms of periodic boundary conditions imposes restrictions on the wave functions, too. Bloch's theorem states that in this case the wave functions

$$\psi_i(\mathbf{r}, \mathbf{k}) = e^{i\mathbf{k}\cdot\mathbf{r}} u_i(\mathbf{r}) \quad (2.45)$$

can be written as the product of a lattice-periodic function

$$u_i(\mathbf{r}) = u_i(\mathbf{r} + \mathbf{T}(\mathbf{n})) \quad (2.46)$$

and a wave vector \mathbf{k} -dependent plane wave. In the case of periodic calculations in *FHI-aims*, this is exploited by using a Bloch-like nuclear atomic orbitals that fulfill Eq. (2.45)

$$\chi_j(\mathbf{r}, \mathbf{k}) = \sum_{\mathbf{n}} e^{i\mathbf{k}\cdot\mathbf{T}(\mathbf{n})} \zeta_j(\mathbf{r} - \mathbf{R}_{at} + \mathbf{T}(\mathbf{n})) \quad (2.47)$$

in the expansion in Eq. (2.40). Accordingly, both the KS states and KS Hamiltonian become \mathbf{k} -dependent. By this means, one thus formally maps the KS equation for an infinite number of electrons onto the KS equation for the finite number of electrons contained in a unit cell. In turn, however, this problem has to be solved for a formally infinite set of \mathbf{k} -vectors. Obviously, only finite \mathbf{k} -grid are used in practical calculations. Convergence of the quantities of interest with respect to this numerical parameter needs to be checked.

2.1.3 Including van der Waals Interaction

Van der Waals interaction is a weak attractive force between atoms. It arises due to quantum mechanical fluctuations of electron density inducing a momentarily existing dipole. Whilst these dipoles average out over time they still produce an electric field $\propto \frac{1}{\mathbf{R}^3}$ inducing a corresponding dipole on the other atoms. The resulting interaction between these dipoles gives rise to an attractive force. Its interaction energy is proportional

2 Theory

to $\frac{1}{R^6}$ and was already introduced in Sec. 2.1.1 as the attractive term in the Lennard-Jones potentials $\frac{\sigma^6}{R^6}$. Due to the long-ranged nature of these interactions they are not included in semi-local XC-functionals, which only account only for (semi-)local changes in $n(r)$.

Pairwise van der Waals interaction

A popular way to include vdW interaction into DFT is to add a pairwise energy term $E_{\text{vdW}} \propto \frac{C_6}{R^6}$ to the DFT energy [101] so to approximately including the missing long-range correlation energy. A practical form of this approximation is given by:

$$E_{\text{vdW}} = -\frac{1}{2} \sum_{AB} f_{\text{damp}}(R_{AB}, \mathbf{R}_A, \mathbf{R}_B) \frac{C_{6AB}}{R_{AB}^6} \quad (2.48)$$

Here C_{6AB} describes the pairwise interaction. Since long-range vdW interactions for nonoverlapping densities are missing, a Fermi type dampening function f_{damp} is included to eliminate spurious short-range interactions. A non-empirical way to obtain the necessary coefficient is given by the Tkatchenko-Scheffler method [102]. This method however neglects screening effects beyond the range of the electron density, since its two body vdW energy originates from "atomic" dipole fluctuations [103].

Many Body Dispersion

Including long-range screening effects is especially important for solids (and large molecules) since the electrostatic interaction between distant fluctuating dipoles decays not exponentially but via a power law. A method accounting for short and long-range screening is given by the Many-Body Dispersion [103, 104] extending the previously discussed Tkatchenko-Scheffler method. This is accomplished by modeling the surrounding of an atom as a dipole field and obtaining the polarizability matrix $A_{lm}(\omega) = \delta_{lm}\alpha_l(\omega)$. Here $\alpha_l(\omega)$ are frequency-dependent effective atomic polarizabilities. Finally, the long-range correlation energy can be calculated as:

$$E_{c,\text{MBDRsSCS}} = \frac{1}{2\pi} \int \text{Tr}(\ln(1 - A(\omega)T_{\text{LR}})d\omega \quad (2.49)$$

Where T_{LR} is the long-range dipole interaction tensor describing the strength of the interaction between different dipoles.

2.2 Nuclear Motion

Until this point we mainly focused on how solve the electronic problem (Eq. (2.7)) using DFT. However our goal is to explore the PES. Accordingly we need the forces acting on

the nuclei, which are given by the first derivative of the total energy E_{tot} . In DFT they can be obtained using the Hellman-Feynman Theorem.

$$\begin{aligned}\mathbf{F}_I &= -\frac{dE_{\text{tot}}}{d\mathbf{R}_I} \\ &= -\frac{\partial E_{\text{tot}}}{\partial \mathbf{R}_I} - \sum_i \frac{\partial E_{\text{tot}}}{\partial \chi_i} \frac{\partial \chi_i}{\partial \mathbf{R}_I} - \sum_{ij} \underbrace{\frac{\partial E_{\text{tot}}}{\partial c_{ij}}}_{=0} \frac{\partial c_{ij}}{\partial \mathbf{R}_I}.\end{aligned}\quad (2.50)$$

As highlighted by the notation $\partial/\partial \mathbf{R}_I$ for the *partial* derivatives, the first term describes the direct dependence of the total energy on the nuclear degrees of freedom. The second term, the so called *Pulay* term [39], captures the dependence of the total energy on the basis set chosen for the expansion in Eq. (2.44). The last term vanishes, since the ground state total energy constitutes a variational minimum with respect to the expansion coefficients c_{ij} . For higher order derivatives of the total energy, e.g., the Hessian,

$$\begin{aligned}\frac{d^2 E_{\text{tot}}}{d\mathbf{R}_I d\mathbf{R}_J} &= -\frac{d}{d\mathbf{R}_J} \mathbf{F}_I \\ &= -\frac{\partial \mathbf{F}_I}{\partial \mathbf{R}_J} - \sum_i \frac{\partial \mathbf{F}_I}{\partial \chi_i} \frac{\partial \chi_i}{\partial \mathbf{R}_J} - \sum_{ij} \underbrace{\frac{\partial \mathbf{F}_I}{\partial c_{ij}}}_{\neq 0} \frac{\partial c_{ij}}{\partial \mathbf{R}_J},\end{aligned}\quad (2.51)$$

the problem gets more complex, since the forces are *not* variational with respect to the expansion coefficients c_{ij} . Accordingly, a calculation of the Hessian does not only require the analytical derivatives appearing in the first two terms, but also the *response* of the expansion coefficients to a nuclear displacement $\partial c_{ij}/\partial \mathbf{R}_J$. Formally, the $(2n+1)$ theorem [46], i.e., a generalization of Hellman-Feynman theorem [47], shows that knowledge of the n -th order response (i.e. the n -th order total derivative) of the electronic structure with respect to a perturbation is required to determine the respective $(2n+1)$ -th total derivatives of the total energy [46]. These response quantities are, however, not directly accessible within DFT: They can be either computed by application of first order perturbation theory [87] or by evaluating the Hessian numerically with finite differences:

$$\frac{d^2 E_{\text{tot}}}{d\mathbf{R}_I d\mathbf{R}_J} \approx -\frac{F_I(\Delta \mathbf{R}_J)}{\Delta \mathbf{R}_J}\quad (2.52)$$

Conversely when using semi-empirical force fields (FF) the forces, and all other derivatives, can be obtained analytically. Often, however, interactions are formulated in curvilinear coordinates, accordingly, the derivatives become more complex⁷.

2.2.1 The Harmonic Approximation

The harmonic approximation is the most well-known and most used technique to describe and interpret the motion of the nuclei, especially in solid-state theory. To start, the PES

⁷All force-fields are Riemann manifolds (including \mathcal{R}^N) which require the use of covariant derivatives.

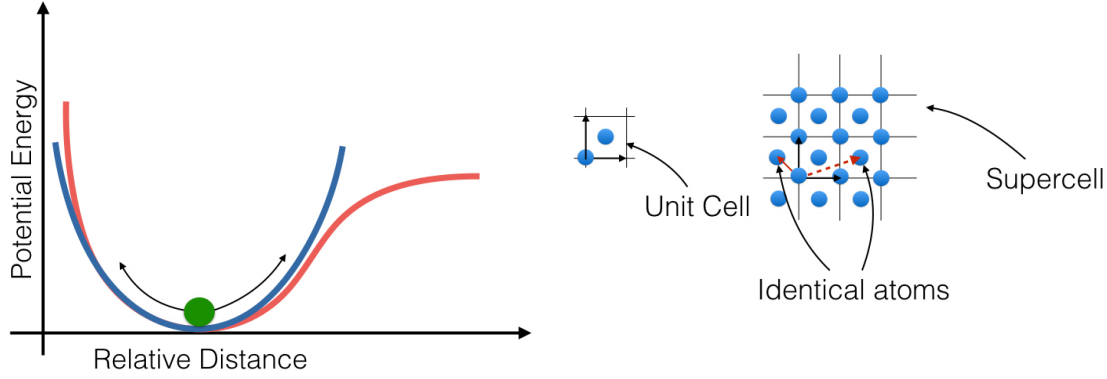


Figure 2.4: Left: Sketch showing a potential energy surface (red) that is approximated in the harmonic approximation (blue) around the equilibrium position. Right: Sketch of a supercell, the red arrows mark two periodic images that are connected to the respective primitive atom in the supercell via lattice vectors (see text)

is approximated by expanding it into a Taylor series around its minimum, i.e., the 0K equilibrium positions \mathbf{R}^{eq} shown in Fig. (2.4), truncated at the second order.

$$E_{tot}^{ha} \approx E_{tot} + \sum_{I,\alpha} F_I^\alpha u_I^\alpha + \frac{1}{2} \sum_{I,J,\alpha,\beta} \Phi_{IJ}^{\alpha\beta} u_I^\alpha u_J^\beta. \quad (2.53)$$

Here, the $u_I^\alpha = \mathbf{R}_I^\alpha - \mathbf{R}_I^{\alpha,eq}$ are the displacements of the atoms around their equilibrium positions. Please note that the static term E_{tot} is the total energy in equilibrium and that the linear term vanishes due to the fact that the forces F_I^α vanish in equilibrium. The Hessian (or harmonic force constants)

$$\Phi_{IJ}^{\alpha\beta} = \frac{\partial^2 E_{tot}}{\partial R_I^\alpha \partial R_J^\beta} \quad (2.54)$$

introduced in Eq. (2.53) above do not vanish (see Fig. 2.4). The ansatz

$$u_I^\alpha = \frac{A}{\sqrt{M_I}} \epsilon_I^\alpha(\mathbf{q}, s) e^{i(\mathbf{q} \cdot \mathbf{R}_I - \omega t)}, \quad (2.55)$$

the physical interpretation of which is discussed below, separates and solves the equation of motion in this approximate potential. In this context, it is useful to express the index of the I -th atom using periodic boundary conditions as $I \rightarrow n\tilde{I}$, where \tilde{I} denotes the \tilde{I} -th atom in the primitive unit cell and n denotes that this is its n -th periodic image shifted by a lattice translation vector $\mathbf{T}(n)$ (see Sec. 2.1.2). In this notation, the equations of motion become an eigenvalue problem

$$\mathbf{D}(\mathbf{q})\epsilon(\mathbf{q}) = \omega^2(\mathbf{q})\epsilon(\mathbf{q}) \quad \text{with} \quad D_{\tilde{I}\tilde{J}}^{\alpha\beta}(\mathbf{q}) = \sum_n \frac{\Phi_{(0\tilde{I})(n\tilde{J})}^{\alpha\beta}}{\sqrt{M_{\tilde{I}}M_{\tilde{J}}}} e^{i\mathbf{q} \cdot (\mathbf{R}_{(n\tilde{J})} - \mathbf{R}_{(0\tilde{I})})}. \quad (2.56)$$

Here, $\mathbf{D}(\mathbf{q})$ is the *dynamical matrix*, i.e., the Fourier transform of the mass-scaled force constants Φ with respect to the distance of periodic replicas. In practice, the sum can be truncated after a sufficiently high value for n since the interaction decays with the order $\mathcal{O}(1/R^2)$. This is done by constructing a supercell containing n images of the unit cell. The number of as well as which \mathbf{q} -points are accounted for is directly linked to the size of the supercell⁸. Accordingly, only phonon wavelengths commensurate (or more intuitively that fit into the supercell) with the supercell are included. The supercell is repeated periodically (see Fig. (2.4)). For a system with N atoms in the unit cell, we thus get $3N$ eigenvalues and -vectors at each reciprocal space point \mathbf{q} . Accordingly, the solution of the equations of motion is a superposition of harmonic oscillations

$$\mathbf{R}_I(t) = \mathbf{R}_I^{eq} + \text{Re} \left(\sum_{\mathbf{q},s} \frac{A_s(\mathbf{q})}{\sqrt{M_I}} \epsilon_{I,s}(\mathbf{q}) e^{i(\mathbf{q} \cdot \mathbf{R}_I - \omega_s(\mathbf{q})t)} \right) \quad (2.57)$$

with the complex amplitudes $A_s(\mathbf{q})$ and the wavevector \mathbf{q} . Please note that the amplitudes $A_s(\mathbf{q})$ and the respective occupation numbers $n_s(\mathbf{q}) = A_s^2(\mathbf{q})$ are **not** time-dependent and fully determined by the initial conditions, so that the individual oscillations are completely independent and decoupled. Accordingly, the motion is completely characterized by the eigenvectors and eigenfrequencies, i.e., the dispersion $\omega_s(\mathbf{q})$, which describes how the frequency of the phonon mode depends on its wavevector. Please note that also the derivative, i.e., the phonon group velocity

$$\mathbf{v}_s(\mathbf{q}) = \frac{\partial \omega_s(\mathbf{q})}{\partial \mathbf{q}} = \frac{1}{2\omega} \langle \epsilon_s(\mathbf{q}) | \frac{\partial D(\mathbf{q})}{\partial \mathbf{q}} | \epsilon_s(\mathbf{q}) \rangle \quad (2.58)$$

can be calculated directly from the dynamical matrix. An example for a phonon-band structure is given in Fig. 2.5. Here, the group velocity corresponds to the slope of the band structure.

Given that Eq. (2.56) is the analytic solution for the nuclear dynamics in the harmonic potential, also the thermodynamic partition function of the system

$$Z = \prod_{\mathbf{q},s} \frac{e^{-\frac{\hbar \omega_s(\mathbf{q})}{k_B T}}}{1 - e^{-\frac{\hbar \omega_s(\mathbf{q})}{k_B T}}} \quad (2.59)$$

can be calculated. From this expression quantities such as the free energy [91]

$$F^{ha} = -k_B T \ln(Z) = \frac{1}{2} \sum_{\mathbf{q},s} \hbar \omega_s(\mathbf{q}) + k_B T \sum_{\mathbf{q},s} \ln(1 - e^{-\frac{\hbar \omega_s(\mathbf{q})}{k_B T}}) \quad (2.60)$$

and the specific heat C_V

$$C_V = \frac{1}{V} \left(\frac{\partial E^{ha}}{\partial T} \right)_V = \frac{1}{V} \sum_{\mathbf{q},s} \hbar \omega_s(\mathbf{q}) \frac{\partial n_s^{eq}(\mathbf{q})}{\partial T} = \frac{1}{V} \sum_{\mathbf{q},s} c_s(\mathbf{q}) \quad (2.61)$$

⁸For example the primitive unit cell contains exactly one \mathbf{q} -point at Γ .

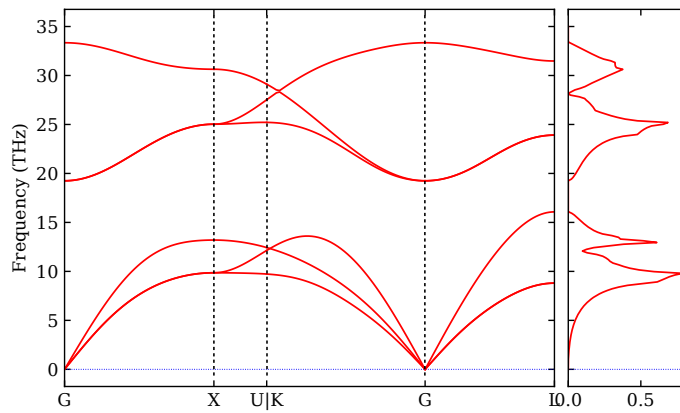


Figure 2.5: This figure shows an example of a phonon band structure with the corresponding density of states of Lithium Hydride, calculated using the PBEsol XC-functional.

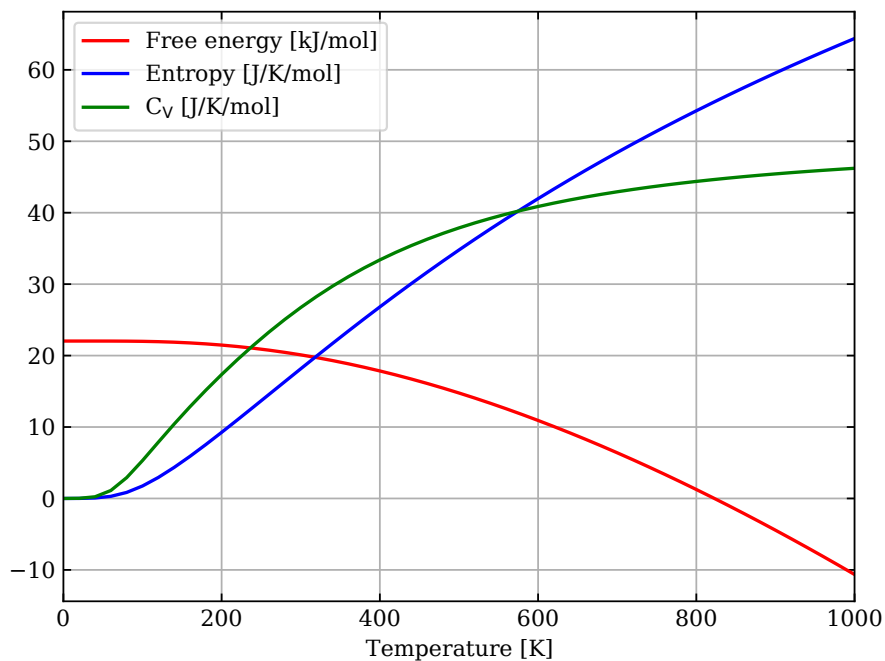


Figure 2.6: Vibrational free energy, entropy, and heat capacity of Lithium Hydride in the harmonic approximation, calculated using the PBEsol XC-functional.

can be calculated with E^{ha} being the harmonic energy

$$E^{ha} = \sum_{\mathbf{q},s} \hbar\omega_s(\mathbf{q}) \left(\frac{1}{2} + n_s^{eq}(\mathbf{q}) \right). \quad (2.62)$$

It is important to note that phonons, since they are bosonic quasi particles, obey the Bose-Einstein distribution

$$n_s^{eq}(\mathbf{q}) = \frac{1}{e^{\frac{\hbar\omega_s(\mathbf{q})}{k_B T}} - 1}. \quad (2.63)$$

At low temperatures, this causes the typical T^3 behavior of the specific heat (see Fig. (2.6)).

At elevated temperatures, C_V then approaches the classical, constant Dulong-Petit value $3Nk_b$ [106].

Most efficiently, equations such as (2.60) and (2.61) are numerically evaluated by introducing the phonon density of states

$$g(\omega) = \frac{1}{\Omega} \sum_s \int_{BZ} \delta(\omega - \omega_s(\mathbf{q})) d\mathbf{q}, \quad (2.64)$$

in which Ω denotes the volume of the Brillouin Zone. The thermodynamic expectation value Π for any operator $\pi(\omega_s(\mathbf{q}))$ that only implicitly depends on the wavevector \mathbf{q} can then be immediately evaluated using

$$\Pi = \frac{1}{\Omega} \sum_s \int_{BZ} \pi_s(\mathbf{q}) d\mathbf{q} = \int \pi(\omega) g(\omega) d\omega. \quad (2.65)$$

Fig. 2.5 also includes an example of a phonon density of states, the peaks occur at the frequencies where the band structure is most dense, e.g. in the case of localized flat modes.

Despite its usefulness, the harmonic approximation has severe limits. Due to the fact that the real PES is approximated close to the 0K equilibrium positions (see Fig.(2.4)), anharmonic effects become notable at higher temperatures when large displacements from equilibrium occur. Obviously, this is highly material dependent and one question answered in this thesis is exactly the quantification of anharmonicity for systems with pronounced quantum nuclear fluctuations e.g. at low temperatures.

Many effects are not described by the harmonic approximation at all, for example, the temperature-dependent renormalization of the phonon frequencies. For this reason, several methods to correct the shortcomings of the harmonic approximation have been developed.

- The Quasi Harmonic approximation: The quasi-harmonic approximation augments the harmonic approximation by explicitly accounting for the volume dependency of the Hessian [86]. This naturally leads to a renormalization of the band structure. It is the computational least expensive method and allows for the inclusion anharmonic effects such as thermal expansion. However, it is limited as for example the thermal conductivity cannot be directly extracted from it.

- Truncating the Taylor series at a higher order: This is the most obvious step to include anharmonicity. Higher-order force constants can either be determined from finite differences or in the case of DFT, from perturbation theory. While it is computationally more expensive compared to the quasi-harmonic approximation its computational cost can be kept comparatively low for systems with higher symmetry. However it is limited to the order at which the series is truncated, most commonly the third [92]. Higher-order force constants can be calculated with rapidly increasing computational cost as the number of force evaluations increases with the order of the force constants.
- Self Consistent Phonon Theory: In Self Consistent Phonon Theory (SCPT) the phonon frequencies are corrected by self consistently solving the Dyson equation [60]. However, this requires computing the fourth-order force constants making it computationally expensive. Furthermore, higher-order anharmonicity is only implicitly accounted for. Accordingly, this approach does not include all accessible degrees of anharmonicity.
- Temperature-Dependent Effective Potentials: Temperature-Dependent Effective Potentials (TDEP) is mathematically equivalent to the SCPT. Here the force constants are fitted to anharmonic forces obtained from sampling the PES at a finite temperature. This can be either accomplished using harmonic sampling or other methods. It is applicable to *ab-initio* methods or semi-empirical FFs. Fitting only the hessian Φ_{IJ} leads to a renormalization of the force constants by implicitly including higher orders of anharmonicity. Higher-order Force Constants may also be obtained in this way. While this does formally not require knowledge about the fourth-order force constants it otherwise suffers from the same drawbacks as SCPT [40].
- Outlook: As we will discuss later molecular dynamics methods allow us to account for all orders of anharmonicity. However, this makes it highly computationally demanding. Accordingly performing molecular dynamics simulations using first principle methods is restricted to comparatively short time lengths and small supercells.

2.2.2 Anharmonic Effects

Anharmonic Effects: Lattice Expansion

In the static limit of immobile nuclei, the equilibrium volume V_0 and the respective lattice constants are defined via the minimum of the total energy of the system $V_0 = \min_V E_{tot}(V)$. At finite temperatures, however, the respective thermodynamic potential e.g., the Helmholtz free energy, has to be minimized:

$$dF = -SdT - PdV + \sum_I \mu_I N_I. \quad (2.66)$$

Here μ is the chemical potential, S the entropy, and P the pressure. Naturally, this introduces a temperature dependence in the equilibrium volume

$$V_0(T) = \min_V F(T, V). \quad (2.67)$$

By neglecting electronic contributions⁹, the Helmholtz free energy can be expressed in the harmonic approximation as $F(T, V) \approx E_{tot}(V) + F^{ha}(T)$ using the definition of $F^{ha}(T)$ given in Eq. (2.60). However, $F^{ha}(T)$ does not depend on the volume, so no lattice expansion (or contraction) occurs in this approximation. Accordingly, to assess and understand temperature-dependent volumes and lattice constants *anharmonic* effects have to be accounted for. In the most intuitive approach, anharmonic effects are *effectively* introduced by explicitly accounting for the volume dependence of the force constants $\Phi_{IJ}^{\alpha\beta} \rightarrow \Phi_{IJ}^{\alpha\beta}(V)$. In this so-called *quasi-harmonic* approximation [86], both the total energy $E_{tot}(V)$ and the phonon calculations $\Phi_{IJ}^{\alpha\beta}(V)$ are performed for a set of different volumes. The temperature-dependent volume $V_0(T)$ and/or lattice constants are then determined by minimizing the resulting Helmholtz free energy

$$F(T, V) \approx E_{tot}(V) + F^{qha}(T, V) \quad \text{with} \quad F^{qha}(T, V) = F^{ha}(T, \Phi_{IJ}^{\alpha\beta}(V)), \quad (2.68)$$

as shown in Fig. 2.7. The obtained equilibrium volumes $V_0(T)$ then allow to compute the volume expansion coefficient

$$\alpha(T) = \frac{1}{3V_0(T)} \left(\frac{\partial V_0(T)}{\partial T} \right)_V \quad (2.69)$$

Beside some notable exceptions (see Ref. [86]), $\alpha(T)$ is typically positive (lattice expansion): Larger volumes imply larger nearest neighbor distances and thus a smaller interaction (smaller force constants $\Phi_{IJ}^{\alpha\beta}$). In turn, this leads to lower eigenfrequencies $\omega_s(\mathbf{q})$ and thus to lower Helmholtz free energies due to entropic contributions. More insight can be gained by explicitly writing down the minimization problem in Eq. (2.67) as:

$$\frac{dF}{dV} = 0 \rightarrow -P = 0. \quad (2.70)$$

This demonstrates that minimizing the volume is equivalent to vanishing external pressure. As will be explained later, this can be used to calculate the fully anharmonic thermal expansion.

Anharmonic Effects: Lattice Thermal Transport

The thermal conductivity tensor $\kappa_{\alpha\beta}$, which describes the the capability of a material to conduct heat, is another prominent example of a physical quantity that can only be

⁹In solids with finite band gaps as the semiconductors of interest in this work, electronic contributions to the free energy are generally negligible [106].

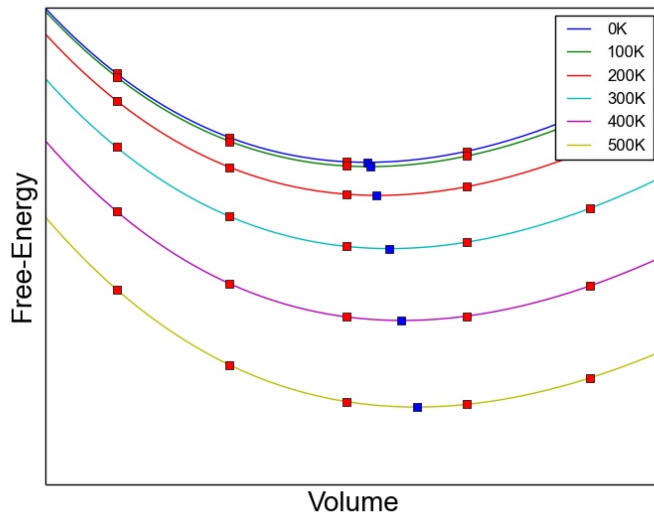


Figure 2.7: Birch-Murnaghan Equations in the quasi-harmonic approximation at different temperatures: The blue squares mark the volumes which minimize the free energy.

understood if anharmonic effects are taken into account. Formally, the thermal conductivity is defined through Fourier’s law [107]

$$J_\alpha = -\kappa_{\alpha\beta} \nabla_\beta T, \quad (2.71)$$

as the proportionality constant between the cartesian components of the applied temperature gradient ∇T and the heat flux \mathbf{J} , which naturally develops to act against the temperature gradient and to re-establish equilibrium. Generally, the thermal conductivity consists of three different contributions

$$\kappa = \kappa_{\text{phonon}} + \kappa_{\text{electron}} + \kappa_{\text{photon}}. \quad (2.72)$$

In this work, we limit ourselves to discuss the *lattice* or *phonon* thermal conductivity κ_{phonon} , since it is the dominant [106] contribution for semiconductors and insulators at non-incandescent temperatures.

The fact that heat transport phenomena cannot occur within a purely harmonic approximation becomes obvious one investigates the heat-flux in the phonon picture [107]

$$\mathbf{J} = (2\pi)^3 \sum_s \int \hbar\omega_s(\mathbf{q}) n_s(\mathbf{q}, t) \mathbf{v}_s(\mathbf{q}) d\mathbf{q} \approx \frac{1}{V_0} \sum_{\mathbf{q}, s} \hbar\omega_s(\mathbf{q}) n_s(\mathbf{q}, t) \mathbf{v}_s(\mathbf{q}). \quad (2.73)$$

Here V_0 denotes the volume of the unit cell. In this expression, each of the modes with occupation number $n_s(\mathbf{q})$ contribute to the heat flux, since they travel with the group velocity $\mathbf{v}_s(\mathbf{q})$ and carry the energy $\hbar\omega_s(\mathbf{q})$. In the harmonic approximation, however, all quantities that enter Eq. (2.73) stay constant over time: Even the occupa-

tion numbers $n_s(\mathbf{q}, t) = n_s^{eq}(\mathbf{q})$ are constant in time since all modes are decoupled (see Sec. 2.2.1). Accordingly, the heat flux \mathbf{J} in equilibrium vanishes in the harmonic approximation as the group velocity is the only antisymmetric quantity entering the heat-flux.

$$\omega_s(\mathbf{q}) = \omega_s(-\mathbf{q}) \quad \text{and} \quad n_s(\mathbf{q}, t) = n_s(-\mathbf{q}, t) \quad \text{but} \quad \mathbf{v}_s(\mathbf{q}) = -\mathbf{v}_s(-\mathbf{q}). \quad (2.74)$$

Hence, Eq. (2.71) cannot be fulfilled in a purely harmonic system.

Accordingly, it is necessary to include anharmonic effects explicitly to assess the thermal conductivity. This can be achieved by investigating the dynamics on the anharmonic potential energy surface using molecular dynamics approaches [95] or perturbatively [92].

Perturbative Thermal conductivity

This approach is often favored as it allows for relatively rapid calculations of the thermal conductivity. For simplicities sake, we restrict the derivation to the cubic isotropic case which allows us to write $\kappa = \kappa_{xx} = \kappa_{yy} = \kappa_{zz}$. A more general and detailed derivation can for instance be found in Ref. [107] and references therein.

To account for anharmonic effects, we first introduce the non-equilibrium occupation numbers $n_s(\mathbf{q})$ by introducing a mode specific deviation $\xi_s(\mathbf{q})$:

$$\begin{aligned} n_s(\mathbf{q}) &= \frac{1}{e^{\frac{\hbar\omega_s(\mathbf{q})}{k_B T} - \xi_s(\mathbf{q})} - 1} \\ &\approx n_s^{eq}(\mathbf{q}) + \frac{k_B T^2}{\hbar\omega_s(\mathbf{q})} \frac{\partial n_s^{eq}(\mathbf{q})}{\partial T} \xi_s(\mathbf{q}). \end{aligned} \quad (2.75)$$

When performing the Taylor expansion around equilibrium in the second step, we inherently assume that the deviations from equilibrium are small compared to the actual occupation numbers in equilibrium. Accordingly, the non-equilibrium occupation numbers $n_s(\mathbf{q})$ must fulfill the linearized Boltzmann equation

$$\mathbf{v}_s(\mathbf{q}) \cdot \nabla T \frac{\partial n_s^{eq}(\mathbf{q})}{\partial T} = \left(\frac{\partial n_s(\mathbf{q})}{\partial t} \right)_{scatt} \quad (2.76)$$

in the steady state. Here, the left hand side (drift term) describes the evolution of the non-equilibrium population due to a temperature gradient in the absence of phonon-phonon interaction. Conversely, the right hand side counterbalance this drift due to scattering processes. To describe them, the *single mode relaxation time approximation* is commonly employed: This implies that explicit correlations between the non-equilibrium occupation numbers of the different modes can be neglected, so that the scattering of one specific mode (s', \mathbf{q}') can be determined by assuming all other modes to follow the respective equilibrium distribution: $n_s(\mathbf{q}) = n_s^{eq}(\mathbf{q})$ for all $(s, \mathbf{q}) \neq (s', \mathbf{q}')$. In this approach, the right

2 Theory

hand side of Eq. (2.76) can be approximated as

$$\left(\frac{\partial n_s(\mathbf{q})}{\partial t}\right)_{scatt} \approx -\frac{\xi_s(\mathbf{q})}{\tau_s(\mathbf{q})} \frac{k_B T^2}{\hbar \omega_s(\mathbf{q})} \frac{\partial n_s^{eq}(\mathbf{q})}{\partial T} \quad (2.77)$$

whereby the mode specific relaxation times $\tau_s(\mathbf{q})$ have been introduced. Combining Eq. (2.76) and Eq. (2.77) yields an expression for $\xi_s(\mathbf{q})$ and thus for the $n_s(\mathbf{q})$ defined in Eq. (2.75) that can be inserted into Eq. (2.73):

$$\mathbf{J} = -\frac{1}{V_0 k_B T^2} \sum_{s\mathbf{q}} \hbar \omega_s(\mathbf{q}) \frac{\partial n_s^{eq}(\mathbf{q})}{\partial T} \tau_s(\mathbf{q}) \mathbf{v}_s(\mathbf{q}) (\mathbf{v}_s(\mathbf{q}) \cdot \nabla T). \quad (2.78)$$

For the isotropic case, a comparison with Fourier's law (2.73) yields:

$$\kappa = \frac{1}{3V_0} \sum_{q,s} \mathbf{v}_s(\mathbf{q})^2 c_s(\mathbf{q}) \tau_s(\mathbf{q}). \quad (2.79)$$

Most of the quantities ($\mathbf{v}_s(\mathbf{q}), c_s(\mathbf{q})$) entering κ as defined in Eq. (2.79) can be readily computed in the harmonic approximation. The lifetime $\tau_s(\mathbf{q})$, however, is infinite in this approximation, due the absence of scattering $n_s(\mathbf{q}) = n_s^{eq}(\mathbf{q})$ discussed before. Formally, the thermal conductivity is thus also infinite in this approximation.

If anharmonic effects are taken into account, the lifetimes can be determined via [109]

$$\tau_s(\mathbf{q}) = \frac{1}{2\Gamma_s(\mathbf{q})}, \quad (2.80)$$

from the imaginary part of the self energy $\Gamma_s(\mathbf{q})$. If only the third order force-constants $\Psi_{IJK}^{\alpha\beta\gamma}$ are taken into account, this self-energy is given by [109]:

$$\Gamma_s(\mathbf{q}) = \frac{18\pi}{\hbar^2} \sum_{\mathbf{q}'s', \mathbf{q}''s''} |\Psi_{s,s',s''}(\mathbf{q}, \mathbf{q}', \mathbf{q}'')|^2 [(n_{s'}^{eq}(\mathbf{q}') + n_{s''}^{eq}(\mathbf{q}'') + 1) \delta(\omega - \omega_{s'}(\mathbf{q}') - \omega_{s''}(\mathbf{q}'')) + (n_{s'}^{eq}(\mathbf{q}') - n_{s''}^{eq}(\mathbf{q}'')) (\delta(\omega + \omega_{s'}(\mathbf{q}') - \omega_{s''}(\mathbf{q}'')) - \delta(\omega - \omega_{s''}(\mathbf{q}') + \omega_{s''}(\mathbf{q}'')))] \quad (2.81)$$

The $\Psi(\mathbf{q}s, \mathbf{q}'s', \mathbf{q}''s'')$ are the Fourier transformed third order force constants $\Psi_{IJK}^{\alpha\beta\gamma}$:

$$\begin{aligned} \Psi_{s,s',s''}(\mathbf{q}, \mathbf{q}', \mathbf{q}'') &= \frac{1}{3! \sqrt{N_0}} \sum_{IJK, \alpha\beta\gamma} \epsilon_{I,s}^{\alpha}(\mathbf{q}) \epsilon_{J,s'}^{\beta}(\mathbf{q}') \epsilon_{K,s''}^{\gamma}(\mathbf{q}'') \\ &\times \sqrt{\frac{\hbar}{2M_I \omega_s(\mathbf{q})}} \sqrt{\frac{\hbar}{2M_J \omega_{s'}(\mathbf{q}')}} \sqrt{\frac{\hbar}{2M_K \omega_{s''}(\mathbf{q}'', s'')}} \\ &\times \Psi_{IJK}^{\alpha\beta\gamma} e^{i\mathbf{q}\cdot\mathbf{R}_I} e^{i\mathbf{q}'\cdot\mathbf{R}_J} e^{i\mathbf{q}''\cdot\mathbf{R}_K} \Delta(\mathbf{q} + \mathbf{q}' + \mathbf{q}'') \end{aligned} \quad (2.82)$$

Here, the factor $\Delta(\mathbf{q} + \mathbf{q}' + \mathbf{q}'')$ ensures momentum conservation and is thus 1 if $\mathbf{q} + \mathbf{q}' + \mathbf{q}''$ corresponds to a reciprocal lattice vector and 0 otherwise. Please note that the expressions (2.80)-(2.82) can be derived directly in a quite lengthy process from the third-order Hamiltonian, as detailed in Ref. [109].

The described approach has so far been used successfully in a series of studies [93, 92], but fails for moderately anharmonic materials as only the leading anharmonic order is included. As explained in Sec. 2.2.1, this can be mitigated to a certain extent, by renormalizing the force constants at finite temperatures, effectively accounting for higher orders of anharmonicity, or by truncating the Taylor series at higher orders.

Outlook: Fully Anharmonic Thermal Conductivity

However, no approach introduced until this point captures all accessible degrees of anharmonicity. Using molecular dynamics methods in conjunction with the Green-Kubo relations [72] one can account for all accessible orders of anharmonicity in the thermal conductivity. This however requires a suitable representation of the heat flux:

$$\begin{aligned} \mathbf{J} &= \frac{d}{dt} \sum_I \mathbf{R}_I E_I \\ &= \underbrace{\sum_I \mathbf{v}_I E_I}_{\text{Convective Heat Flux}} + \underbrace{\sum_I \mathbf{R}_I \dot{E}_I}_{\text{Conductive Heat Flux}} \end{aligned} \quad (2.83)$$

The convective heat flux arises due to mass transport while the conductive heat flux is due to energy transport. In solids the conductive heat flux is the major contribution and the convective heat flux is negligible [73].

Furthermore the given conductive heat flux is well defined since it depends on energy derivatives. After some algebra the expression for the conductive heat flux can be rewritten in terms of forces instead of per atom energies (see Sec. ?? for the derivation).

$$\mathbf{J} = \sum_{IJ} (\mathbf{R}_J - \mathbf{R}_I) \left(\frac{\partial V_J}{\partial \mathbf{R}_I} \cdot \frac{\mathbf{p}_I}{m_I} \right) \quad (2.84)$$

Using the virial stress

$$\sigma_I = \sum_{I < J} (\mathbf{R}_J - \mathbf{R}_I) \left(\frac{\partial V_J}{\partial \mathbf{R}_I} \right), \quad (2.85)$$

the conductive heat flux can thus be rewritten as:

$$\mathbf{J} = \sum_I \sigma_I \mathbf{v}_I \quad (2.86)$$

\mathbf{J} is now uniquely determined. Finally the thermal conductivity is related to the autocorrelation function of the heat flux via the Green-Kubo relations [96] and can be calculated by evaluating the integral:

$$\kappa = \lim_{t_0, \Lambda \rightarrow \infty} \frac{V}{k_B T^2 t_0} \int_0^\Lambda \int_0^{t_0 - \Lambda} J(t) J(t_0 + t) dt. \quad (2.87)$$

Furthermore the average vibrational lifetime can be calculated from the autocorrelation function too:

$$\tau = \lim_{t_0, \Lambda \rightarrow \infty} \frac{\int_0^\Lambda \int_0^{t_0 - \Lambda} J(t) J(t_0 + t) dt}{\text{var}(J)} \quad (2.88)$$

2.2.3 Equilibrium Molecular Dynamics: The Nuclei as a Classical Particle

The most straightforward way to access the anharmonic parts of the PES is by sampling it directly using Molecular Dynamics (MD). Here the propagation of the nuclei is directly simulated by Newton's equations of motion:

$$\mathbf{F}_I(t) = M_I \ddot{\mathbf{R}}_I(t). \quad (2.89)$$

which are stepwise integrated $t \rightarrow t + \Delta t$ for a finite timestep Δt starting from a chosen initial condition for the positions $\mathbf{R}_I(t_0)$ and the velocities $\dot{\mathbf{R}}_I(t_0)$. A prominent example for an algorithm to perform this numerical integration is the *Velocity Verlet* algorithm [49]:

$$\mathbf{R}_I(t + \Delta t) = \mathbf{R}_I(t) + \dot{\mathbf{R}}_I(t) \Delta t + \frac{\mathbf{F}_I(t)}{2M_I} \Delta t^2 \quad (2.90)$$

$$\dot{\mathbf{R}}_I(t + \Delta t) = \dot{\mathbf{R}}_I(t) + \frac{\mathbf{F}_I(t) + \mathbf{F}_I(t + \Delta t)}{2M_I} \Delta t. \quad (2.91)$$

It is in use up to this day due to its high numerical accuracy up to an order of $\mathcal{O}(t^4)$ and an only minimal increase in computational cost compared to earlier examples (e.g. the Verlet algorithm which only has an accuracy of $\mathcal{O}(t^2)$ [49]). Additionally, the velocity Verlet algorithm is also symmetric under time reversal. Directly evaluating the dynamics of the nuclei has the added benefit that phase space integrals do not have to be evaluated directly since the ergodic hypothesis postulates that ensemble averages equal time averages. Phase space is defined as a smooth manifold that is equipped with the canonical symplectic form, i.e., the Poisson brackets that define the time evolution of an observable as:

$$\begin{aligned} \frac{dA(\mathbf{R}, \dot{\mathbf{R}})}{dt} &= \{H, A\} \\ &= \frac{\partial H}{\partial \mathbf{R}} \frac{\partial A}{\partial \dot{\mathbf{R}}} - \frac{\partial A}{\partial \mathbf{R}} \frac{\partial H}{\partial \dot{\mathbf{R}}}. \end{aligned} \quad (2.92)$$

Here H is the Hamilton function. Importantly, the Verlet algorithm is symplectic, i.e., it preserves the symplectic form. To sample different thermodynamic ensembles, the algorithm can be augmented by attaching so-called *thermostats* [48, 49]. Thermostats emulate the behavior of a given thermodynamic ensemble at a constant temperature (more detailed explanations can be found in the appendix) For this work the micro- (NVE) and canonical-ensembles (NVT/NPT) are relevant. Their statistics (and generally the

statics of any equilibrium ensemble) are defined by the partition function Z defined by:

$$Z = \int \rho(H(\mathbf{R}), \mathbf{p}) d\mathbf{R} d\mathbf{p}. \quad (2.93)$$

It defines the probability distribution $\rho = \frac{H(\mathbf{R}, \mathbf{p})}{Z}$, from which the equilibrium expectation value of a thermodynamical observable $A(\mathbf{R}, \mathbf{p})$ can be calculated:

$$\langle A \rangle = \int \rho(\mathbf{R}, \mathbf{p}) A(\mathbf{R}, \mathbf{p}) d\mathbf{R} d\mathbf{p}. \quad (2.94)$$

The meaning of "Classical" in Molecular Dynamics

At this point an important distinction between classical MD and classical nuclei must be made as this can lead to confusion. Classical MD usually (and also in this work) refers to MD simulations where the forces to propagate the nuclei are generated from semi-empirical potentials, MD simulations based on DFT (or other *ab initio* methods) is referred to *ab-initio* MD. However, in both cases the nuclei are treated as classical particles, obeying the Newtonian equations of motion. Accordingly, the degrees of anharmonicity accessible by classical and *ab initio* MD are referred to as "classical accessible degrees of anharmonicity".

The Micro-Canonical Ensemble

The microcanonical ensemble is characterized by the conservation of the number of particles (N), volume (V), and energy (E). Accordingly, its dynamics are fully described by the Newtonian equations of motions and their initial conditions (\mathbf{R}, \mathbf{p}). Usually, these are obtained from snapshots of the system, which is thermalized in the canonical ensemble. The partition function of the micro-canonical ensemble is given by:

$$Z_{NVE} = \mathcal{N} \int \delta(H(\mathbf{R}), \mathbf{p}) - E) d\mathbf{R} d\mathbf{p}. \quad (2.95)$$

Here \mathcal{N} is a normalization constant. While the partition function includes all information about the system solving the integral directly is not practicable. Accordingly, the PES is explored using for example the velocity Verlet algorithm.

The Canonical-Ensemble

In the canonical ensemble the conserved quantities (N) (number of particles), (V/P) (volume or pressure), and (T) (Temperature). Focusing on preserving the volume the partition function of the canonical ensemble can be written as

$$Z = \int e^{-\beta H(\mathbf{R}, \mathbf{p})} d\mathbf{R} d\mathbf{p}. \quad (2.96)$$

2 Theory

Here $\beta = \frac{1}{k_{\text{B}}T}$ is the inverse temperature. The exponential form of the distribution function can be derived in different ways. Most straightforward if one embeds a micro-canonical ensemble within a second micro-canonical ensemble and only allows for energy transfer between them, hereby the second ensemble acts as a heat bath keeping the first one at a constant temperature. An exact derivation is shown for example in Ref [49]. Again solving the integral in Eq. 2.96 directly is only possible for a small number of systems e.g. for a harmonic potential however for general systems it remains not feasible. To sample the canonical ensemble regardless, the equations of motion can be coupled to a thermostat. A selection of which is presented in the appendix of this work.

Why are we not always using MD ?

(*Ab-initio*) Molecular Dynamics enables us to sample all classical accessible degrees of anharmonicity from which theoretically all anharmonic effects can be calculated with much higher qualitative accuracy compared to the previously introduced methods. However at least in *ab-initio* MD we are still limited to comparatively small supercells and short time scales, accordingly, long-wavelength phonons are often not accounted for. Furthermore, to obtain statistically reliable results, multiple trajectories are required, making *ab-initio* MD computationally expensive. A more severe drawback of classical and *ab-initio* MD is that the nuclei are treated as classical particles which is a good approximation for many materials, but not for all. Especially describing organic crystals and molecules requires the inclusion of quantum nuclear fluctuations to access all degrees of anharmonicity¹⁰ [123].

2.2.4 The Quantum Canonical-Ensemble

Similar to the classical canonical ensemble we can define a partition function to calculate the expectation value of observables. For this purpose the operator trace and the density matrix $\rho = \sum_I p_I |\Psi_I\rangle \langle\Psi_I|$ need to be introduced:

$$\langle\hat{A}\rangle = \text{Tr}(\hat{A}\hat{\rho}) = \text{Tr}\left(\sum_I p_I |\Psi_I\rangle \langle\Psi_I| \hat{A}\right). \quad (2.97)$$

Here p_I is the probability associated with the state $|\Psi_I\rangle$. In the quantum canonical ensemble the partition function is replaced by the trace of the canonical density matrix

$$\hat{\rho} = e^{-\beta\hat{H}} \quad (2.98)$$

¹⁰This is not limited to organic compounds a prominent example is "classical" water which would be poisonous [124]

and thus defined as:

$$Z = \text{Tr}(\rho). \quad (2.99)$$

This makes the expectation value of an operator in the canonical ensemble

$$\langle A \rangle = \frac{\text{Tr}(Ae^{-\beta H})}{\text{Tr}(\rho)} \quad (2.100)$$

Evaluating this expression however requires solving the Hamiltonian from Eq. 2.8 which is prohibitively expensive. However, it is possible to reformulate the quantum canonical partition function in terms of an imaginary time path integral [63, 67]

2.2.5 The Path Integral Formalism

The original motivation behind the path integral formalism was to find the quantum mechanical correspondence to the principle of least action in classical mechanics [62]. Accordingly, the roots of the path integral formalism are found in classical physics. The principle of least action requires that any particle takes the path, which requires the least amount of energy. Mathematically this means that the action functional must be stationary. Formally the action functional is defined as:

$$S = \int_{t_0}^{t_1} L(\mathbf{R}(t), \dot{\mathbf{R}}(t), t) dt \quad (2.101)$$

$$(2.102)$$

Here $\mathbf{R}(t)$ are the positions, $\dot{\mathbf{R}}$ the velocities, and the Lagrange function. The Lagrange function is determined by the kinetic energy T and potential energy V and is typically given by:

$$L(\mathbf{R}(t), \dot{\mathbf{R}}(t), t) = T(\dot{\mathbf{R}}) - V(\mathbf{R}). \quad (2.103)$$

Mathematically it describes a surface, determining all possible configurations of the system¹¹. In classical mechanics the only relevant path is the one for which the action S is stationary:

$$\delta S = 0. \quad (2.104)$$

In 1933 Paul Dirac attempted to generalize this principle to the then-new field of quantum mechanics [62] by extending Norbert Wiener's description of Brownian motion. He found that a quantum state q at different times t and T can be written as:

$$\langle q_t | q_T \rangle = \int e^{\frac{i}{\hbar} F}. \quad (2.105)$$

¹¹Please note that the Lagrange function can also depend on higher-order derivatives, the most prominent example is the Einstein-Hilbert action.

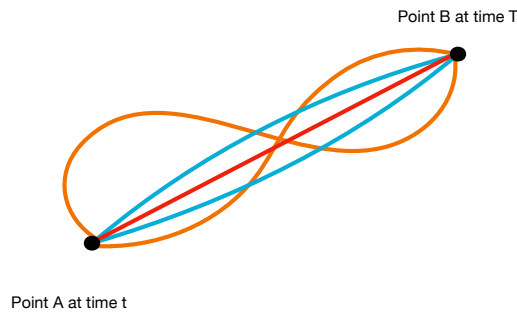


Figure 2.8: This figure illustrates the paths a particle traveling from point A to B can take. The red line is the most likely path at which the action is stationary, blue lines are the probable paths that contribute to the probability amplitude, and orange lines are paths that generally cancel each other out.

Here F is a function depending on q_t, q_1, \dots, q_T and h the Planck constant. In the $h \rightarrow 0$ limit, the classical principle of least action (Eq. 2.104) is recovered. The implications might not be obvious at first glance but Eq. (2.105) demonstrates that the principle of least action in classical mechanics is deeply connected to quantum mechanics. However, Dirac did not show how to recover the Schrödinger equation nor did he provide a way to sum over all possible paths. Richard Feynman addressed these open questions in his Ph.D. thesis. Mathematically he derived the path integral from the time evolution operator, as described in the next section. He came to the conclusion that the probability amplitude of a particle traveling from point A to B is given by the sum of all possible amplitudes. [63] Theoretically, this also includes paths that go to the end of the universe but by summing over all paths they cancel each other out, and only the most probable paths contribute to the result. This is illustrated in Fig.2.8.

Imaginary Time: Wick Rotation

As mentioned above Feynman derived the path integral from the time evolution operator:

$$\hat{U}(t) = e^{-\frac{it\hat{H}}{h}}. \quad (2.106)$$

Here \hat{H} is the Hamilton operator. The time evolution operator is linked to the canonical density matrix Eq. (2.98) via the Wick rotation [64]. Originally developed as a tool in relativistic quantum field theory to map problems that are difficult to solve in Minkowski to Euclidian space¹², the Wick rotation is also widely used in statistical physics where it is

¹²A Minkowski space is characterized by the signature of its (pseudo)metric $(-1,1,1,1)$, conversely, the metric of a Euclidian space has the signature $(1,1,1,1)$.

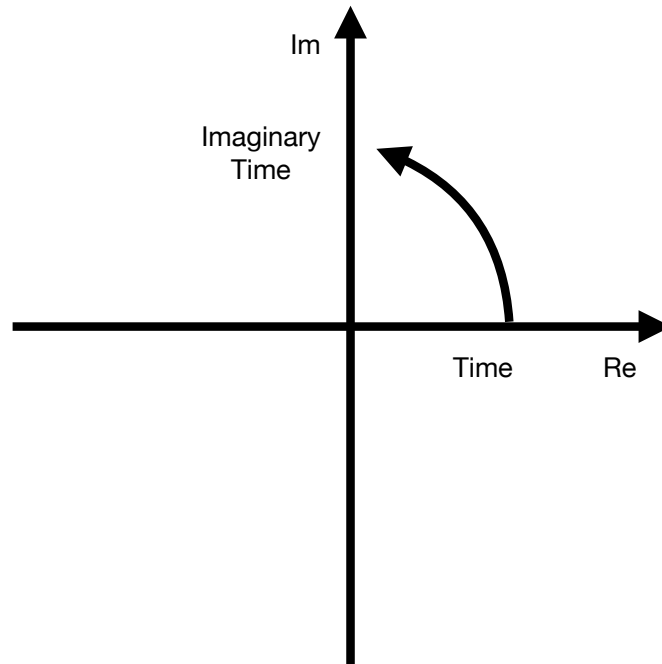


Figure 2.9: The Wick rotation maps time from the real to the imaginary axis

defined as:

$$\frac{it}{\hbar} = \beta \quad (2.107)$$

This transforms time by a $\pi/2$ rotation from the real axis to the imaginary axis, as illustrated in Fig. 2.9. Applied to the time evolution operator we find that

$$e^{-\frac{it\hat{H}}{\hbar}} \xrightarrow{\text{Wick rotation}} e^{-\beta\hat{H}}, \quad (2.108)$$

the canonical density matrix, as defined in Eq. 2.98, is exactly the Wick rotated time evolution operator, in which the imaginary unit in the exponent is replaced by a real number. Deriving the path integral from the canonical density matrix instead of the time evolution operator has many advantages for statistical physics, both mathematically and computationally, as shown at the end of the section.

Derivation of the Imaginary Time Path Integral

To derive the path integral formulation of the quantum canonical partition function, from Eq. 2.99, one starts by writing the corresponding density matrix in position space:

$$\hat{\rho}(R) = \langle R | e^{-\beta\hat{H}} | R \rangle. \quad (2.109)$$

2 Theory

Since the kinetic and potential energy operators do not commute, the density operator cannot be factorized in the potential and kinetic energy part. However, since the Hamilton operator is (essentially) self-adjointed [66] the canonical density matrix can be written as:

$$e^{-\beta(T+V)} = \lim_{P \rightarrow \infty} \left(e^{\frac{-\beta V}{2P}} e^{\frac{-\beta T}{P}} e^{\frac{-\beta V}{2P}} \right)^P \quad (2.110)$$

Here we used the Trotter product formula [65], importantly the error introduced by this factorization decreases quadratically with P . Using this result we can reformulate Eq. 2.109 as a product of exponential operators, which only depend on the kinetic and potential energy operators, respectively:

$$\rho(R) = \lim_{P \rightarrow \infty} \langle R | \left(e^{\frac{-\beta V}{2P}} e^{\frac{-\beta T}{P}} e^{\frac{-\beta V}{2P}} \right)^P | R \rangle \quad (2.111)$$

To evaluate the resulting expression we introduce the resolution of identity:

$$\mathbf{1} = \int |R_\alpha\rangle \langle R_\alpha| dR_\alpha. \quad (2.112)$$

Inserting the resolution of identity into Eq. 2.111, one obtains:

$$\begin{aligned} \rho(R = R_1) &= \lim_{P \rightarrow \infty} \int \langle R_1 | e^{\frac{-\beta V}{2P}} e^{\frac{-\beta T}{P}} e^{\frac{-\beta V}{2P}} | R_P \rangle \langle R_P | e^{\frac{-\beta V}{2P}} e^{\frac{-\beta T}{P}} e^{\frac{-\beta V}{2P}} | R_{P-1} \rangle \\ &\dots \langle R_2 | e^{\frac{-\beta V}{2P}} e^{\frac{-\beta T}{P}} e^{\frac{-\beta V}{2P}} | R_1 \rangle \prod_{\alpha=2}^P dR_\alpha. \end{aligned} \quad (2.113)$$

Given that we expanded the identity operator in eigenfunctions of the position operator, we can evaluate the exponential operator of the potential energy:

$$\langle R_{\alpha+1} | \left(e^{\frac{-\beta V}{2P}} e^{\frac{-\beta T}{P}} e^{\frac{-\beta V}{2P}} \right) | R_\alpha \rangle = e^{\frac{-\beta V(R_{\alpha+1})}{2P}} \langle R_{\alpha+1} | e^{\frac{-\beta T}{P}} | R_\alpha \rangle e^{\frac{-\beta V(R_\alpha)}{2P}}. \quad (2.114)$$

This only leaves the kinetic energy part to be evaluated. To this end, the unity operator is again inserted, but since the kinetic energy operator depends on the momentum operator the unity operator, has to be written in terms of eigenstates of the momentum operator:

$$\mathbf{1} = \int |p_\alpha\rangle \langle p_\alpha| dp_\alpha. \quad (2.115)$$

Using this representation the kinetic term of Eq. (2.114) can be evaluated:

$$\begin{aligned} \langle R_{\alpha+1} | e^{-\beta_P T} | R_\alpha \rangle &= \int \langle R_{\alpha+1} | p_{\alpha+1} \rangle \langle p_{\alpha+1} | e^{-\beta_P T} | R_\alpha \rangle dp_{\alpha+1} \\ &= \int e^{-\beta_P T(p_{\alpha+1})} \langle R_{\alpha+1} | p_{\alpha+1} \rangle \langle p_{\alpha+1} | R_\alpha \rangle dp_{\alpha+1}. \end{aligned} \quad (2.116)$$

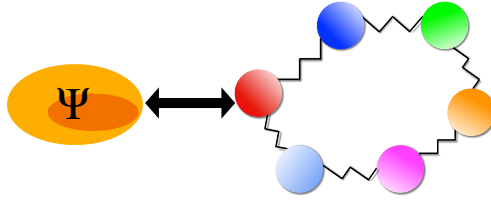


Figure 2.10: The imaginary time path integral relates the statistical properties of a quantum mechanical system to that of classical ring polymer.

For the sake of readability, we defined $\beta_P = \frac{\beta}{P}$. All terms in this equation are known:

$$\langle R_{\alpha+1} | p_{\alpha+1} \rangle = \frac{1}{\sqrt{2\pi\hbar}} e^{ip_{\alpha+1}R_{\alpha+1}/\hbar} \quad (2.117)$$

$$\langle p_{\alpha+1} | R_{\alpha} \rangle = \frac{1}{\sqrt{2\pi\hbar}} e^{-ip_{\alpha+1}R_{\alpha}/\hbar}. \quad (2.118)$$

Inserting these results into Eq. 2.116 we find

$$\begin{aligned} \langle R_{\alpha+1} | e^{-\beta_P T} | R_{\alpha} \rangle &= \frac{1}{2\pi\hbar} \int e^{-\beta_P T(p_{\alpha+1})} e^{i\frac{p_{\alpha+1}(R_{\alpha+1}-R_{\alpha})}{\hbar}} dp_{\alpha+1} \\ &= \sqrt{\frac{m}{2\pi\beta_P\hbar^2}} e^{-\frac{\beta_P M\omega_P^2}{2}(R_{\alpha+1}-R_{\alpha})^2} \end{aligned} \quad (2.119)$$

Here we have defined $\omega_P = \frac{1}{\beta_P\hbar}$.

Combining Eq. 2.114 with Eq. 2.119 one can hence write the exact partition function, by evaluating the trace of Eq. 2.113, as:

$$Z = \lim_{P \rightarrow \infty} \left(\frac{M}{2\pi\beta_P\hbar^2} \right)^{P/2} \int e^{-\beta_P \sum_{\alpha} \left(-\frac{M\omega_P^2}{2}(R_{\alpha+1}-R_{\alpha})^2 + V(R_{\alpha}) \right)} \prod_{\alpha=1}^P dR_{\alpha}. \quad (2.120)$$

This is the main result of the (imaginary time) path integral formalism, it defines an isomorphism between the (discrete) quantum canonical partition function and the partition function of a ring polymer coupled by harmonic springs vibrating with the frequency ω_P [67]. This relationship is shown schematically in Fig 2.10. The index α represents the *alpha*'th replica. Different from Feynmans' formulation, the path integral in Eq. 2.120 sums over all possible closed paths in configuration space instead of real space. The generalization to three dimensions simply requires adding the corresponding Cartesian indices and is straightforward. In theory, the limit $P \rightarrow \infty$ has to be evaluated to obtain the exact result. However, the error in the factorization of Eq. 2.110 decreases as $\mathcal{O}(1/P^2)$, so in practice, finite, sufficiently high, values of P are chosen. However, what "sufficiently high" means is highly problematic, i.e. temperature and material, dependent in our case. Light elements, for instance, often exhibit strong quantum nuclear fluctuations even at elevated temperatures, which become more pronounced at lower temperatures.

Why not use Real-Time Path Integrals ?

Feynmans' original real-time path integral uses a slightly different form compared to the imaginary time path integral:

$$U = \lim_{P \rightarrow \infty} \left(\frac{MP}{2\pi i t \hbar^2} \right)^{P/2} \int e^{\frac{i}{\hbar P} \sum_{\alpha} \left(-\frac{M^2 P^2}{2t} (R_{\alpha+1} - R_{\alpha})^2 - tV(R_{\alpha}) \right)} \prod_{\alpha=1}^P dR_{\alpha}. \quad (2.121)$$

The differences to the imaginary time path integral in Eq. (2.120) are that the prefactor in the exponent is imaginary and that the exponent is a Lagrangian type function ($T - V$) instead of a Hamiltonian one ($T+V$). Therefore the real-time path integral is not positive definite and thus does not define a probability measure. Accordingly, all paths apriori have to be taken as equally possible, requiring the evaluation of all possible paths (as sketched in Fig. 2.8). In practical calculations and simulations this leads to what is called the "sign problem" [69] causing, amongst others, uncontrollable noise. Conversely, the imaginary time path integral meets the criteria of a probability measure and naturally assigns a probability weight to all paths allowing for numerically efficient implementations. Furthermore, for many potentials, the real-time path integral (in the limit $P \rightarrow \infty$) does not even exist and requires the introduction of a "pseudo time" [70].

Observables in the Path Integral Formalism

Using the density matrix the expectation value of an operator is given by Eq. 2.100. A path integral formulation of the same operator A is called an estimator. If the operator \hat{A} only depends on the position its estimator can be derived easily by keeping it on the left side during the path integral derivation. This yields a function $A(R_1)$ and since all replicas are equivalent the estimator can be written as the average over all replicas:

$$\langle A \rangle_P = \frac{\int e^{-\beta_P \sum_{\alpha} \left(-\frac{\beta_P M \omega_P^2}{2} (R_{\alpha+1} - R_{\alpha})^2 + V(R_{\alpha}) \right)} \frac{\sum_{\alpha} A(R_{\alpha})}{P} \prod_{\alpha=1}^P dR_{\alpha}}{\int e^{-\beta_P \sum_{\alpha} \left(-\frac{\beta_P M \omega_P^2}{2} (R_{\alpha+1} - R_{\alpha})^2 + V(R_{\alpha}) \right)} \prod_{\alpha=1}^P dR_{\alpha}}. \quad (2.122)$$

Probably the most obvious examples are the position and potential energy estimators:

$$\mathbf{R}_C = \frac{1}{P} \sum_{\alpha}^P \mathbf{R}_{\alpha} \quad (2.123)$$

$$V(\mathbf{R}) = \frac{1}{P} \sum_{\alpha}^P V(\mathbf{R}_{\alpha}) \quad (2.124)$$

An important side note is that the variable \mathbf{R}_C corresponds to the center of mass of the replica chain and is called the path centroid. Estimators, which depend only on individual replicas, as the position and potential energy, are called local. This is however

not the case if the operator depends also on the momentum. A simple example is the energy, in its most bare bone form the energy estimator can be directly derived from the partition function in Eq. 2.120 via $E = \frac{\partial \ln(Z)}{\partial \beta}$. This yields the thermodynamic energy estimator:

$$E^{\text{TD}} = \frac{P}{2\beta} - \frac{1}{P} \sum_{\alpha}^P \frac{M}{2\omega_P^2} (R_{\alpha} - R_{\alpha+1}) + \frac{1}{P} \sum_{\alpha}^P V(R_{\alpha}) \quad (2.125)$$

It is easy to distinguish between the potential energy estimator

$$V = \frac{1}{P} \sum_{\alpha}^P V(R_{\alpha}) \quad (2.126)$$

and the kinetic energy estimator:

$$T^{\text{TD}} = \frac{P}{2\beta} - \frac{1}{P} \sum_{\alpha}^P \frac{M}{2\omega_P^2} (R_{\alpha} - R_{\alpha+1})^2 \quad (2.127)$$

It is immediately evident that the kinetic energy does not only depend on individual replicas but also on cross-correlations between them. Thus this is called a non-local estimator.

Sampling the Phase Space using Path Integral Molecular Dynamics

There are two established methods to evaluate the integral in Eq. 2.120. One is Path Integral Monte Carlo (PIMC), where the PES is explored by generating random samples, distributed according to the probability distribution:

$$e^{-\beta_P \sum_{\alpha}^P \left(-\frac{M\omega_P^2}{2} (R_{\alpha+1} - R_{\alpha})^2 + V(R_{\alpha}) \right)}. \quad (2.128)$$

The other method is Path Integral Molecular Dynamics (PIMD) [68]. PIMD uses the prefactor of Eq. 2.120 to reintroduce momenta:

$$\sqrt{\frac{2\pi M}{\beta}} = \int_{\mathcal{R}} e^{-\beta \frac{p^2}{2M}}. \quad (2.129)$$

Accordingly Eq. (2.120) can be rewritten as:

$$Z = \lim_{P \rightarrow \infty} \left(\frac{1}{2\pi\hbar^2} \right)^P \int e^{-\beta_P \sum_{\alpha}^P \left(\frac{p_{\alpha}^2}{2M} - \frac{\beta_P M \omega_P^2}{2} (R_{\alpha+1} - R_{\alpha})^2 + V(R_{\alpha}) \right)} \prod_{\alpha=1}^P dR_{\alpha} \prod_{\alpha=1}^P dp_{\alpha}. \quad (2.130)$$

This yields an effective Hamiltonian

$$H_P = \sum_{\alpha} \left(\frac{p_{\alpha}^2}{2M} - \frac{\beta_P M \omega_P^2}{2} (R_{\alpha+1} - R_{\alpha})^2 + V(R_{\alpha}) \right), \quad (2.131)$$

2 Theory

that effectively describes a ring-polymer of P classical systems coupled by harmonic springs. Accordingly, the system can be evolved using the Hamiltons' equation of motion:

$$\dot{p}_\alpha = \frac{M}{\beta_P^2 \hbar^2} (2R_\alpha - R_{\alpha-1} - R_{\alpha+1}) - \frac{\partial V(R_\alpha)}{\partial R_\alpha} \quad (2.132)$$

$$\dot{R}_\alpha = \frac{p_\alpha}{M} \quad (2.133)$$

The dynamics generated by these equations of motion provide an ingenious way to evaluate the integral from Eq. 2.120. However one needs to keep in mind that the introduced momenta are purely fictitious and were only introduced as sampling devices. Accordingly, they do not have a strict physical meaning and the trajectories produced are purely statistical. One might say that PIMD is only a clever Monte Carlo scheme.

The Normal Mode Representation

An important technical concept in obtaining an efficient implementation of PIMD is the normal mode representation of Eq. (2.131). For that purpose the ring polymer Hamiltonian is rewritten in matrix form:

$$H_P = \sum_{\alpha I} \left(\frac{\mathbf{p}_I^\alpha \cdot \mathbf{p}_I^\alpha}{2M_I} + \frac{1}{2} \mathbf{R}_I^{T\alpha} S_I^\alpha \mathbf{R}_I^\alpha + V(\{\mathbf{R}^\alpha\}) \right). \quad (2.134)$$

Here S denotes the matrix that couples the different replicas to each other. Using periodic boundary conditions in the ring polymer (e.g. if the ring polymer has P replicas the replica number $P+1$ is identical to the first replica), the components of the matrix S can be written as

$$S_I^\alpha := \frac{\omega_P^2}{2M_I} (2\delta_{\alpha\alpha} - \delta_{\alpha\alpha-1} - \delta_{\alpha\alpha+1}) \quad (2.135)$$

This is a tri-diagonal matrix with additional elements on the corners which account for the periodic boundary conditions. It takes the form:

$$S = \frac{\omega_P^2}{M_I} \begin{pmatrix} 2 & -1 & 0 & \cdots & -1 \\ -1 & 2 & -1 & 0 & \cdots \\ 0 & \ddots & \ddots & \ddots & \ddots \\ \vdots & \cdots & -1 & 2 & -1 \\ -1 & 0 & \cdots & -1 & 2 \end{pmatrix}$$

Mathematically S describes a closed chain of P harmonic oscillator with nearest-neighbor coupling. The transformed momenta and position can be written as:

$$\tilde{\mathbf{p}}^\nu = \sum_{\alpha} \mathbf{p}^{\alpha} C_{\alpha\nu} \quad (2.136)$$

$$\mathbf{q}_\nu = \sum_{\alpha} \mathbf{R}^{\alpha} C_{\alpha\nu}. \quad (2.137)$$

The exact form of the transformation matrix C can be found in Ref. [49] Note that the index ν indicates a vibrational mode and not a specific replica index. Finally, we find the diagonalised matrix elements for the coupling matrix S :

$$\omega_\nu = 2\omega_P \sin(\nu\pi/P). \quad (2.138)$$

Inserting the results into Eq. (2.134) yields the ring polymer Hamiltonian in normal mode coordinates:

$$H_P = \sum_{\nu I} \left(\frac{\tilde{\mathbf{p}}_I^\nu \cdot \tilde{\mathbf{p}}_I^\nu}{2M_I} + \frac{M\omega_\nu^2}{2} \mathbf{q}_{\nu I}^2 + V(\{\mathbf{R}^\nu(\mathbf{q})\}) \right). \quad (2.139)$$

This representation of H_P offers insight into the centroid which corresponds to the mode $\nu = 0$ where the ring polymer contribution $\frac{M\omega_\nu^2}{2} \mathbf{q}_{\nu I}^2$ vanishes since $\omega_0 = 0$. Accordingly, the centroid can be regarded as more ‘‘classical’’ compared to the ring polymer mode $\nu > 0$

Alternatives to PIMD

While PIMD and PIMC are the most commonly used (and fastest) methods to sample the PES including quantum nuclear fluctuations they are not the only ones. Finding (approximate) solutions of Eq. 2.8 is an active field of research. Two prominent examples are the Vibrational Configuration Interaction [43, 44, 45] (VCI) and Vibrational Coupled Cluster [41] (VCC) methods which are inspired by their electronic structure counterparts. Accordingly, both approximate the exact wave function of the nuclear Hamiltonian in Eq. 2.8 to include correlation effects. Besides scaling to the order of $(O)(N^D)$ where N is the number of basis functions per mode and D the tensor dimensionality, VCI and VCC require a dense representation of the PES increasing the computational cost significantly. This makes VCI and VCC only suitable for molecules but not solids which is the focus of this work.

2.2.6 Sampling the Potential Energy Surface by Chance: Harmonic Sampling

The MD/PIMD methods for sampling the PES introduced until this point are highly accurate, but also computational demanding. Since Molecular Dynamics (ab initio and classical) samples the PES by propagating the nuclei in time which requires momenta. Conveniently the cost can be alleviated by using Monte Carlo sampling generating displacements based

on the harmonic approximation [83]. This method uses the canonical probability density of an approximated harmonic system to generate weighted displacements to solve Eq. 2.94. Accordingly the canonical partition function in Eq. 2.96 for a system with N particles can be simplified to:

$$\begin{aligned} Z &= \int e^{-\beta \left(\sum_I \frac{\mathbf{p}_I \cdot \mathbf{p}_I}{2M_I} + V(\mathbf{R}) \right)} d\mathbf{p} d\mathbf{R} \\ &= \sqrt{\frac{2\pi^{3*N}}{\beta}} \int e^{-\beta V(\mathbf{R})} d\mathbf{R} \end{aligned} \quad (2.140)$$

This is analytically possible since the canonical probability distribution of the kinetic energy is a Gaussian function. Another Monte Carlo method was already introduced in Since the potential is harmonic $V(\mathbf{R}) = \frac{1}{2} \sum_{I,J,\alpha,\beta} \Phi_{IJ}^{\alpha\beta} u_I^\alpha u_J^\beta$ we can easily see that the harmonic displacements obey a normal distribution. Using the harmonic positions, defined in Eq. 2.57, we can calculate the necessary expectation values to write the finite temperature form of the harmonic displacements. For that purpose Eq. 2.57 is rewritten using real functions:

$$\begin{aligned} \mathbf{R}_I(t) - \mathbf{R}_I^{eq} &= +\text{Re} \left(\sum_{\mathbf{q},s} \frac{A_s(\mathbf{q})}{\sqrt{M_I}} \epsilon_{I,s}(\mathbf{q}) e^{i(\mathbf{q} \cdot \mathbf{R}_I - \omega_s(\mathbf{q})t)} \right) \\ \mathbf{u}_I(t) &= \text{Re} \left(\sum_{\mathbf{q},s} \frac{A_s(\mathbf{q})}{\sqrt{M_I}} \epsilon_{I,s}(\mathbf{q}) e^{i(\phi_s(\mathbf{q}) - \omega_s(\mathbf{q})t)} \right) \\ &= \sum_{\mathbf{q},s} \frac{A_s(\mathbf{q})}{\sqrt{M_I}} \epsilon_{I,s}(\mathbf{q}) \cos(\phi_s(\mathbf{q}) - \omega_s(\mathbf{q})t). \end{aligned} \quad (2.141)$$

From this we find that the mode resolved energy in the harmonic approximation is:

$$E_s(\mathbf{q}) = \frac{\omega_s^2(\mathbf{q})}{2} A_s^2(\mathbf{q}). \quad (2.142)$$

Classical Harmonic Sampling

From the equipartition theorem we know that the energy per mode in a harmonic potential¹³ is $\langle E_s(\mathbf{q}) \rangle = k_B T = \frac{\omega_s^2(\mathbf{q})}{2} \langle A_s^2(\mathbf{q}) \rangle$ defining the expectation value of the mean square displacement. The mean square displacement can be used to define the expectation value of the amplitude as:

$$\begin{aligned} \langle A_s(\mathbf{q}) \rangle &= \sqrt{\langle A_s^2(\mathbf{q}) \rangle} \\ \langle A_s(\mathbf{q}) \rangle &= \sqrt{\frac{k_B T 2}{\omega_s^2(\mathbf{q})}} \end{aligned} \quad (2.143)$$

Based on this result, the harmonic displacements are constructed by replacing the time modulation with normally distributed random numbers. This method was first proposed

¹³More general formulations exist e.g. for anharmonic potentials of the form $E_{\text{Pot}} = a_1 * R^2 - \sum_{n>1} a_n u^{2n}$ [133]

in Ref. [83]. To obtain normally distributed random numbers a Box-Muller transformation [84] is applied to two uniformly distributed mode-dependent random numbers ξ_s and ϕ_s :

$$Z_s = \sqrt{-2\ln(\xi_s)}\cos(2\pi\phi_s) \quad (2.144)$$

$$\zeta_s = \sqrt{-2\ln(\xi_s)}\sin(2\pi\phi_s) \quad (2.145)$$

Z_s and ζ_s are then independent, normally distributed random numbers. Based on this result, we can write the harmonic displacements as:

$$\mathbf{u}_I = \sum_{s\mathbf{q}} \epsilon_{I,s}(\mathbf{q}) \sqrt{\frac{2k_B T}{M_I \omega_s^2(\mathbf{q})}} \sqrt{-2\ln(\xi_s)} \cos(2\pi\phi_s). \quad (2.146)$$

Importantly this preserves all expectation values and the displacements vanish in the limit $t \rightarrow 0$ K, as expected for classical nuclei.

Quantum Harmonic Sampling

To account for quantum nuclear fluctuations the Bose-Einstein distribution is used instead of the equipartition theorem. The general idea however is largely the same and only requires finding the appropriate form of $\langle A_s(\mathbf{q}) \rangle$. This is again drawn from the square root of the mean square displacements and is give by:

$$\langle A_s(\mathbf{q}) \rangle = \sqrt{\frac{\hbar(n_s(\mathbf{q}) + 2)}{2M_I \omega_s(\mathbf{q})}} \quad (2.147)$$

Using the same technique as before we can write the quantum harmonic displacements as:

$$\mathbf{u}_I = \sum_{s\mathbf{q}} \epsilon_{I,s}(\mathbf{q}) \sqrt{\frac{\hbar(n_s(\mathbf{q}) + 2)}{2M_I \omega_s(\mathbf{q})}} \sqrt{-2\ln(\xi_s)} \cos(2\pi\phi_s). \quad (2.148)$$

Again all expectation values are preserved, accordingly, the displacements remain finite even in the $t \rightarrow 0$ K limit due to the zero point or vacuum energy. Using Eq. 2.148 to calculate the expectation value $\sqrt{\langle A_s^2(\mathbf{q}) \rangle} = \langle A_s(\mathbf{q}) \rangle$ for $T = 0$ K we find:

$$\langle A_s(\mathbf{q}) \rangle = \sqrt{\frac{\hbar}{M_I \omega_s(\mathbf{q})}} \quad (2.149)$$

Advantages and Disadvantages of Harmonic Sampling

Harmonic sampling as discussed above rapidly produces uncorrelated configurations for which fully anharmonic energies and forces can be calculated for semi-empirical force fields and ab-initio methods alike. However, the harmonic nature of the displacements still

presents an approximation, in which the displacements are always normally distributed. Additionally, quantum nuclear fluctuations can also only be accounted for within the limits of the harmonic approximation only changing the displacements' variance or "spread" by changing the amplitudes from Eq. 2.147. Accordingly tunneling and other QNFs are not present. of the displacements. which can lead to erroneous results which will be demonstrated in chapter 3.

2.2.7 Real Time Correlation Functions

In the previous section, the discussion revolved around how to evaluate the static expectation values of classical and quantum mechanical observables. However many statistical processes are time-dependent. An important case, and the one we shall examine here, is the correlation function of two observables A and B .

Classical Real-Time Correlation Function

The classical real-time correlation function of two observables A and B in the canonical ensemble is given by

$$G_{AB}^{\text{Cl}} = \int e^{-\beta H(\mathbf{R}, \mathbf{p})} A(\mathbf{R}_t, \mathbf{p}_t) B(\mathbf{R}, \mathbf{p}) d\mathbf{R} d\mathbf{p}. \quad (2.150)$$

It describes how the microscopic values of A and B are related at different times. Note that the classical correlation function is symmetric under time reversion, complex conjugation, and under both operations combined [49].

Quantum Real-Time Correlation Function

The quantum real-time correlation function of two operators A and B is again defined using the canonical density matrix introduced in Eq. 2.98 and reads:

$$G_{AB} = \frac{\text{Tr} \left(e^{-\beta H} A e^{\frac{iHt}{\hbar}} B e^{-\frac{iHt}{\hbar}} \right)}{Z} \quad (2.151)$$

However, an alternative formulation exists, i.e. the Kubo-transformed correlation function [72]:

$$\tilde{G}_{AB} = \frac{1}{\beta Z} \int \text{Tr} \left(e^{-(\beta-\lambda)H} A e^{-\lambda H} e^{\frac{iHt}{\hbar}} B e^{-\frac{iHt}{\hbar}} \right) d\lambda \quad (2.152)$$

Both correlation functions are related through their Fourier transforms:

$$G_{AB}(\omega) = \int_{\mathbb{R}} G_{AB}(t) e^{-i\omega t} dt \quad (2.153)$$

$$\tilde{G}_{AB}(\omega) = \mathcal{FT}(\tilde{G}_{AB}(t)) \quad (2.154)$$

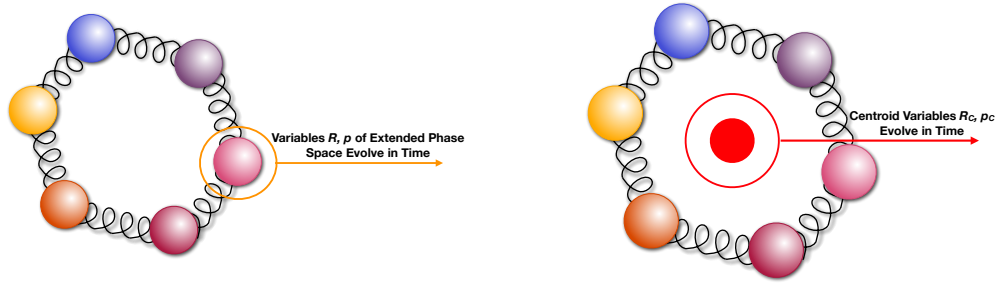


Figure 2.11: Schematics of how the phase space variables evolve in time in Ring Polymer Molecular Dynamics and Centroid Molecular Dynamics.

By evaluating the traces in Eq. 2.151 and 2.152 using the Hamiltonians eigenstates one can show that both correlation functions are related by:

$$G_{AB}(\omega) = \frac{\beta \hbar \omega}{1 - e^{-\beta \omega \hbar}} \tilde{G}_{AB}(\omega) \quad (2.155)$$

However, it can be debated which of the two correlation functions is the true analog to the classical correlation function. A case can be made that the Kubo-transformed correlations functions are more closely related to classical correlation functions as they also full fill the same symmetries, whereas the quantum real-time correlation functions do not [49].

Approximating the Quantum Real Time Correlation Function

However, evaluating any of the real-time quantum correlation functions requires solving the nuclear Hamiltonian in Eq. 2.8 or evaluating the real-time path integral in Eq. 2.121. To avoid these numerical intensive tasks, approximations, in terms of classical trajectories, similar to static PIMD, are sought, to account for quantum nuclear dynamics in the calculation of spectra, transport properties, and reaction rates.

Centroid Molecular Dynamics

One of the earliest approximations is Centroid Molecular Dynamics [79, 80] (CMD). It should be noted that CMD is an ad-hoc defined method and no rigorous derivation for CMD existed until recently. It was shown that CMD can be derived from Matsubara dynamics [82]¹⁴. CMD approximates the Kubo transformed correlation function by evolving the centroid in the potential of mean force generated by the replica, which in normal mode coordinates has the form:

$$U_C(\tilde{q}_0) = -\frac{1}{\beta} \ln \left(\int \prod_{\alpha=1}^{P-1} d\tilde{p}_{\alpha} d\tilde{q}_{\alpha} e^{-\beta P \left(\sum_{\alpha=1}^{P-1} \frac{\tilde{p}_{\alpha} \cdot \tilde{p}_{\alpha}}{2m_{\alpha}} + \sum_{\alpha=1}^{P-1} \frac{m_{\alpha} \omega_{\alpha}^2}{2} \tilde{q}_{\alpha}^2 + \sum_{\alpha=0}^{P-1} V(\mathbf{R}_{\alpha}(\tilde{q})) \right)} \right) \quad (2.156)$$

¹⁴Matsubara dynamics is a higher level approximation with a rigorous derivation. However, its immense computational demand currently prohibits any application.

2 Theory

Accordingly the correlation function of two observables A and B is given by

$$\langle AB \rangle = \frac{1}{Z_{\text{CMD}}} \int e^{-\beta_P(T_C + U_C)} A_C(R_C) B_C(R(t)_C) dR_C dp_C, \quad (2.157)$$

Here the subscript C denotes centroid properties. Technically the potential of mean force is obtained by integrating over all internal ring-polymer modes except the centroid mode. Effectively this is archived by decreasing the mass of the ring-polymer replicas, which increases their frequencies. This leads to an adiabatic decoupling of the centroid- and all other ring-polymer modes. CMD has many desirable qualities [78]:

- It fulfills the same symmetries as the Kubo transformed correlation function
- It is exact in the harmonic approximation for linear position-dependent observables.
- It is exact in the limit $t \rightarrow 0$ for linear-position dependent observables

However, this method also has its caveats.

- CMD suffers from the "curvature" problem since the centroid can move into unphysical positions. In practice, this is known as a shift and broadening in the peaks of spectras [81]
- The time steps have to be chosen small enough for the centroid to follow the changes in the effective potential. This leads to higher computational costs compared to the alternatives below.
- While CMD is exact in the harmonic approximation it is less accurate for highly anharmonic potentials [82].
- CMD also does not include quantum coherence effects
- Nonlinear and momentum-dependent estimators can be problematic.

Ring Polymer Molecular Dynamics

Another popular method to calculate real-time quantum correlation functions is Ring Polymer Molecular Dynamics (RPMD) [74]. Similar to CMD, RPMD is an Ad-Hoc defined method and can only be derived from Matsubara dynamics [82] In contrast to CMD, RPMD emulates a microcanonical ensemble. Accordingly, the internal modes of the ring polymer are not thermalized and the replica masses are equal to the physical masses. RPMD is based on the observation that if one tries to calculate the static expectation values of two position-dependent estimators $A_P(R)$ and $B_P(R)$ using PIMD the resulting expression

$$\langle AB \rangle_P = \frac{1}{(2\pi\hbar)^P Z_P} \int e^{-\beta_P H_P} A_P(R) B_P(R(t)) dR dp, \quad (2.158)$$

yields the $t \rightarrow 0$ limit of the Kubo-transformed correlation function (Eq. 2.152). Furthermore, Eq. 2.158 not only shares the same symmetries as the Kubo-transformed correlation function but is also exact in the classical limit and the harmonic approximation for linear position-dependent estimators. Identical to PIMD the equations of motions are generated by the ring polymer Hamiltonian 2.131 and are given by Eq. (2.132). Accordingly, the time steps do not have to be reduced in contrast to CMD. RPMD has successfully been applied to calculate reaction rates [75] and transport coefficients, such as diffusion coefficients [76]. However, the method also suffers from certain drawbacks:

- Does not include quantum coherence effects
- Problematic for highly anharmonic potentials
- Problematic for nonlinear and momentum-dependent estimators
- Ring Polymer modes can erroneously resonate with physical modes [81], leading to spurious splitting of peaks in spectra.
- Harmonic springs coupling the replicas stiffen thus RPMD is highly non-ergodic and requires many trajectories.

Thermostatted Ring Polymer Molecular Dynamics

Thermostatted Ring Polymer Molecular Dynamics (TRPMD) is an extension of RPMD and bridges the gap between it and CMD. The motivation to do so was to address RPMD's resonance and CMD's curvature problem. By demonstrating that CMDs' curvature problem originates from decreasing the masses [77], since (T)RPMD uses the physical masses instead neither exhibits the curvature problem [77]. The spurious resonance is removed by attaching a path integral Langevin thermostat (PILE) [167] to the internal ring polymer modes [77], thus dampening their vibrations. For the free ring polymer the dampening parameters γ are given by:

$$\gamma^{\alpha>0} = 2\omega_\alpha \quad (2.159)$$

$$\gamma^0 = \frac{1}{\tau_0}. \quad (2.160)$$

Here α numerates the ring polymer modes ω_α and τ_0 the relaxation time. Importantly, this approach retains all features proven about RPMD, which means that estimators derived for RPMD can also be applied to TRPMD. Furthermore, the practical application of TRPMD is straightforward since the thermostat can easily be detached from the centroid mode by choosing a sufficiently high relaxation time. An additional advantage of attaching a thermostat to the internal ring polymer modes is that the resulting dynamics are significantly more ergodic compared to RPMD. However, the thermostat can lead to an artificial peak broadening in vibration spectra. How the PILE thermostat works are explored in more detail in appendix D.2.

2.3 Measuring Anharmonicity

So far we mainly discussed MD/PIMD methods that allow to inclusion anharmonic effects. However, how pronounced the anharmonic effects are in different materials at different temperatures. To this end, an anharmonicity measure was recently introduced [112]. The basic idea is to sample the PES at a finite temperature and use the forces to measure to which extent the PES is anharmonic. However, since results obtained from the bare forces would not be comparable for different materials a normalization scheme was developed. The normalization schemes is derived from the thermodynamic average of the force components $\langle F_{I,a} \rangle$ and the associated associated probability density function $\rho(F)$:

$$\sum_{I,a} \langle F_{I,a} \rangle = \frac{1}{N_I} \int_{\mathcal{R}} F \rho(F) dF. \quad (2.161)$$

The probability density function $\rho(F)$ can be represented using the Dirac delta distribution and takes the form:

$$\rho_I^a(F) = \frac{1}{N_t} \sum_t \delta(F - F_I^a(t)) \quad (2.162)$$

$$\rho(F) = \frac{1}{3N_I} \sum_{I,a} \rho_I^a(F), \quad (2.163)$$

where N_t is the number of time steps, t the time, N_I the number of nuclei, and F the forces. We can generalize the rest of the original definition, shown in Ref. [112], to PIMD. The required force estimator can easily be derived from the PIMD equations of motion in Eq. 2.132 and takes the form:

$$\mathbf{F}_I^C = \frac{1}{P} \sum_{\alpha} \left(\underbrace{\frac{M_I}{\beta_P^2 \hbar^2} (2\mathbf{R}_{I,\alpha} - \mathbf{R}_{I,\alpha-1} - \mathbf{R}_{I,\alpha+1})}_{\mathbf{F}_{I,\alpha}^{\text{RP}}} - \frac{\partial V(\mathbf{R}_{I,\alpha})}{\partial \mathbf{R}_{I,\alpha}} \right) \quad (2.164)$$

Here $\mathbf{F}_{I,\alpha}^{\text{RP}}$ describes the ring-polymer forces between nuclei in neighbouring replicas, $-\frac{\partial V(\mathbf{R}_{I,\alpha})}{\partial \mathbf{R}_{I,\alpha}}$ the physical forces within each replica, P is the number of replicas in the ring-polymer, and $\alpha \in [0, P]$ are the replica indices. The forces \mathbf{F}_I^C are also referred to as the centroid forces. Once the sum in Eq. 2.164 is carried we find that the contribution from the ring-polymer forces vanishes, due to its cyclic boundary conditions $P + 1 = 1$. We use the definition of $\mathbf{F}_{I,\alpha}$ in Eq. 2.164 to generalize Eq. 2.162 to PIMD, which takes

the form:

$$\rho_{I,\alpha}^a(F) = \frac{1}{N_t} \sum_t \delta(F - F_{I,a}^\alpha(t)) \quad (2.165)$$

$$\rho(F) = \frac{1}{3N_I} \sum_{I,a} \sum_{\alpha} \rho_{\alpha,I}^a(F). \quad (2.166)$$

In Ref. [112] the standard deviation $\sigma(F) = \sqrt{\int_{\mathcal{R}} F^2 \rho(F) dF}$ was identified as the *natural scale* of the forces. Based on the force estimator presented in Eq. 2.164, we can write the *natural scale* for the forces to PIMD as:

$$\sigma(F) = \sqrt{\int_{\mathcal{R}} F^2 \rho(F) dF} \quad (2.167)$$

$$= \sqrt{\frac{1}{3N_I P^2} \sum_{I,a} \langle (F_{I,a}^\alpha)^2 \rangle}. \quad (2.168)$$

This will become relevant shortly, Based on this the anharmonicity is measured as:

$$\sigma^A = \sqrt{\frac{\sum_{I,a} \langle (F_{I,a}^A)^2 \rangle}{\sum_{I,a} \langle (F_{I,a}^\alpha)^2 \rangle}}. \quad (2.169)$$

Here F_I^α are the purely anharmonic centroid forces defined as:

$$\mathbf{F}_I^\alpha = \mathbf{F}_I^\alpha - \mathbf{F}_I^\alpha \quad (2.170)$$

The harmonic centroid force $F^{\text{C-HA}}$ are obtained from the displacements around the equilibrium positions and are given by:

$$\mathbf{F}_I^\alpha = \sum_J \Phi_{IJ} \cdot \mathbf{u}_{J\alpha}. \quad (2.171)$$

Accordingly, Eq. 2.169 measures the contribution of anharmonicity relative to the forces \mathbf{F} by subtracting the harmonic contribution of the force from the full force. In the publication, it is suggested to categorize materials as harmonic if the anharmonicity score at a given temperature is less than 0.3. While this statement is true, the next chapter will show that materials with $\sigma^A \approx 0.3$ can already exhibiting strongly anharmonic dynamics.

Harmonic Analysis

The completeness of the eigenvectors $\epsilon_s(\mathbf{q})$ of the dynamical matrix defined in Eq. (2.56) allows to analyze (PI)MD trajectories on a qualitative level by projecting it onto the eigenmodes of the dynamical matrix thus allowing mode-specific resolution of atom specific quantities. Note that, the projection of a (PI)MD trajectory implicitly includes higher

2 Theory

orders of anharmonicity. The implementation is straightforward and only requires the Hessian and basically relies on inverting the ansatz to solve the harmonic equations of motion in Eq. (2.55). Two important examples are the displacements of the atoms around their equilibrium position and the velocities. Their projections, in a finite size super cell are given by:

$$u_S(t) = \frac{1}{N} \sum_I \epsilon_S^I \cdot \mathbf{u}_I(t) \quad (2.172)$$

$$v_S(t) = \frac{1}{N} \sum_I \epsilon_S^I \cdot \mathbf{v}_I(t). \quad (2.173)$$

Here N is the number of atoms in the supercell, I the I 'th atom in the supercell, ϵ_S^I the eigenvector of the dynamical matrix, and S one of the $3N$ vibrational modes that are commensurate with the supercell. The projected displacements and velocities can be mapped back into the first Brillouin zone. For that it is useful to express the index I using periodic boundary conditions as $I \rightarrow n\hat{I}$, where \hat{I} is the \hat{I} 'th atom in the primitive unit cell and n the n 'th periodic image shifted by the translation vector \mathbf{T}_n . The commensurate wave vectors \mathbf{q} and \mathbf{T}_n determine the phase factor $e^{-i\mathbf{q}\cdot\mathbf{T}_n}$. The mapping of the projected displacements and velocities is given by:

$$u_s(\mathbf{q}, t) = \frac{1}{\hat{N}} \sum_{n\hat{I}} e^{-i\mathbf{q}\cdot\mathbf{T}_n} \epsilon_s^{\hat{I}}(\mathbf{q}) \cdot \mathbf{u}_{n\hat{I}}(t) \quad (2.174)$$

$$v_s(\mathbf{q}) = \frac{1}{\hat{N}} \sum_{n\hat{I}} e^{-i\mathbf{q}\cdot\mathbf{T}_n} \epsilon_s^{\hat{I}}(\mathbf{q}) \cdot \mathbf{v}_{n\hat{I}}(t). \quad (2.175)$$

Here \hat{N} is the number of atoms in the primitive unit cell and s denotes the $3\hat{N}$ vibrational modes. The tuple (\mathbf{q}, s) is equivalent to the mode index S from Eq. 2.172 and 2.173. As is proven in App. B this is also applicable to PIMD:

$$u_s^\alpha(\mathbf{q}, t) = \frac{1}{\hat{N}} \sum_{n\hat{I}} e^{-i\mathbf{q}\cdot\mathbf{T}_n} \epsilon_s^{\hat{I}}(\mathbf{q}) \cdot \mathbf{u}_{n\hat{I}}^\alpha(t) \quad (2.176)$$

$$v_s^\alpha(\mathbf{q}) = \frac{1}{\hat{N}} \sum_{n\hat{I}} e^{-i\mathbf{q}\cdot\mathbf{T}_n} \epsilon_s^{\hat{I}}(\mathbf{q}) \cdot \mathbf{v}_{n\hat{I}}^\alpha(t). \quad (2.177)$$

Here α denotes the α 'th ring-polymer replica.

Mode Resolved Anharmonicity Score

The completeness of the eigenvectors $\epsilon_s(\mathbf{q})$ of the dynamical matrix defined in Eq. (2.56) also allows for mode-resolved analysis of (PI)MD forces:

$$F_s(\mathbf{q}) = \frac{1}{N} \sum_{n\hat{I}} \frac{1}{M_{\hat{I}}} e^{-i\mathbf{q}\cdot\mathbf{T}_n} \epsilon_s^{\hat{I}}(\mathbf{q}) \cdot \mathbf{F}_{n\hat{I}}(t). \quad (2.178)$$

This allows to calculate a mode-resolved anharmonicity score, its functional form is very similar to $\sigma_s^A(\mathbf{q})$ as defined in Eq. 2.169:

$$\sigma_s^A(\mathbf{q}) = \sqrt{\frac{\langle (\mathbf{F}_s(\mathbf{q}) - \mathbf{F}_s^{\text{HA}}(\mathbf{q}))^2 \rangle}{\langle \mathbf{F}_s^2(\mathbf{q}) \rangle}}. \quad (2.179)$$

In Ref. [112] σ^A was defined even more generally by the formula:

$$\sigma^A = \sqrt{\frac{\sum_{I\alpha} \langle (\mathbf{F}_{I\alpha X} - \mathbf{F}_{I\alpha X}^{\text{HA}})^2 \rangle}{\sum_{I\alpha} \langle \mathbf{F}_{I\alpha X}^2 \rangle}}. \quad (2.180)$$

Here X can be either a vibrational mode n , a group of atoms, or even a single atom [112].

3 The Interplay of Quantum Nuclear and Anharmonic Fluctuations

To this day, the impact of quantum nuclear fluctuations (QNFs) on the degree of anharmonicity is still not widely understood. For instance, it is still common to assume that quantum nuclear fluctuations are only important at low temperatures and that anharmonic effects are negligible at these temperatures. Similarly, it is often assumed that the classical, i.e. $T \rightarrow \infty$, limit is generally applicable at elevated temperatures. A number of publications suggest that a complex interplay between quantum nuclear fluctuations and anharmonic effects exists, e.g. for the thermal expansion [122], for the relative stability of different structural phases [123], and for the thermal conductivity [121, 120]. However, most of these studies focus on a specific observable and material. Here we establish a more general picture by quantifying the degree of anharmonicity first. To this end, we generalized the definition of the anharmonicity measure [112], introduced in Sec. 2.3, to path integral MD (PIMD). Finally, we analyze the implication of our findings for thermal conductivity.

3.1 Validation of the Anharmonicity Score

For validation of the generalized anharmonicity score, we chose solid Lennard-Jones Argon and Tersoff Silicon from 0 to 60 and 700 Kelvin respectively. Both force fields are well understood, and well-performing implementations for both are readily available as part of LAMMPS [143]. Most importantly Tersoff Silicon and Lennard-Jones Argon are examples of highly harmonic and anharmonic materials, respectively. Before proceeding, both systems will be discussed briefly to establish a baseline, comparing predictions obtained from the toy models to experiments as well as a selection of different DFT XC functionals using the FHI-aims *ab initio* materials simulation package [100]. For that purpose, the phonon band structures [91] and thermal expansion coefficients were calculated for both systems using the Tersoff and Lennard-Jones potentials respectively. As explained in Sec. 2.2.1 calculating this, requires the harmonic force constants $\Phi_{IJ}^{\alpha\beta}$, i.e., the Hessian of the potential energy surface. In this work, a finite difference approach, as proposed by Parlinski, Li, and Kawazoe [90] and implemented in the *phonopy* package [91], was used. From the forces $\mathbf{F}_I(\Delta\mathbf{R}_J)$ acting on the individual atoms I under a small displacement $\Delta\mathbf{R}_J$ of

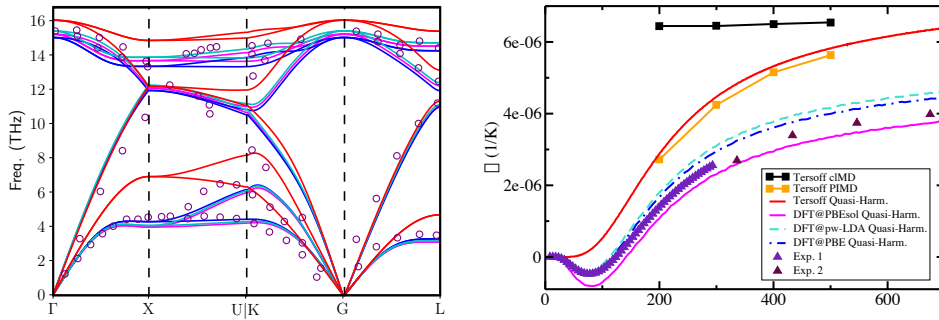


Figure 3.1: Phonon band structures (left) and thermal expansion coefficients (right) for diamond silicon. The band structure was calculated using the Tersoff potential (red) and DFT PBEsol (magenta), PBE (blue), and PW-LDA (cyan) XC-functionals. Neutron scattering experiments taken from Ref. [125] (open maroon circles) are shown as well. The thermal expansion coefficient was extracted from the quasi-harmonic approximation (all methods), classical MD (black squares, Tersoff only), and PIMD (orange squares, Tersoff only) and compared to Twyman-Green interferometry (violet triangles [126]) and X-ray diffraction (blue triangles [127]).

atom J from its equilibrium position the Hessian is calculated by evaluating the forward finite difference:

$$\Phi_{IJ}^{\alpha\beta} = \frac{\partial E}{\partial R_I^\alpha \partial R_J^\beta} = \frac{\partial F_I^\alpha}{\partial R_J^\beta} \approx \frac{F_I^\alpha(\delta R_J^\beta)}{\delta R_J^\beta}. \quad (3.1)$$

The thermal expansion was calculated based on the quasi-harmonic approximation [86] and fully anharmonic NPT cl and PIMD simulations using the I-PI (PI)MD code [142]. In the latter cases, the nuclei were propagated in 1 fs steps, to which a stochastic velocity re-scaling thermostat was used [61]. The results are then compared to different XC-functionals and van der Waals correction schemes (Silicon: PW-LDA [28], PBE [29], and PBEsol [30]; Argon: TS@PBE [102] and MBD@PBE [103, 104]) as well as experimental results.

3.1.1 Vibrational Properties of Tersoff Silicon

As discussed in Sec. 2.1.1, the necessary parameters to model silicon using the Tersoff potential are provided as part of the LAMMPS package [143] but were first introduced in Ref. ???. For all Tersoff simulations, a cubic $6 \times 6 \times 6$ supercell containing 1728 atoms was used while all DFT simulations were performed in a cubic $2 \times 2 \times 2$ containing 64 atoms as well as a dense $6 \times 6 \times 6$ k-grid. The phonon band structures and thermal

expansion coefficients are shown in Fig. 3.1. Both properties are relevant for this work since high-frequency phonons can indicate active quantum nuclear fluctuations at elevated temperatures while the thermal expansion allows for (limited) insight into the degree of anharmonicity.

While, Silicon exhibits high frequent optical modes it only exhibits a small thermal expansion, due to its highly harmonic nature. Qualitatively, the results are the same for all levels of theory. Both PIMD and the quasi-harmonic approximation predict a nonlinear temperature-dependent function for the thermal expansion due to the inclusion of QNFs particularly zero-point motion which induces a renormalization of the temperature-dependent lattice constants at lower temperatures. Conversely, the thermal expansion obtained from classical MD is almost constant since the classical lattice expands completely linearly. However comparing all predictions, obtained from the Tersoff potential, to experimental results uncovers that both the phonon dispersion relation, especially at high frequencies, as well as the thermal expansion, are highly overestimated, furthermore the Tersoff potential fails to predict the negative thermal expansion at low temperatures. Conversely, DFT results for the phonon dispersion relation and thermal expansion, are generally in much better agreement with the experimental results for example correctly modeling the negative thermal expansion at low temperatures. However this should not insinuate that choice of the functional is irrelevant, on the contrary, pw-LDA, PBE, and PBEsol predictions still differ quite drastically. While the predicted band structures agree with experimental results (with a slight bias towards pw-LDA), the thermal expansion coefficients, calculated using the pw-LDA and PBE XC-functionals respectively, are in better agreement with the experiment below 200 K compared to PBEsol. Conversely, PBEsol results are in better agreement with experimental results above 200 K.

3.1.2 Vibrational Properties of Solid Lennard-Jones Argon

Since the outer shell of argon atoms is completely filled it usually neither forms ionic nor covalent bonds¹. Accordingly, the atoms in an Argon crystal do not form chemical bonds and are held together by van der Waals interactions described by a pairwise Lennard-Jones potential. We use the Lennard-Jones parameters introduced in Ref [128] ($\epsilon = 0.010325$ (eV), $\sigma = 3.405$ (Å)) and a 13 (Å) cutoff radius for the interactions. As explained in Sec. 2.1.3 semi-local XC-functionals do not account for the long-range nature of van der Waals interactions. Accordingly, correction schemes have to be applied to most DFT calculations. For purposes of comparison, both the Tkatchenko-Scheffler (TS) and many-body dispersion (MBD) correction schemes were used on top of the PBE XC-functional. The results are shown in Fig. 3.2. In contrast to the previously discussed silicon, the phonon band structures obtained using either TS@PBE or MBD@PBE are not more accurate compared to the band structure calculated using the Lennard-Jones potential which appears to agree best

¹While only some compounds have been synthesized successfully e.g. argon hydrofluoride [129] which exhibits weak chemical bonds, CCSD(T) and MP2 calculations predict the existence of different carbon/silicon-argon compounds [130].

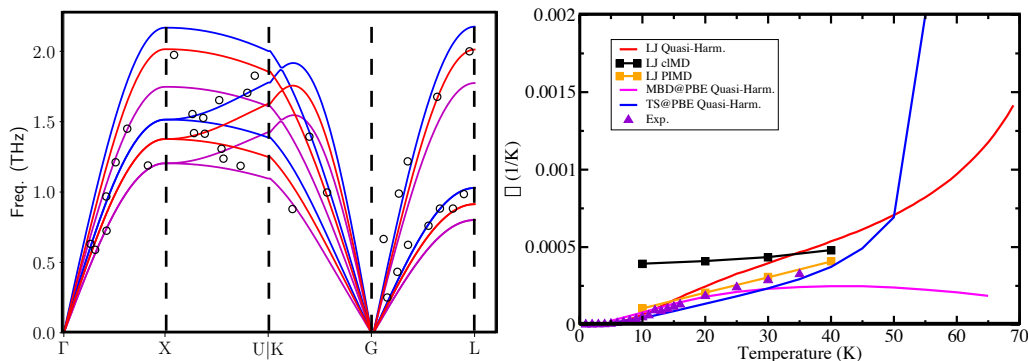


Figure 3.2: The left image shows the phonon band structure of solid Argon obtained from the Lennard-Jones potential (red), DFT@PBE@mbd (magenta), and DFT@PBE@TS (blue) in comparison with experimental results [131] (open black circles) obtained from neutron scattering. The right image shows the corresponding thermal expansion coefficients calculated from the quasi-harmonic approximation (the same color coding as for the band structures applies), classical MD (black squares and line), and PIMD (orange squares and line) in comparison with experimental results [132] (violet triangles) using a parallel-plate capacitance dilatometer

with the experimental results. Conversely, the results of the quasi-harmonic approximation, based on DFT, appear to be in better agreement with the experimental results compared to the quasi-harmonic results obtained from the Lennard-Jones potential. However, this also illustrates the shortcomings of the quasi-harmonic approximation, while it serves as a useful approximation even for highly anharmonic materials as it does include high orders of anharmonicity, it is still only an extension of the harmonic approximation. This is evident if the Lennard-Jones PIMD results are taken into account which agree much better with the experimental results. However, this does not indicate that the quasi-harmonic thermal expansion obtained from MBD@PBE and TS@PBE is meaningless. Quite on the contrary, the quasi-harmonic thermal expansion based on TS@PBE seems to diverge above 50 (K) while MBD@PBE predicts a decrease in the thermal expansion. This can be an indication of a phase transition that would be roughly in line with the melting temperature of solid Argon at 83 (K). The same behavior can also be observed in the Lennard-Jones based quasi-harmonic results above 60 (K).

3.1.3 The Anharmonicity Score Tested on Tersoff Silicon and Lennard-Jones Argon

To test its PIMD formulation and also illustrate the methods used, the anharmonicity scores for Lennard-Jones argon and Tersoff silicon were calculated using different methods for exploring the PES. We used classic and quantum harmonic sampling, (classical)MD, and PIMD. Additionally, we calculated the anharmonicity score along multiple harmonic PIMD trajectories, calculating the anharmonic forces from uncorrelated snapshots using the Lennard-Jones and Tersoff potentials. This is mathematically equivalent to quantum

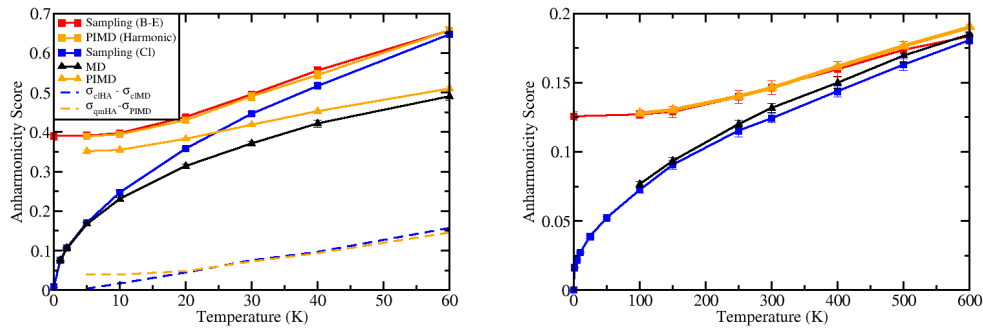


Figure 3.3: The images show the anharmonicity score of Lennard-Jones Argon (left) and Tersoff Silicon (right) computed from harmonic sampling using the Bose-Einstein distribution (solid red line) or equipartitioning (solid blue line), classical MD (solid black line and triangles) and PIMD (orange solid line with triangles squares indicate harmonic PIMD) together with the difference between harmonic and anharmonic sampling.

harmonic sampling and thus presents an valuable tool for validation, since the average anharmonicity score must be the same for both methods. The results are shown in Fig. 3.3 for Lennard-Jones Argon and Tersoff Silicon.

Tersoff Silicon

For Tersoff Silicon we find that the anharmonicity score extracted along clMD trajectories σ_{clMD}^A , increases approximately proportional to \sqrt{T} across the entire temperature range. This is a direct consequence of the \sqrt{T} temperature dependence of the atomic displacements in the harmonic approximation.

Theorem 3.1.1. *Let the interatomic force F_I be $n + 1$ times differentiable and $n > 2$ always be an odd integer. Also, let all non-harmonic contributions be small compared to the harmonic contribution. Then $\sigma^A \sim \sqrt{T}$ in first-order perturbation theory and for classical nuclei.*

Proof. Since the inter atomic force F_I are $n + 1$ times differentiable we can expand them in a Taylor polynomial:

$$\mathbf{F}_I = \sum_{IJ} \Phi_{IJ} \mathbf{u}_J + \sum_{JK} \Psi_{IJK} \mathbf{u}_J \mathbf{u}_K + \mathcal{O}(u^3) \quad (3.2)$$

Here Φ_{IJ} and Ψ_{IJK} are the second and third-order force constants respectively and \mathbf{u}_I the displacements of the I 'th atom. In first-order perturbation theory, the displacements are taken to be harmonic. Thus we can assume that the equipartition theorem holds true and

that $\langle \sqrt{\mathbf{u}_I^2} \rangle \sim \sqrt{T}$. Accordingly, for the anharmonicity score we find that:

$$\frac{\sqrt{\sum_I \langle (\mathbf{F}_I - \mathbf{F}_I^{\text{HA}})^2 \rangle}}{\sqrt{\sum_I \langle \mathbf{F}_I^2 \rangle}} = \frac{\sqrt{\sum_I \langle (\sum_{JK} \Psi_{IJK} \mathbf{u}_J \mathbf{u}_K + \mathcal{O}(\mathbf{u}^3))^2 \rangle}}{\sqrt{\sum_I \langle (\sum_J \Phi_{IJ} \mathbf{u}_J + \mathcal{O}(\mathbf{u}^2))^2 \rangle}} \quad (3.3)$$

$$\sim \frac{\mathcal{O}(T)}{\mathcal{O}(\sqrt{T})} \quad (3.4)$$

$$= \mathcal{O}(\sqrt{T}). \quad (3.5)$$

Accordingly, σ^{A} is approximately proportional to \sqrt{T} □

Comparing the results for $\sigma_{\text{clMD}}^{\text{A}}$ to the anharmonicity scores obtained from classical harmonic sampling $\sigma_{\text{clHA}}^{\text{A}}$, reveals that $\sigma_{\text{clMD}}^{\text{A}} = \sigma_{\text{clHA}}^{\text{A}}$, which demonstrates the highly harmonic nature of Tersoff Silicon. Using the same line of thought as in proof 3.1.3 we find that Accounting for quantum-nuclear through quantum-harmonic sampling leads to an increase of the anharmonicity $\sigma_{\text{qmHA}}^{\text{A}}$ up to 400 K. Above 500 K the increase due to QNFs is still visible but less pronounced compared to lower temperatures since we approach the classical limit. This is confirmed by calculating the anharmonicity score $\sigma_{\text{PIMD}}^{\text{A}}$ from PIMD, which serves as a first conformation for the generalization of σ^{A} to PIMD. The increase in anharmonicity is driven by the zero-point motion since there are no differences between PIMD and quantum-harmonic sampling. Importantly zero-point motion also leads to a finite anharmonicity at 0 K. Additionally, we find that the classical limit is recovered by $\sigma_{\text{PIMD}}^{\text{A}}$ above 500 K. In contrast to $\sigma_{\text{clMD/clHA}}^{\text{A}}$ the functional form of $\sigma_{\text{PIMD/qmHA}}^{\text{A}}$ is proportional to $\sqrt{(n+1/2)}$ where n is the Bose-Einstein distribution.

Lennard-Jones Argon

In Lennard-Jones Argon we again see the same approximate \sqrt{T} temperature dependence of $\sigma_{\text{clHA}}^{\text{A}}$. However, it is immediately clear that Lennard-Jones Argon is highly anharmonic, since $\sigma_{\text{clHA}}^{\text{A}}(T > 30\text{K}) > 0.3$. This is confirmed by comparing $\sigma_{\text{clHA}}^{\text{A}}$ and $\sigma_{\text{clMD}}^{\text{A}}$, which shows that classical harmonic sampling significantly overestimates the anharmonicity above 20 K. We also see that the difference $\sigma_{\text{clHA}}^{\text{A}} - \sigma_{\text{clMD}}^{\text{A}}$ exhibits a linear temperature dependency and vanishes below 5 K. Quantum nuclear fluctuations then increase the anharmonicity for temperatures below 60 K, becoming more pronounced as the temperature decreases. Thus the highest increase due to QNFs is observed in the $T \rightarrow 0$ K limit, where Lennard-Jones Argon exhibits an anharmonicity score between 0.35-0.40 due to zero-point motion. Accordingly, Lennard-Jones Argon cannot be regarded as harmonic at any temperature. Similar to classical harmonic sampling, we observe that quantum harmonic sampling overestimates the anharmonicity compared to PIMD. However, QNFs lead to an overestimation at all investigated temperatures, including the low-temperature limit. Finally the difference $\sigma_{\text{qmHA}}^{\text{A}} - \sigma_{\text{PIMD}}^{\text{A}}$ no longer exhibits a linear temperature

dependence but becomes constant below 20 K, only exhibiting a linear temperature-dependence above 20 K. This serves as the basis for another test to validate $\sigma_{\text{PIMD}}^{\text{A}}$ by propagating the nuclei in a harmonic potential, using PIMD, one can generate samples that are mathematically equivalent to those generated by quantum harmonic sampling. By calculating the anharmonic forces at uncorrelated snapshots along the trajectory, $\sigma_{\text{qmHA}}^{\text{A}}$ is recovered using our $\sigma_{\text{PIMD}}^{\text{A}}$ implementation. Importantly, we see that the values of $\sigma_{\text{clMD}}^{\text{A}}$ and $\sigma_{\text{clHA}}^{\text{A}}$ are both recovered by $\sigma_{\text{PIMD}}^{\text{A}}$ in the Lennard-Jones and harmonic potentials respectively.

The Road so Far : These two examples not only served to test the applicability and implementation of $\sigma_{\text{PIMD}}^{\text{A}}$, but also establish whether there is any knowledge to be gained. Indeed we find that accounting for quantum nuclear fluctuations leads to an increased anharmonicity in Tersoff Silicon and Lennard-Jones Argon. The inclusion of zero-point motion alone causes a finite degree of anharmonicity even at 0 K. In Tersoff Silicon we see that quantum harmonic sampling yields the same results as PIMD and that at 0 K $\sigma_{\text{qmHA}}^{\text{A}} = \sigma_{\text{PIMD}}^{\text{A}} = 0.13$. While quantum nuclear fluctuations remain visible even at high temperatures quantum harmonic sampling and PIMD remain indistinguishable. Conversely, in Lennard-Jones Argon the 0 K anharmonicity is larger than 0.35 making it highly anharmonic at all temperatures. This limits the applicability of harmonic sampling techniques which overestimate the anharmonicity in Lennard-Jones Argon. If the nuclei are treated as classical particles this overestimation increases linearly due to anharmonic effects, however, if quantum nuclear fluctuations are accounted for that overestimation is constant up to 20 K. Accordingly, we can conclude that the temperature-independent zero-point motion dominates the nuclear motion up to 20 K. However, anharmonic effects also influence the zero-point motion, which is fully accounted for in PIMD but not at all in quantum harmonic sampling. Fortunately, the anharmonic displacement probability density can be written down explicitly in terms of a Gram-Charlier expansion of the harmonic displacement probability density [162]²:

$$\langle \rho^{\text{HA}}(\mathbf{u}) \rangle = \sum_I \frac{1}{(2\pi \text{var}(\mathbf{u}_I))^{3/2}} \exp\left(-\frac{\sum_J \mathbf{u}_J^2}{2\text{var}(\mathbf{u}_I)}\right). \quad (3.6)$$

The anharmonic displacement probability density is then given by:

$$\langle \rho(\mathbf{u}) \rangle = \left[1 + \frac{1}{2!} C^{ab} \frac{\partial^2}{\partial \mathbf{u}_a \partial \mathbf{u}_b} + \dots \right] \sum_I \frac{1}{(2\pi \text{var}(\mathbf{u}_I))^{3/2}} \exp\left(-\frac{\sum_J \mathbf{u}_J^2}{2\text{var}(\mathbf{u}_I)}\right). \quad (3.7)$$

The displacements are expanded around the harmonic probability distribution, which is always normally distributed. Conversely, the anharmonic corrections are given by Hermite polynomials and, in the lowest order, enter via the coefficient C_{ab} . Accordingly, the zero-

²Here we assumed a cubic symmetry with space group 225 in which all odd terms are zero. A Gram-Charlier expansion cannot reliably be applied to highly anharmonic materials since the magnitude of the coefficients C has to decrease compared to all previous orders.

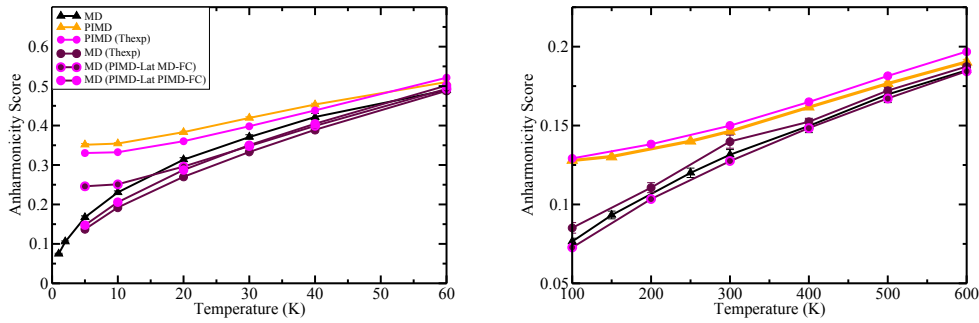


Figure 3.4: This image shows the Anharmonicity Score for Lennard-Jones Argon (left) and Tersoff Silicon (right) without thermal expansion for classical MD and PIMD (denoted as triangles). Compared to results accounting for thermal expansion (denoted as circles).

point motion is proportional to $\frac{1}{\sqrt{\omega}} + \frac{C_{ab}}{2\omega} + \dots$, which is accounted for in PIMD but not in quantum harmonic sampling for which $C_{ab} = 0$. In the case of Lennard-Jones Argon, this results in an overestimated anharmonicity, which demonstrates that quantum nuclear fluctuations and anharmonic effects cannot always be investigated separately. Conversely, above 20 K we see that the overestimation by quantum and classical harmonic sampling becomes indistinguishable. However, until this point thermal expansion was neglected, yet including it is paramount if real materials are to be investigated. Furthermore as shown in Sec. 3.1.1 and 3.1.2, the inclusion of quantum nuclear fluctuations has a pronounced effect on the thermal expansion leading to a renormalization of the lattice parameters.

To investigate its impact on the anharmonicity scores of Lennard-Jones argon and Tersoff silicon, the lattice parameter were relaxed in the NPT ensemble using a Langevin barostat [166] and pile-1 [167] thermostat for PIMD for cIMD a Langevin thermostat was chosen instead of the pile-1 thermostat. All simulations ran a total of 20000 fs per temperature of which, 10000 fs were discarded as thermalization. Due to the low computational cost of these simulations, the timesteps were always set to 1 fs. Both the thermostat and barostat ha using the results to calculate the matching harmonic force constants and anharmonic forces from additional cl and PIMD trajectories. Additional cIMD simulations at PIMD lattice constants were performed to investigate how the lattice renormalization, induced by QNFs, impacts the anharmonicity score. The resulting anharmonicity scores are shown in fig 3.4. Thermal expansion only has a minimal impact on the anharmonicity of Tersoff silicon. We observe the same qualitative and quantitative behavior as previously and neither the lattice constant nor the corresponding harmonic force constants have a pronounced influence. Conversely, thermal expansion has to be accounted for in more anharmonic materials such as Lennard-Jones Argon, which exhibits a thermal expansion two orders of magnitudes larger than the thermal expansion observed in Tersoff Silicon. We immediately can see, that not accounting for thermal expansion leads to an overestimated

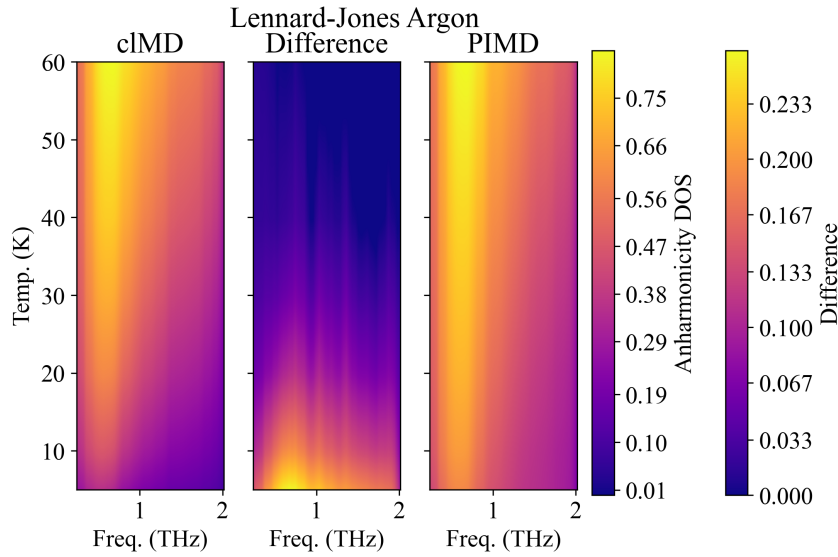


Figure 3.5: The anharmonicity density of states of Lennard-Jones Argon (left clMD, right PIMD) as well as the difference between both (middle).

anharmonicity compared to clMD and PIMD simulations that include thermal expansion. If the anharmonicity along clMD trajectories at PIMD lattice constants is calculated using harmonic force constants at the clMD lattice constants, its shape resembles that of the $\sigma_{\text{PIMD}}^{\text{A}}$. Conversely, if the anharmonicity is calculated with force constants at the PIMD lattice constants, the results are consistent with the anharmonicity along clMD trajectories at clMD lattice constants. These two examples show that thermal expansion has to be included for anharmonic materials such as Lennard-Jones Argon but has almost no impact on harmonic materials like Tersoff Silicon. We also saw that the renormalization of the lattice parameter due to quantum nuclear fluctuations does not impact the observed anharmonicity if the force constants are consistent with the parameters. The observed renormalization of the anharmonicity along clMD trajectories at PIMD lattice constants is not a consequence of the renormalized lattice constant but an artifact introduced by the harmonic force constants. Since they were calculated at the clMD lattice constants, they were not consistent with the PIMD lattice constants. This shows that the employed force constants have to be consistent with the lattice constants at which the cl and PIMD trajectories are run.

The Mode-Resolved Anharmonicity Score

The anharmonicity scores of Lennard-Jones Argon and Tersoff Silicon already show that QNFs can have a pronounced impact on the anharmonicity and vice versa. However, we can gain a deeper understanding by investigating which modes are most influenced by the inclusion of QNFs. This can be accomplished, by projecting the forces into reciprocal space, as explained in Sec 2.3, from which the mode-resolved anharmonicity score in Eq. 2.179, can be extracted. To precisely see which frequencies contribute the most to the

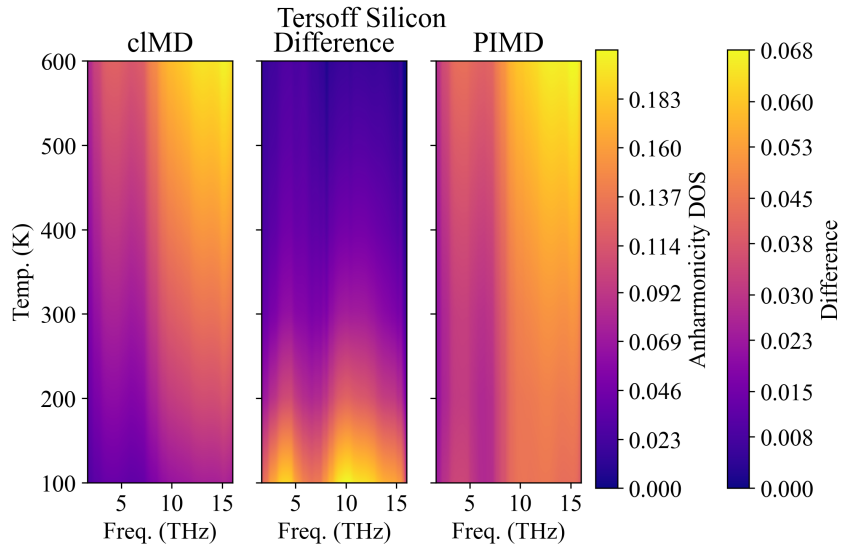


Figure 3.6: The anharmonicity density of states of Tersoff Argon (left classical MD, right PIMD) as well as the difference between both (middle).

anharmonicity, we introduce what we call the "anharmonicity density of states" defined by:

$$\sigma^A(\omega) = \frac{1}{\Omega} \sum_s \int_{\text{BZ}} \sigma_s^A(\mathbf{q}) \delta(\omega_s(\mathbf{q}) - \omega) d\mathbf{q} \quad (3.8)$$

Here Ω is the Brillouin zone volume, ω the phonon frequencies, \mathbf{q} the wave vector, and $\sigma_s^A(\mathbf{q})$ (*vecq*) the mode specific anharmonicity from Eq. 2.179. The anharmonicity density of states $\sigma^A(\omega)$ is directly linked to the overall anharmonicity score σ^A via the integral:

$$\int \sigma^A(\omega) d\omega = \sigma^A. \quad (3.9)$$

The impact of quantum nuclear fluctuations on the anharmonicity DOS is measured by the difference of PIMD and clMD anharmonicity:

$$\sigma_{\text{Diff}}^A(\omega) = \sigma_{\text{PIMD}}^A(\omega) - \sigma_{\text{clMD}}^A(\omega). \quad (3.10)$$

Here $\sigma_{\text{PIMD}}^A(\omega)$ and $\sigma_{\text{clMD}}^A(\omega)$ are the PIMD and clMD anharmonicity density of states respectively. The anharmonicity density of states for Lennard-Jones Argon is shown in Fig. 3.5, the one for Tersoff Silicon in Fig. 3.6. In both materials, QNFs increase the frequency-resolved anharmonicity, but the magnitude and temperature range are quite different. In Lennard-Jones Argon, the increase above 20 K is most pronounced for frequencies below 1.5 THz. However, for lower temperatures, i. e. less than 20 K, the modes between 1.5 and 2 THz begin to contribute meaningfully to the anharmonicity. Conversely, above 40 K we observe that $\sigma_{\text{PIMD}}^A(\omega)$ transitions into the classical limit. In Tersoff Silicon, quantum nuclear fluctuations increase the anharmonicity mostly for

modes above 7 THz and below 5 THz. Accordingly, nearly all modes contribute to the overall anharmonicity increase in σ^A . This remains unchanged at elevated temperatures where $\sigma^A(\omega)$ slowly transitions into the classical limit. However, even at 600 K, quantum nuclear fluctuations visibly increase the anharmonicity. While quantum nuclear fluctuations increase the anharmonicity almost uniformly in Tersoff Silicon, we observed a surprising bias towards lower frequencies in Lennard-Jones Argon. While quantum nuclear fluctuations are normally associated with high vibrational frequencies, zero-point motion displaces the nuclei inverse proportionally to the phonon frequency $\frac{C_{ab}}{2\omega_s^2(\mathbf{q})}$ ³, which explains the behaviour observed in Lennard-Jones Argon. Numerically we see that the classical limit is recovered correctly even if the forces are projected on eigenmodes of the dynamical matrix. However, Tersoff Silicon still exhibits an increased anharmonicity at 600 K which matches the observation from the total anharmonicity. Accordingly, subtracting the frequency-resolved cIMD anharmonicity from its PIMD counterpart is a useful metric to measure the frequency-resolved impact QNFs have.

3.1.4 How does this Relate to the Thermal Conductivity

It has long been known that the presence of quantum nuclear fluctuations and anharmonic effects at the same time, impacts predictions of the thermal conductivity. However, it is seldom discussed what happens if both are also equally important. To shed some light on this issue it is useful to investigate if there is an overlap between the modes which exhibit an increase in anharmonicity and those, which contribute to the thermal conductivity. For that purpose we use the thermal conductivity density of states.

$$\kappa(\omega) = \frac{1}{\Omega} \sum_s \int_{\text{BZ}} \kappa_s(\mathbf{q}) \delta(\omega_s(\mathbf{q}) - \omega) d\mathbf{q} \quad (3.11)$$

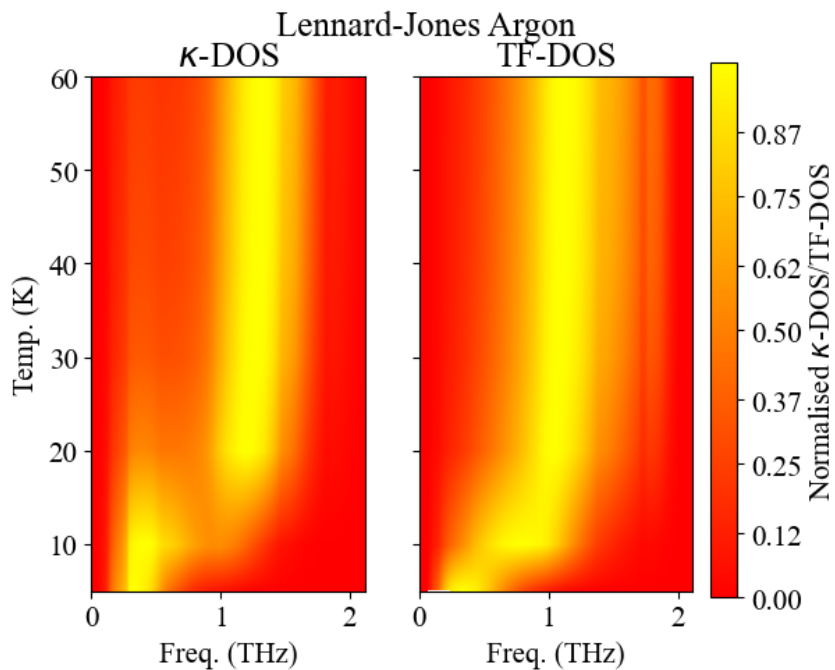
Furthermore, we investigate the single-mode relaxation time approximation in Eq. 2.79. In this approximation, the only anharmonic quantity is the lifetime, while how much heat can potentially be transported is determined by the group velocity and the mode-specific heat, two quantities accessible in the harmonic approximation. The latter contribution is called the transport function and is usually defined without the specific heat capacity. Here we include it, as it is important for comparing classical and quantum nuclear dynamics. Accordingly, the transport function (TF) is defined as:

$$\text{TF}_s^{\text{Cl}}(\mathbf{q}) = \mathbf{v}_s(\mathbf{q}) \otimes \mathbf{v}_s(\mathbf{q}) k_B \quad (3.12)$$

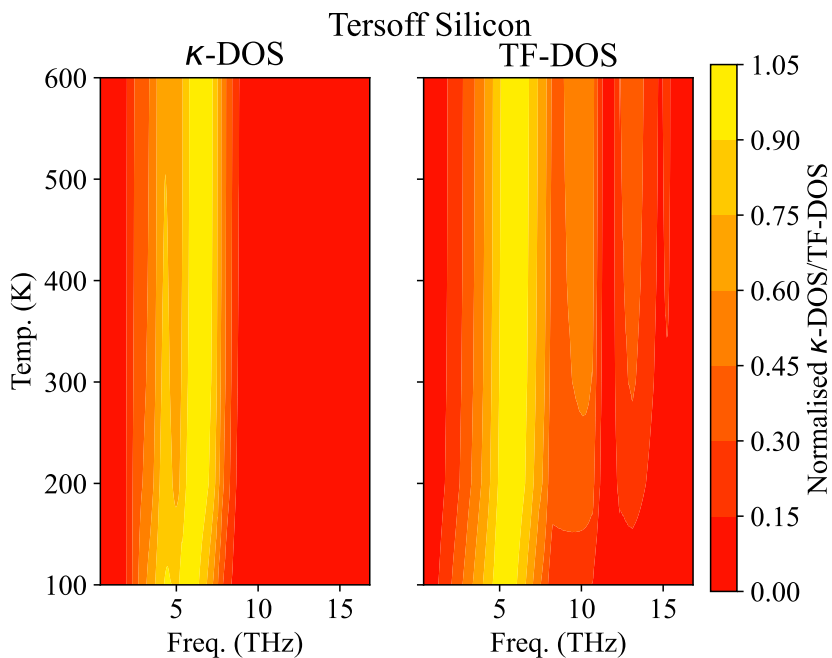
$$\text{TF}_s^{\text{Qm}}(\mathbf{q}) = \mathbf{v}_s(\mathbf{q}) \otimes \mathbf{v}_s(\mathbf{q}) C_s(\mathbf{q}) \quad (3.13)$$

Here \otimes is the tensor product and $C_s(\mathbf{q})$ the mode-specific heat capacity as defined in Sec. 2.2.1. The phonon group velocity is calculated from the phonon band structure

³Here we accounted for the first anharmonic correction as present in a Gram-Charlier expansion.



(a)



(b)

Figure 3.7: Thermal conductivity (left) and transport function (right) density of states as defined in Eq. 3.11 and Eq. 3.15 respectively for Lennard-Jones Argon (a) and Tersoff Silicon (b). The densities were normed using the Uniform norm to allow for comparisons between temperatures.

via:

$$\mathbf{v}_s(\mathbf{q}) = \nabla_{\mathbf{q}}\omega_s(\mathbf{a}) \quad (3.14)$$

It is the speed at which a packet of phonons propagates through a solid. To allow for comparability the "classical" transport function was defined by replacing the mode-specific heat capacity with its classical limit. While we have provided a very general definition of the transport function, only its trace will be used. The corresponding density of states is defined analogue to the thermal conductivity density of states in Eq. 3.11:

$$\text{TF}(\omega) = \frac{1}{\Omega} \sum_s \int_{\text{BZ}} \text{TF}_s(\mathbf{q}) \delta(\omega_s(\mathbf{q}) - \omega) d\mathbf{q}. \quad (3.15)$$

The TF-DOS allows insights into how much heat a mode could potentially carry. The transport function and thermal conductivity for Lennard-Jones Argon and Tersoff Silicon were calculated on an extended $40 \times 40 \times 40$ k-grid. The necessary finite displacements calculations were generated using the phonopy and phono3py packages for the Hessian and the 3rd order force constants respectively. For Argon we chose an $8 \times 8 \times 8$ cubic supercell with 2048 atoms and for Silicone a $6 \times 6 \times 6$ supercell with 1728 atoms. For that purpose, Fig. 3.7 shows a comparison between κ -DOS and TF^{Qm} -DOS. For Lennard-Jones Argon the comparison reveals that both functions contain very similar qualitative information, each revealing that the bulk of the heat is transported by modes below 1 THz for temperatures under 20 K. This is followed by a shift to frequencies above 1 THz for higher temperatures. Since this is present in both functions we know that it is caused by the mode-specific heat capacity. However, the TF^{Qm} -DOS also exhibits additional peaks, especially above 20 K, for frequencies higher than 1.5 THz, which are absent in the κ -DOS. This is due to the $1/\omega_s^2(\mathbf{q})$ [149] scaling of the mode resolved phonon-lifetime $\tau_s(\mathbf{q})$ and thus higher frequency modes typically contribute less to the thermal conductivity. A similar situation can be observed in Tersoff Silicon, both functions show that most of the heat is carried by modes between 5 THz and 10 THz. However, the TF^{Qm} -DOS exhibits additional peaks, above 10 THz, which are again absent in the κ -DOS. While the transport function is calculated from harmonic quantities alone, it can be combined with the frequency-resolved anharmonicity score $\sigma^{\text{A}}(\omega)$. This builds on the approximation

$$\sigma^{\text{A}}(\omega) \sim \frac{1}{\tau(\omega)}, \quad (3.16)$$

which relates the frequency-resolved anharmonicity and the phonon lifetime. A more fundamental observation was made in Ref. [112] which, reveals an inverse proportional relationship between the thermal conductivity and overall anharmonicity $\sigma^{\text{A}}(T) \sim \frac{1}{\kappa(T)}$.

To illustrate this behavior, we follow the spirit of the single mode relaxation time

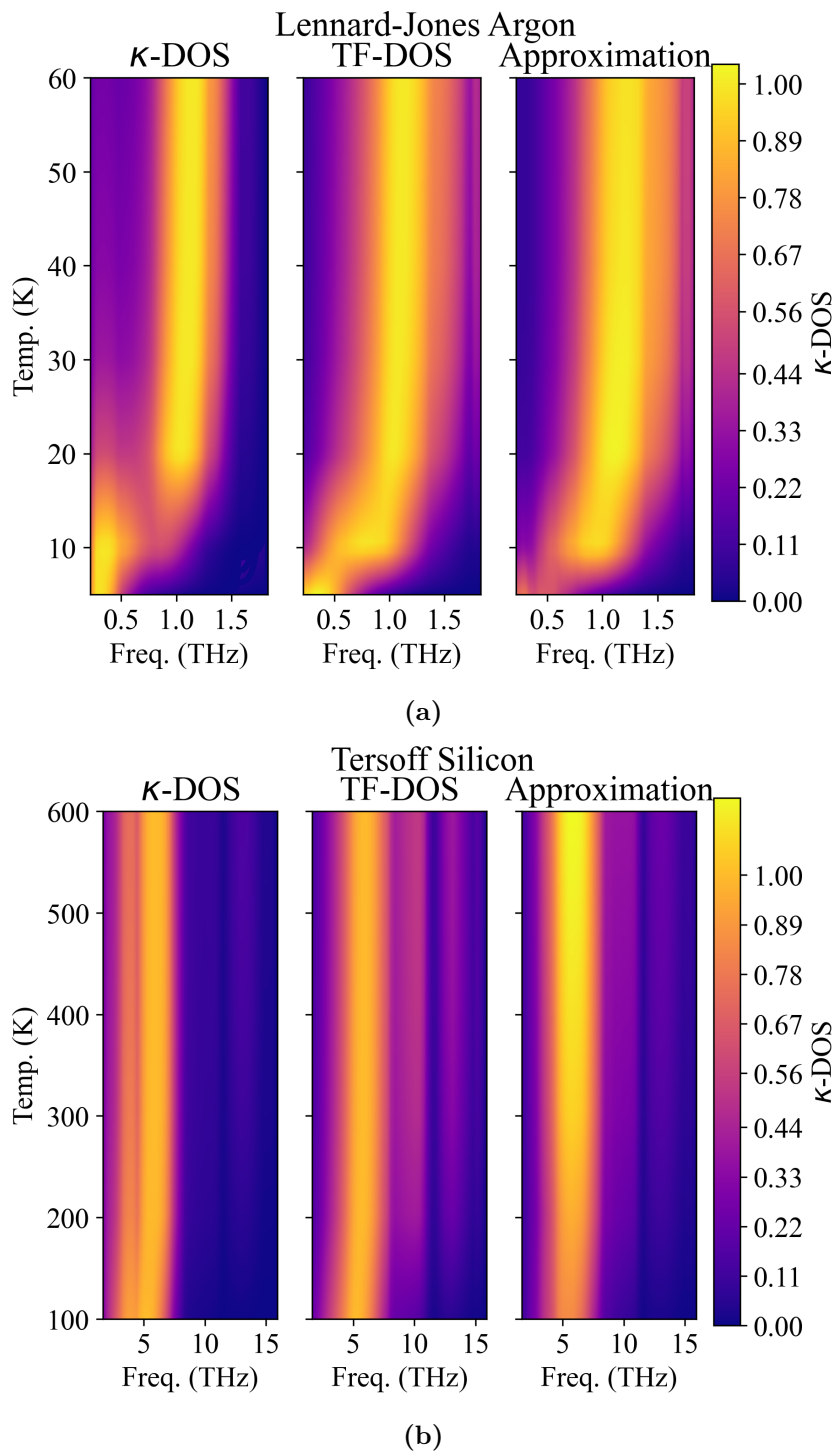


Figure 3.8: The thermal conductivity (left), transport function (middle), and reconstructed density of states based on the definition in Eq. 3.12 for Lennard-Jones Argon (a) and Tersoff Silicon (b) respectively. The densities were normed using the Uniform norm to allow for comparisons between temperatures.

approximation and introduce $\frac{1}{\sigma_{\text{PIMD}}^{\text{A}}(\omega)}$ as a weight for $\text{TF}^{\text{Qm}}(\omega)$:

$$\kappa^{\text{APP}}(\omega) \approx \frac{\text{TF}^{\text{Qm}}(\omega)}{\sigma_{\text{PIMD}}^{\text{A}}(\omega)}. \quad (3.17)$$

In his Fig. 3.8 this approximation is compared to $\kappa(\omega)$ and $\text{TF}^{\text{Qm}}(\omega)$. For Lennard-Jones Argon we observe a separation of the peaks at 0.5 THz between 5 and 20 K in $\kappa(\omega)$, which is not visible in $\text{TF}^{\text{Qm}}(\omega)$. However, due to the inclusion of $\sigma_{\text{PIMD}}^{\text{A}}(\omega)$ it is reproduced by $\kappa^{\text{APP}}(\omega)$. In Tersoff Silicon the inclusion of $\sigma_{\text{PIMD}}^{\text{A}}(\omega)$ observe a pronounced dampening of the erroneous peaks, visible in $\text{TF}^{\text{Qm}}(\omega)$ above 7 THz, are dampened in $\kappa^{\text{APP}}(\omega)$. Accordingly, we can make qualitative statements with sufficient accuracy, even without κ -DOS, by augmenting TF^{Qm} -DOS with $\sigma(\omega)$. Fig. 3.9 illustrated how the inclusion of the mode-specific heat changes the transport function density of states. Since the classical transport function density of states is determined from the harmonic phonon group velocities alone, it does not exhibit any temperature dependence. Thus this is also mirrored in the results for Lennard-Jones Argon, where the TF-DOS peaks at 1.1 THz. Since the classical TF-Dos is the squared group velocity, it is directly linked to the curvature exhibited by $\omega_s(\mathbf{q})$ and peaks where the curvature maximizes. However, we can also see smaller secondary peaks below 1 THz and above 1.3 THz. Conversely, the quantum TF-Dos is weighted by the mode resolved heat capacity and thus is temperature-dependent. Below 10 K we see that the TF-Dos peak below 0.5 THz, at 10 THz we see that the peak switches to 1.1 THz. Since exclusively occupied modes contribute to the heat capacity only low-frequency modes can add to the transport function at low temperatures. The secondary peaks become only visible above 20 K when the heat capacity begins to converge to its classical value $C_s(\mathbf{q}) = k_{\text{B}}$. Above 40 K the TF-Dos finally transitions to its classical limit, i.e. to the classical TF-Dos and the mode-specific heat capacity becomes constants. Similar behavior can be observed in Tersoff Silicon, where the classical TF-Dos assumes its maximum at 6 THz with secondary peaks above 7 THz. However, the quantum TF-Dos shows only a minor shift from 5 THz at 100 K to 5.5 THz at 200 K. The secondary peaks, however, are fully suppressed at 100 K and appear fully above 300 K. The peaks indicate the potentially heat-carrying and as such, is still massively important in Tersoff silicon. The quantum TF-Dos reveals that higher frequency modes only carry significant amounts of heat above 300 K. The inclusion of the mode-specific heat capacity clearly has a pronounced impact which partially explains why at higher temperatures the bulk of the heat is transported by higher frequency modes compared to lower temperatures.

A comparison of the quantum TF-Dos or κ -Dos with $\sigma_{\text{Diff}}^{\text{A}}(\omega)$ allows us to investigate how much QNFs can influence thermal conductivity. An example of this is shown in Fig. 3.10. Demonstrating that in both test systems, QNFs increase the anharmonicity mostly at the frequencies which carry the bulk of the heat. It is especially pronounced Lennard-Jones Argon below 20 K where QNFs are most active. We see that the peaks of the κ -Dos align close to the peaks of $\sigma_{\text{Diff}}^{\text{A}}(\omega)$. Since the peaks in the quantum TF-Dos are at the

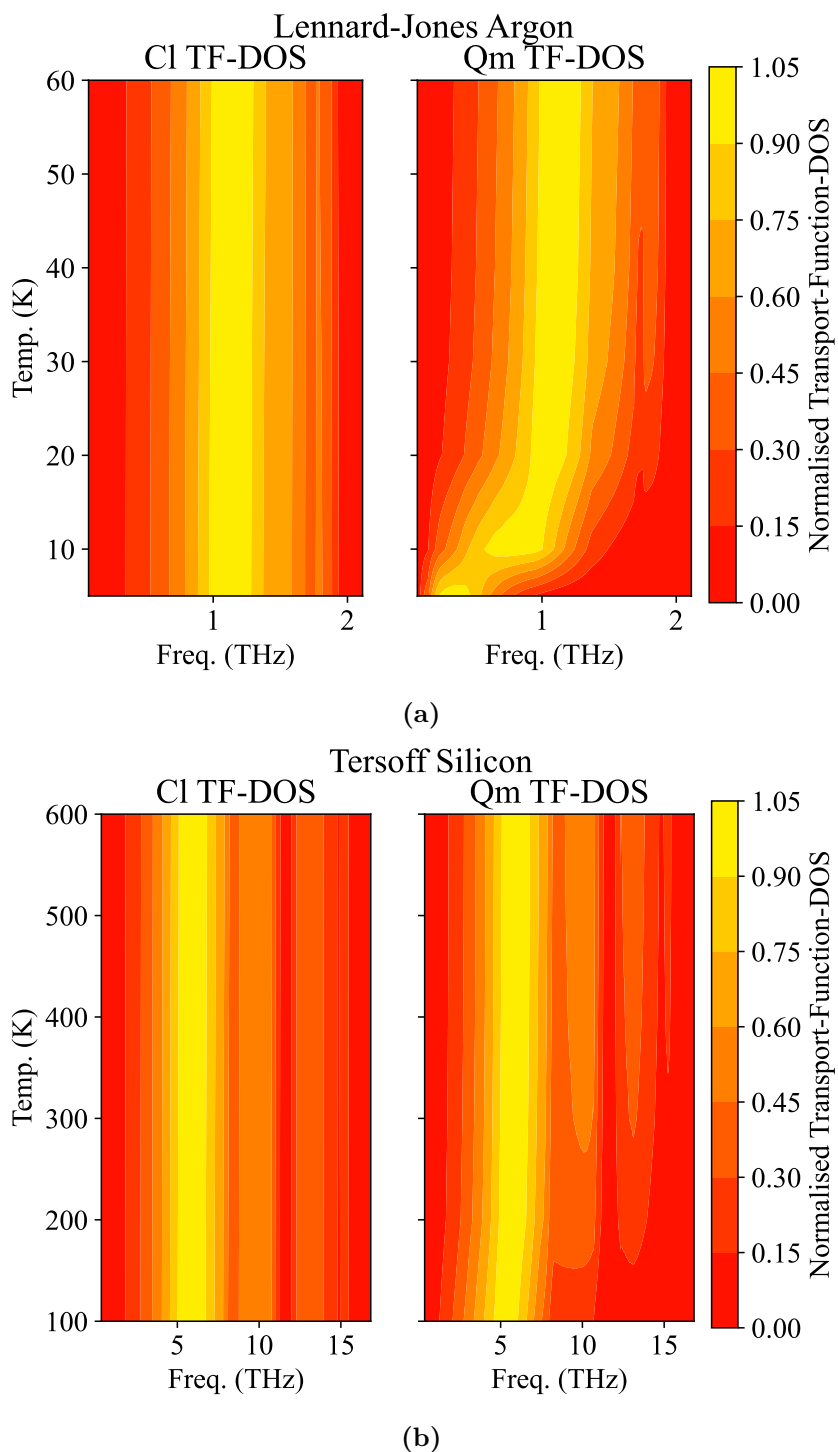


Figure 3.9: The Classical (left) and quantum (right) transport function density of states based on the definition in Eq. 3.12 for Lennard-Jones Argon (a) and Tersoff Silicon (b) respectively. The densities were normed using the Uniform norm to allow for comparisons between temperatures.

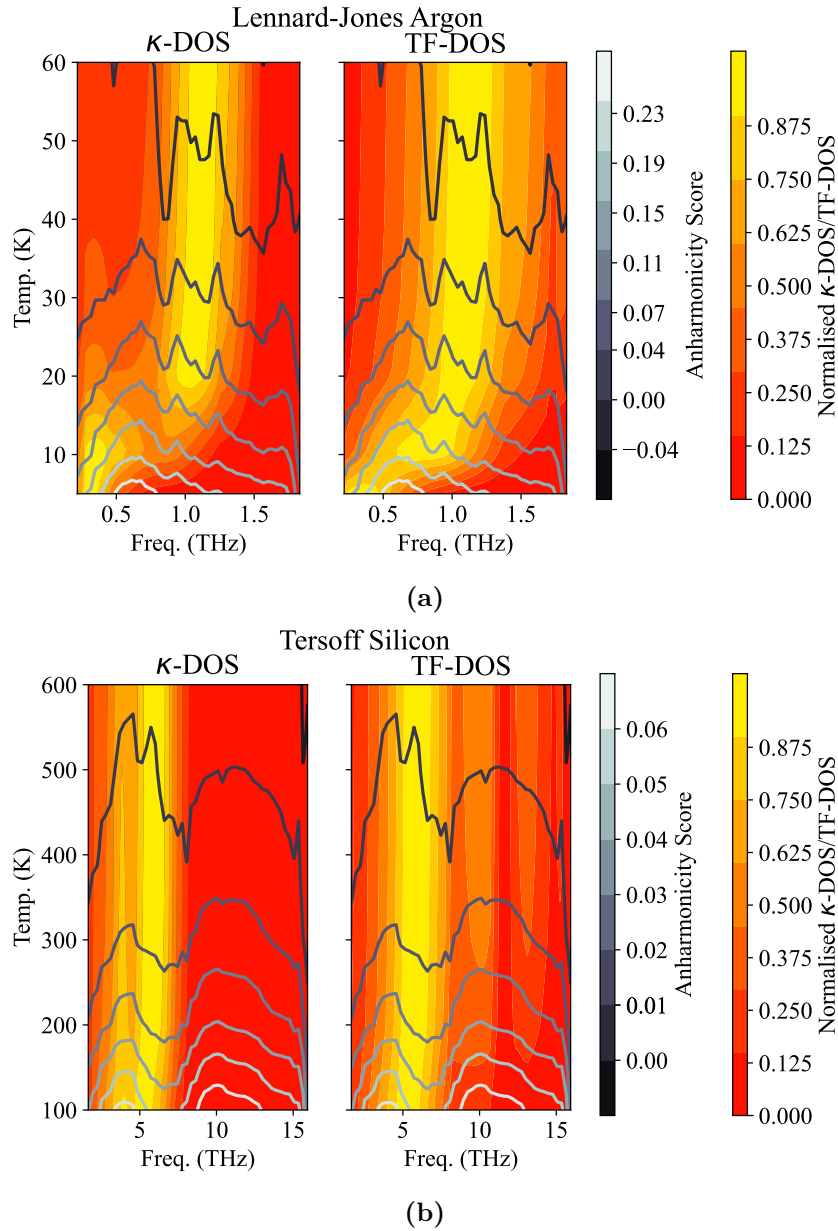


Figure 3.10: The normalized κ -DOS (left) and TF-DOS (right), both no overlaid with the difference between the anharmonicity score 3.10 from cl and PIMD for Lennard-Jones Argon (a) and Tersoff Silicon (b).

same positions a comparison with $\sigma_{\text{Diff}}^{\text{A}}(\omega)$ leads to the same conclusion. In Tersoff Silicon we again see that the highest peaks in the κ -Dos align with the highest peak of $\sigma_{\text{Diff}}^{\text{A}}(\omega)$. However $\sigma_{\omega}^{\text{A}}$ also exhibits peaks at higher frequencies which do not meaningfully contribute to the thermal conductivity. The high-frequency peaks we observed in the TF-Dos align with those of $\sigma_{\text{Diff}}^{\text{A}}(\omega)$ and cause a dampening which is seen in our approximate κ -Dos in Fig. 3.8.

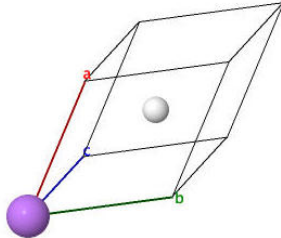
Here we have seen that the TF^{Qm}-DOS together with the anharmonicity difference $\sigma_{\text{Diff}}^{\text{A}}(\omega)$ yields deep insights into the thermal conductivity. In Lennard-Jones Argon, quantum nuclear fluctuations cause a shift in the heat-carrying modes, which is also mirrored in the TF-Dos and also where $\sigma_{\text{Diff}}^{\text{A}}(\omega)$ assumes its highest values. Real Materials Tersoff Silicon and Lennard-Jones Argon can only be considered toy models, which yields the question of how the anharmonicity of real materials is influenced by QNFs. To this end we investigated two industry-relevant examples, namely Lithium Hydride and thin-film Pentacene, using the *ab initio* MD and *ab initio* PIMD implementation of the I-PI [142] (PI)MD code to evaluate the equations of motion based on the *ab initio* forces provided by FHI-aims [100]. To understand the impact quantum nuclear fluctuations have on the degree of anharmonicity of both materials we will employ the approach detailed in chapter 3.

3.1.5 Lithium Hydrate

The first real material investigated closely in this study is Lithium Hydrate. Originally, Lithium Hydrate (LiH) came into the focus of researchers for its applications in nuclear physics. For instance, Lithium Hydride and Lithium Deuteride were and sadly to this day still are used as fuel to create an uncontrolled fusion reaction [134]. Additionally, its high hydrogen content relative to its weight makes Lithium Hydrate well suited for example as a shielding material for nuclear reactors, the demand for which remains strong. Ironically the same qualities make Lithium Hydride a potential candidate for a hydrogen storage medium [134] and also of interest to the author of this thesis. Due to both, Lithium and Hydrogen, being light elements it is to be expected that Lithium Hydride will display high vibrational frequencies and thus strong QNFs.

Basic properties of Lithium Hydride

In the first step, we established the basic geometric properties of Lithium Hydride, i.e. the static equilibrium lattice constant a_0 , the bulk modulus B_0 , as well as their values when zero-point energy effects are accounted for. The lattice constant was calculated using symmetry constrained relaxation as implemented in FHI-Vibes [112] while the bulk modulus was extracted by fitting the total energy at 5 different lattice constants, $\pm 3\%$ around a_0 , to the Birch-Murnaghan [113, 114] equation of state for the pw-LDA [28],



Functional	a_0 (Å)	a_0^{ZPE} (Å)	B_0 (eV/Å ³)	B_0^{ZPE} (eV/Å ³)
pw-LDA	3.94	4.01	0.26	0.22
PBE	4.02	4.12	0.22	0.21
PBEsol	4.00	4.10	0.23	0.21
PBE0	4.02	4.10	0.22	0.21
HSE06	4.03	4.11	0.22	0.21
Exp.	4.07 ^a 4.08 ^b		0.20 ^c	

Figure 3.11 & Table 3.1: Left: The Primitive unit cell of pristine lithium hydride (Li purple, H white). Right: The static equilibrium lattice constant a_0 and bulk modulus B_0 as well as the renormalized lattice constant a_0^{ZPE} , and bulk modulus B_0^{ZPE} computed for different XC functionals.
^a Ref. [146] ^b Ref. [145] ^c Ref. [148]

E_{gap} (eV)	this work						from literature	
	LDA	PBE	PBEsol	PBE0	PBEsol0	HSE06	Exp. [135, 136]	PBE [137]
$L \leftrightarrow L$	7.64	7.42	7.40	9.28	9.27	8.51	9.0	–
$X \leftrightarrow X$	2.57	3.00	2.75	4.66	4.49	4.05	4.99	3.19

Table 3.2: Values for the direct ($L \leftrightarrow L$) and ($X \leftrightarrow X$) Electronic bandgaps of LiH calculated with pw-LDA, PBE, PBEsol, PBE0, PBEsol0, and HSE06.

PBE [29], PBEsol [30], PBE0 [32], and HSE06 [34] XC-functionals. Both zero-point energy renormalized values a_0^{ZPE} and B_0^{ZPE} were calculated in the quasi-harmonic approximation again for pw-LDA, PBE, PBEsol, PBE0, and HSE06. The results together with the primitive unit cell are shown in Fig. 3.11. The static equilibrium properties suggest that pw-LDA underestimates the lattice constant while the bulk modulus is overestimated in line with LDAs' "overbinding" tendency. Conversely, PBE "underbinds" and thus presents the opposite trend, while PBEsol occupies a middle ground between LDA and PBE. Comparing a_0 and B_0 to the more expensive but also more accurate PBE0 and HSE06 hybrid functionals reveals that, PBE yields the results closest with respect to PBE0 and HSE06 calculations. With respect to experiments, which naturally include quantum nuclear fluctuations, we have to include QNFs to draw the most accurate conclusion. While the renormalization has a minimal impact on the bulk modulus it significantly increases the lattice constant for all functionals. Comparing the values for a_0^{ZPE} and B_0^{ZPE} from pw-LDA, PBE, and PBEsol to experiments and both hybrid functionals reveals the expected "overbinding" and "underbinding" tendencies of pw-LDA and PBE respectively while PBEsol serves as a middle ground and produces the results closest to the values obtained from experiments as well as PBE0 and HSE06. This demonstrates the importance of the inclusion of QNFs for accurate geometric properties. Fig. 3.12 shows the electronic band structure of lithium hydride for pw-LDA, PBE, and PBEsol in comparison with PBE0, PBEsol0 [33], and HSE06. While all band structures look qualitatively similar it is obvious that the band gap for pw-LDA, PBE, and PBEsol is much smaller than the band gaps

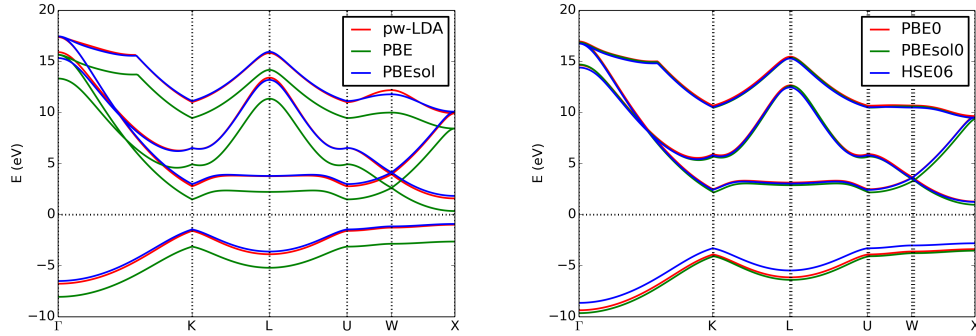


Figure 3.12: Electronic band structure of LiH close to the Fermi level as computed with DFT between high-symmetry points $[100]$ at the respective equilibrium geometries (see Tab. 3.1) for the LDA, PBE, PBEsol (all left), and for the PBE0, PBEsol0, and HSE06 XC-functional (right).

predicted by PBE0, HSE06, and PBEsol0 (see Tab. 3.2). A more detailed investigation of the electronic structure in terms of a *partial* density of states (PDOS)⁴ reveals at least partially ionic character of the bond between lithium and hydrogen as shown in Fig. 3.13.

Vibrational Properties of Lithium Hydride

Since this thesis is mainly focused on the influence quantum nuclear fluctuations exert on the degree of anharmonicity and the thermal conductivity, the choice of which XC-functional to use cannot be made from the geometric and electronic properties alone. Accordingly, we do not only investigate the phonon spectrum for PBEsol, but also pw-LDA, PBE, PBE0, and HSE06. The results are shown in Fig. 3.14 confirming that lithium hydride indeed exhibits high vibrational frequencies. A direct comparison to experiments is complicated since phonon band structure measurements are preferably conducted on lithium deuteride due to its larger neutron scattering cross-section [138] which exhibits drastically lower frequencies in the optical modes due to the higher mass of the Deuterium. However, it has been demonstrated that the acoustic modes barely change [139] which is confirmed by our calculation which is in good agreement with the experiment for all modes and also consistent with the results for Lithium Hydride. By extension, this also demonstrates that pw-LDA, PBEsol, and PBE band structures agree with the experimental results. Furthermore, there are only minimal differences between PBE and PBEsol in the optical modes, only pw-LDA introduces oscillations in the optical modes near the Γ -point. Importantly, we observe a splitting of the longitudinal and transversal optical modes near the Γ -point. This is due to the ionic nature of the bonds between Lithium and Hydrogen or Deuterium. Comparing the PBE0 and HSE06 phonon band structures shows

⁴In *partial* density of states the contribution of the individual atoms to the full density of states is disentangled by performing a Mulliken population analysis, i.e., by projecting it onto individual atomic orbitals.

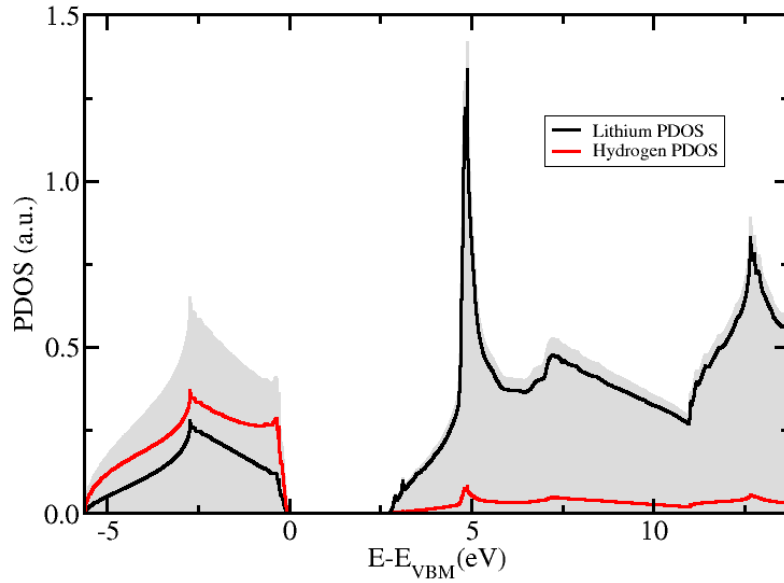


Figure 3.13: Species projected electronic density of states of LiH calculated using the PBEsol XC-functional and tetrahedron method. The total DOS is shaded gray.

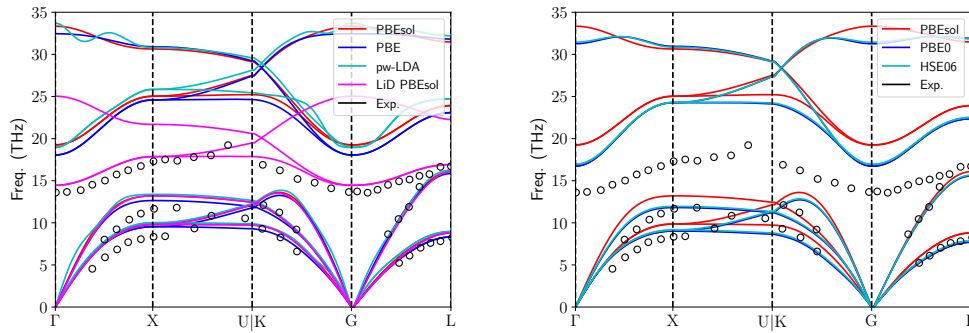


Figure 3.14: Phonon band structure of lithium hydride, the left image shows calculations with pw-LDA (cyan), PBE (blue), and PBEsol (red) as well as lithium deuteride (magenta, PBEsol only) compared neutron scattering experiments for lithium deuteride taken from Ref. [138]. The right image shows results using PBE0 (blue), HSE06 (cyan), and PBEsol (red) for reference.

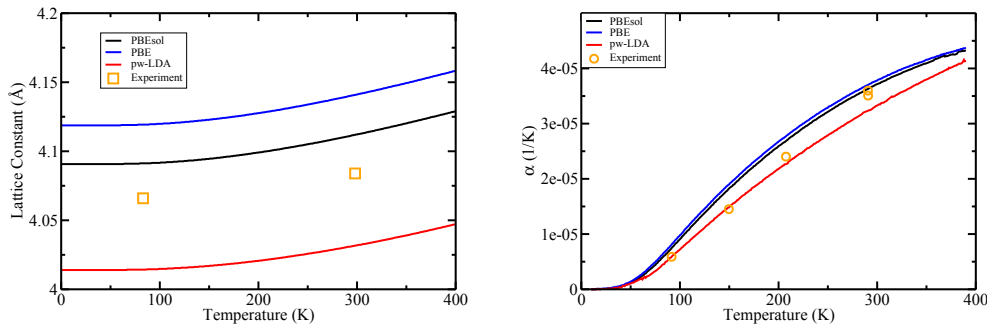
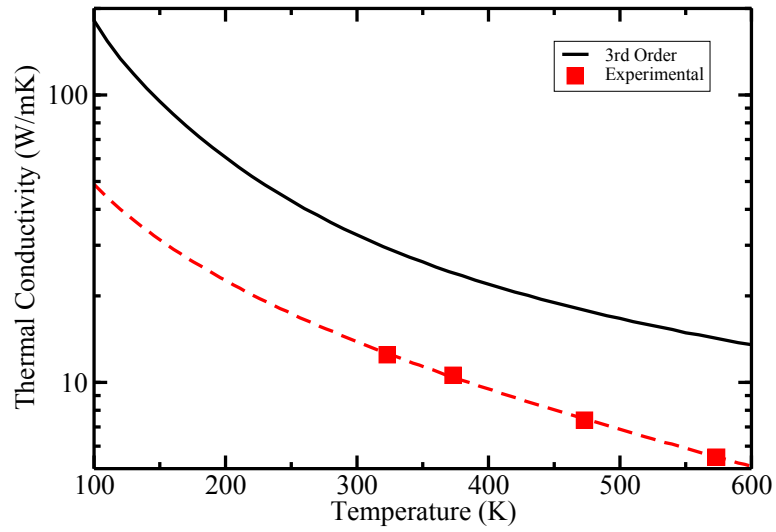


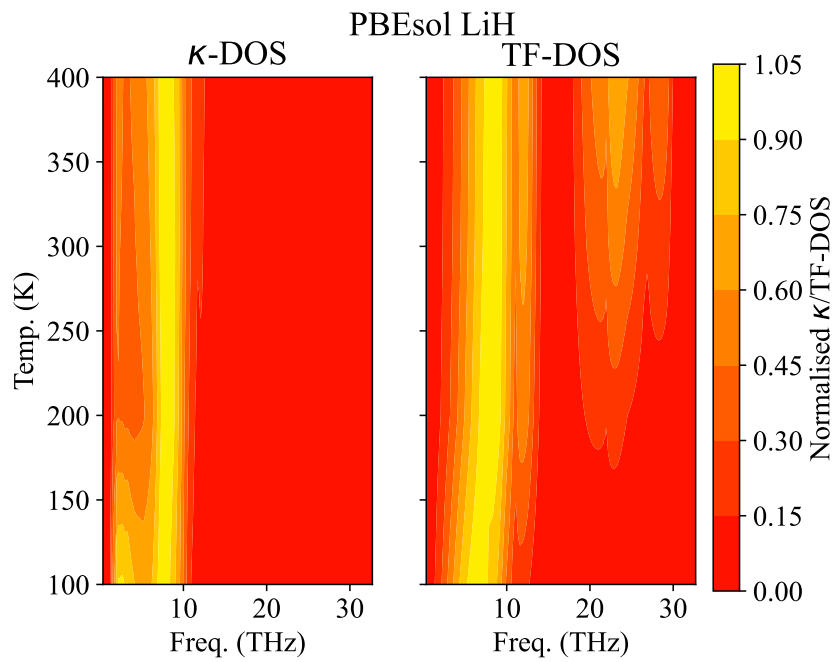
Figure 3.15: Lattice constant (left) and thermal expansion coefficient (right) for Lithium Hydride calculated using the quasi-harmonic approximation (black line PBEsol, blue line PBE, and red line pw-LDA) as well as experimental results (orange squares and circles). The experimental data for the temperature-dependent lattice constants were obtained by X-ray diffraction [146], the experimental expansion coefficients were measured using dilatometric methods [145].

that both hybrid functionals produce almost identical results with negligible quantitative differences. Conversely, the difference between all (semi-)local XC-functionals and both hybrid functionals is more pronounced. Especially at the Γ -point pw-LDA, PBE, and PBEsol all predict 2 (PBE) to 4 (pw-LDA and PBEsol) THz higher frequencies. As previously discussed high frequency phonons often indicate active quantum nuclear fluctuations which is demonstrated in Fig. 3.14. It also illustrates the influence of the XC-functional on the phonon band structure. Fig. 3.15 shows the temperature-dependent lattice constants and thermal expansion in quasi-harmonic approximation calculated for pw-LDA, PBE, and PBEsol. Both pw-LDA and PBEsol show similar quantitative results, however, PBEsol more closely replicates the qualitative properties of the experimental thermal expansion coefficient.

Fig. 3.16 also demonstrates that a perturbative approach overestimates the thermal conductivity by up to 300 percent compared to experimental results. However, the qualitative trend is reproduced correctly, suggesting that its density of states still offers qualitative insights into which modes carry the bulk of the heat. Investigating the κ -DOS suggests that heat is mostly transported by low-frequency modes (around 10 THz) which are also apparent from the transport function DOS. However, at higher temperatures, the TF-DOS exhibits peaks between 20 and 30 THz which are not visible in the κ -DOS. This is due to the mode-specific heat capacity slowly converging to its classical value of k_B which is compensated for in κ -DOS since mode dependence of the relaxation time approximately obeys the relation $\tau(\omega) \propto \frac{1}{\sigma^A(\omega)}$ [112].



(a)



(b)

Figure 3.16: The thermal conductivity of Lithium Hydrate (a) obtained from third-order perturbation theory (solid line) in the single-mode relaxation time approximation and experiments [147] (red squares) and the κ and TF-DOS respectively (b). The experimental data was obtained by measuring the heat flow from the inside to the outside of a series of stacked annular rings.

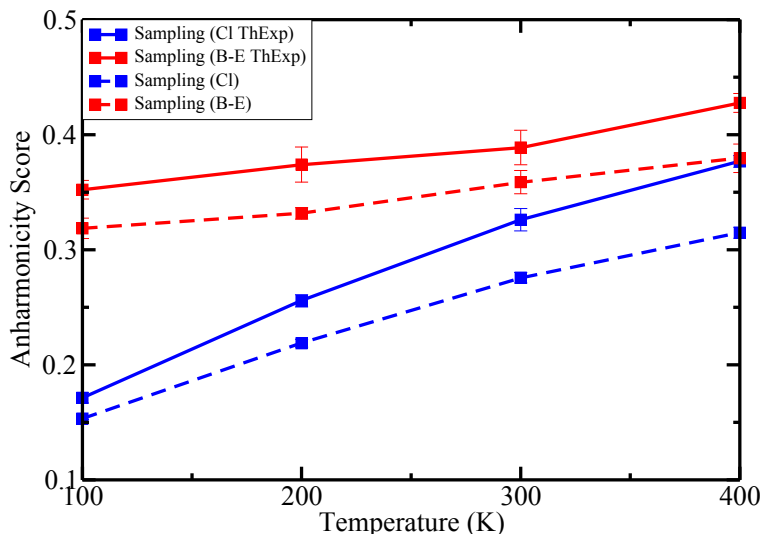


Figure 3.17: Anharmonicity scores of Lithium Hydrate from 100 (K) to 400 (K), using classical harmonic sampling (blue line) and quantum harmonic sampling (red), without (dashed lines) and including (solid lines) thermal expansion.

3.1.6 The Anharmonicity of Lithium Hydride

As demonstrated in the previous section lithium hydride not only exhibits strong quantum nuclear fluctuations but also high thermal expansion. Based on the results shown in the previous section we chose the PBEsol XC-functional [30] to analyze the anharmonicity of lithium hydride using the quasi-harmonic approximation to account for thermal expansion. Furthermore as demonstrated in Sec. 3.1.3 we can safely assume that the inclusion of QNFs in the thermal expansion does not influence the results of classical sampling methods as long as the lattice constants are consistent with the harmonic force constants. Due to the high vibrational frequencies, the time steps for all ai and PIMD simulations were set to 1 fs, for all aiMD trajectories we again chose the SVR thermostat [61]. To thermalize the internal PIMD ring polymer modes and the centroid mode as efficiently as possible, we chose the PILE-g [167] thermostat (see Appendix for a more in-depth explanation). Finally, we run multiple trajectories at 300 K to converge the simulation concerning the number of replicas. By extrapolating we found the necessary number of replicas for each temperature to be 24@100 K, 12@200K, 8@300K, and 6@400K. The anharmonicity score extracted from classical and quantum harmonic sampling is shown in Fig. 3.17 with and without thermal expansion. Starting with the static lattice we find that σ_{clHA}^A again demonstrates a $\propto \sqrt{T}$ temperature dependence. At 400 K we find that LiH exhibits an anharmonicity of $\sigma^A = 0.32$ and intermediate anharmonicity between 0.15-0.25. Finally, accounting for thermal expansion increases the anharmonicity by 0.02 at 200 K up to 0.06 at 400 K. Conversely, quantum harmonic sampling reveals that Lithium Hydride is strongly

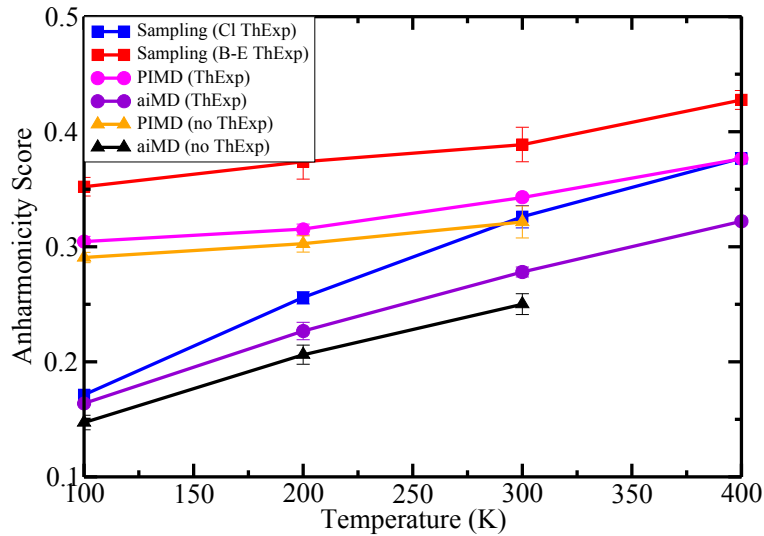


Figure 3.18: This figure shows the anharmonicity scores of Lithium Hydrate from 100 (K) to 400 (K) using different methods. The left image compares the anharmonicity score obtained from harmonic sampling with (solid line) and without (dashed line) thermal expansion.

anharmonic at all temperatures. At 0 K we observe that zero-point motion increases the anharmonicity to $\sigma_{\text{qmHA}}^A \sim 0.35$. Similar to the previously discussed toy systems, we observe a larger anharmonicity increase at low temperatures compared to high temperatures. However, even at 400 K impact remains sizable since σ_{qmHA}^A exhibits almost no temperature dependence. Accordingly, the anharmonicity increase from thermal expansion is also approximately temperature independent. Calculating the anharmonicity along different aiMD trajectories, reveals that while at 100 K $\sigma_{\text{aiMD}}^A(T = 100) \approx \sigma_{\text{clHA}}^A(T = 100)$, harmonic sampling overestimates the anharmonicity for all higher temperatures classical (Fig. 3.18). The inclusion of thermal expansion slightly again increases the anharmonicity. PIMD shows a qualitative identical anharmonicity increase compared to aiMD as we have seen in the comparison between quantum and classical harmonic sampling. However, compared to PIMD, quantum harmonic sampling overestimates the anharmonicity for all temperatures by 0.05. This is also visible in the $T \rightarrow 0\text{K}$ anharmonicity which is 0.3 in PIMD. However, since the qualitative trends are unchanged, the anharmonicity increase due to thermal expansion remains almost temperature independent in PIMD.

The anharmonicity density of states, in Fig. 3.19, demonstrates that QNFs uniformly increase the anharmonicity for modes up to 22 THz. Importantly $\sigma_{\text{Diff}}^A(\omega)$ remains uniformly distributed and pronounced at elevated temperatures. Fig. 3.20 shows the thermal conductivity and transport function densities together with $\sigma_{\text{Diff}}^A(\omega)$ taken from Fig ???. It shows that most of the heat is transported by modes at low frequencies, i.e. below 10 THz. This agrees with the peak exhibited by $\sigma_{\text{Diff}}^A(\omega)$. Above 200 K the TF-Dos exhibits

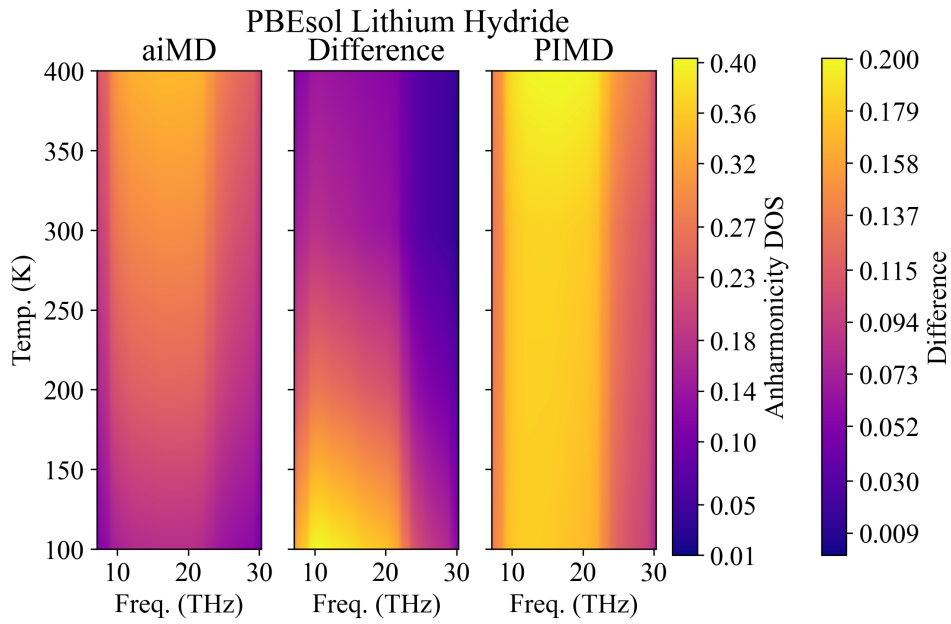


Figure 3.19: This figure shows the mode resolved anharmonicity score, accounting for thermal expansion, extracted from aiMD (left), PIMD (right), and their difference (middle). All images are color-coded identically to allow for comparisons.

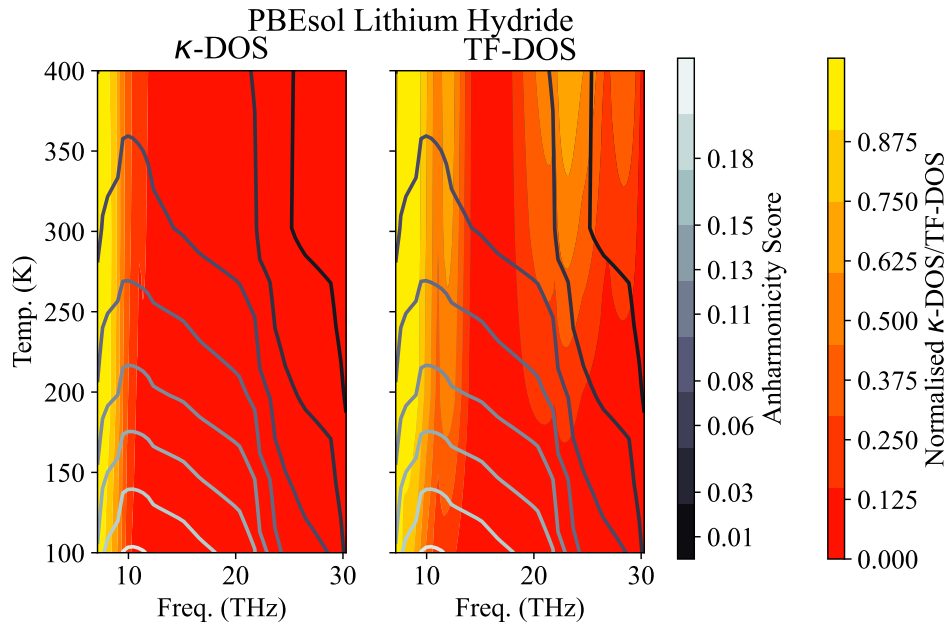


Figure 3.20: κ -DOS (left) and TF-DOS (right) overlaid with the difference between the PIMD and aiMD anharmonicity density of states $\sigma_{\text{Diff}}^{\text{A}}(\omega) = \sigma_{\text{PIMD}}^{\text{A}}(\omega) - \sigma_{\text{aiMD}}^{\text{A}}(\omega)$.

additional peaks between 20 and 30 THz, which are dampened in the thermal conductivity Dos.

Results LiH

In Lithium Hydride, quantum nuclear fluctuations increase the anharmonicity for all investigated. While classical harmonic sampling exhibits the same anharmonicity as aiMD at 200, quantum harmonic sampling overestimates the anharmonicity at every temperature compared to PIMD. Thus Lithium Hydride is highly anharmonic when quantum nuclear fluctuations are included. However, since, $\sigma_{\text{qmHA/PIMD}}^{\text{A}}(T) \sim \text{const}$ we conclude that zero-point motion largely dominates the nuclear motion, even at 400 K. Accordingly, the frequency-resolved anharmonicity shows that QNFs increase the anharmonicity predominantly below 20 THz. Comparing $\sigma_{\text{Diff}}^{\text{A}}(\omega)$ to the thermal conductivity Dos shows that the QNFs likely have a pronounced impact on heat transport. Since the anharmonicity is not sufficiently captured by quantum harmonic sampling, a perturbative approach to the thermal conductivity is not sufficient. This is supported by the observation that the thermal conductivity is overestimated if only the leading anharmonic order is considered (see Fig. 3.16b).

3.1.7 Thin Film Pentacene

The second material we investigate is thin-film pentacene. Its most ubiquitous application is probably in the form of thin-film transistors [150], which are essential in today's electronic industry, where they are used for example to drive OLED displays [151], including the only recently released flexible OLEDs [152]. Pentacene is also of massive academic relevance and is for example used to realize masers [153, 154] which can operate at ambient conditions, potentially paving the way to life-saving applications in medicine by increasing the precision of magnetic resonance spectrometers [155]. Both applications are sure to generate heat, which has to be transported away, which combined with its high vibrational frequencies attracted our attention.

Basic Properties of Thin-Film Pentacene

All materials discussed up to this point (argon, silicon, and lithium hydride) exhibited a cubic lattice structure with high degrees of symmetry and most importantly had atoms as their "building block". Conversely, thin-film pentacene is a molecular crystal, with pentacene chains ($\text{C}_{22}\text{H}_{14}$) as its building blocks. While the carbon and hydrogen atoms enter covalent bonds the different chains are only held together by van der Waals forces [156]. Similar to most molecular crystals thin-film pentacene exhibits only minimal symmetries, exhibiting a triclinic lattice structure. Difficulties arise from the unique properties of thin-film materials, which are three-dimensional systems with a small finite thickness.

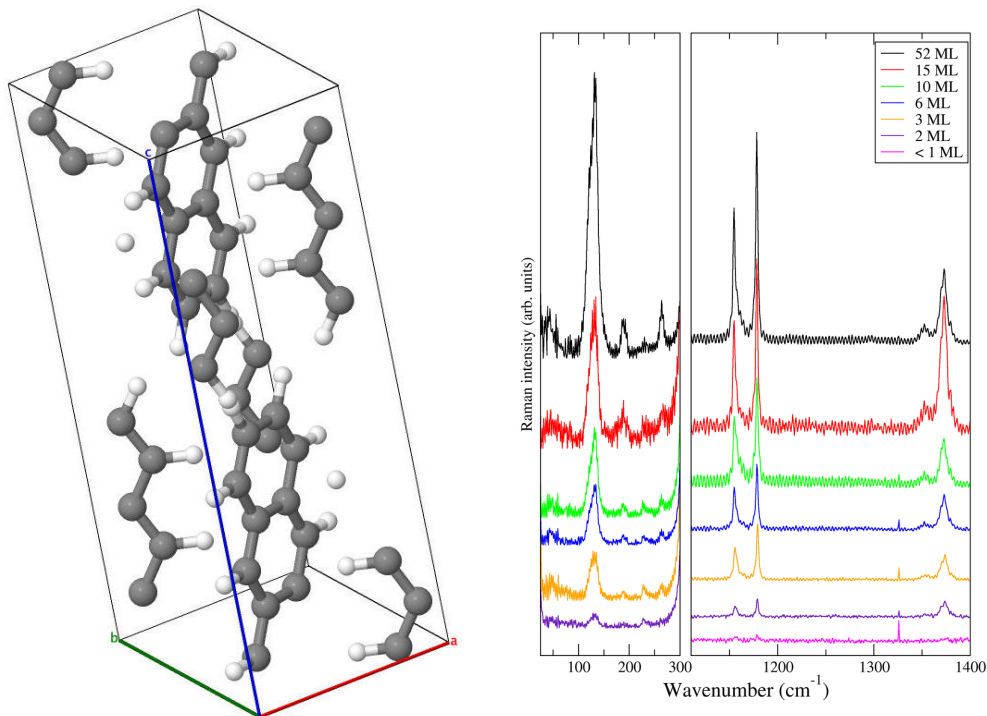


Figure 3.21: Relaxed thin film pentacene unitcell (left) and Raman spectra as a function of films thickness measured in mono layers (ML) taken from Ref [157]

Temp. (K)	Lattice Parameters (\AA)			Angles		
	a	b	c	α	β	γ
200	5.92	7.55	15.59	81.07	86.44	89.78
300	5.93	7.56	15.66	81.07	86.44	89.78
400	5.94	7.60	15.72	80.95	86.40	89.81

Table 3.3: Lattice parameters used for aiMD, PIMD, and second-order force constants. a, b, and c denote the lattice constants and α , β , and γ the angles between them.

Fig. 3.21 illustrates how the intensity of the peaks in Raman spectra are influenced by the film's thickness, measured in monolayers ($1 - 2 \text{ ML} \sim 23 \text{ \AA}$), clearly, the bulk limit is not reached in such samples. Many theoretical studies avoid this problem by using experimentally determined lattice parameters [159, 160, 161]. We used the same approach and extract the lattice parameters from x-ray diffraction experiments on 500 \AA thick thin-film Pentacene presented in Ref. [163]. However as shown in Fig. 3.22 experiments do not yield smooth curves, accordingly, we averaged over the measured values close to 300 K and 400 K respectively to obtain reliable results. To extend the temperature range we assumed that the thermal expansion varies only minimally between 200 K and 300 K. This is supported by the thermal expansion coefficient we calculated from the running averages of the lattice parameters. Accordingly, we obtained a linear fit from the measured values around 300 K and used this to extrapolate down to 200 K. The atomic positions were subsequently relaxed using the PBE XC-functional including van der Waals interaction via

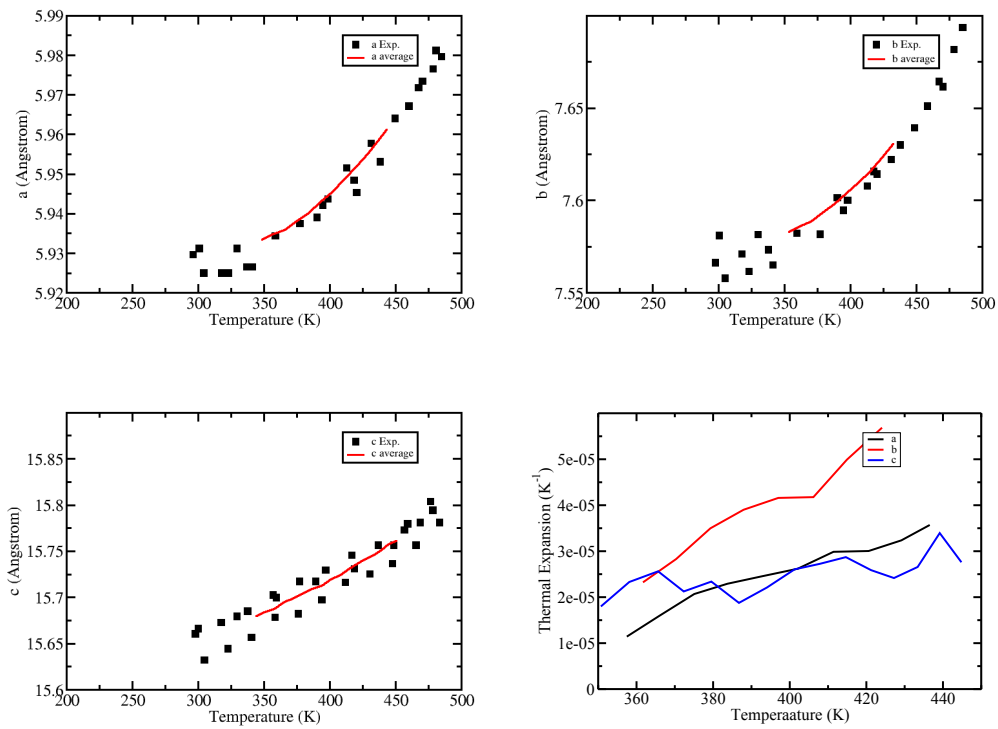


Figure 3.22: Experimental lattice constants of thin film pentacene measured using grazing incidence x-ray diffraction taken from Ref. [163]. The thermal expansion (bottom right) was calculated using the running average of the different lattice constants (red curves).

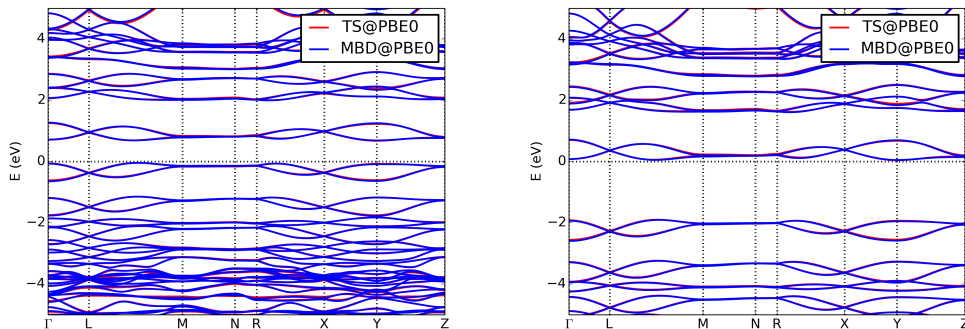


Figure 3.23: Electronic band structures of thin-film pentacene close to the Fermi level as computed with DFT for the PBE (left) and PBE0 (right) comparing the TS and many body dispersion correction schemes.

E_{gap} (eV)	this work				from literature
	TS@PBE	MBD@PBE	TS@PBE0	MBD@PBE0	Exp [137]
Smallest Gap	0.72	0.73	1.95	1.95	1.8

Table 3.4: Values for the direct ($L \leftrightarrow L$) and ($X \leftrightarrow X$) Electronic bandgaps of LiH calculated with pw-LDA, PBE, PBEsol, PBE0, PBEsol0, and HSE06.

many-body dispersion [103, 104] and the pairwise TS-method [102]. The band structures in Fig. 3.23 were calculated using the extrapolated 200 K structure. While PBE and PBE0 band structures are qualitatively similar we immediately see that PBE predicts a much smaller bandgap compared to PBE0. Conversely, the difference between the TS and MBD vdW correction schemes are negligible for both PBE and PBE0. Further substantiated by the results shown in Tab 3.4, revealing that the band gaps predicted by TS@PBE0 and MBD@PBE0 are practically identical. A comparison with measurements shows that the TS/MBD@PBE0 band gap compares favorably with measurements TS/MBD@PBE exhibit band gaps that massively underestimate its width even compared to the predictions made for Lithium Hydride. However the hybrid XC-functional results indicate that the physics is described correctly despite the use of measured lattice parameters. Finally, the partial density of states in Fig. 3.24 reveals that the valence and conduction bands potentially are sp-hybridized, which is indicative of a covalent C-H bond.

Vibrational Properties of Thin-Film Pentacene

Analyzing the phonon band structure of thin-film Pentacene allows for further comparisons between the TS and MBD vdW correction schemes. It is shown in Fig. 3.25 and confirms that thin-film Pentacene exhibits high-frequency vibrations up to 95 THz. We find that most modes lay below 50 THz with an isolated band of modes above 90 THz. However, above 20 THz modes become increasingly localized, which is confirmed by sharp peaks in the (species projected) dos (Fig. 3.26). Accordingly, modes above 20 THz are almost flat which

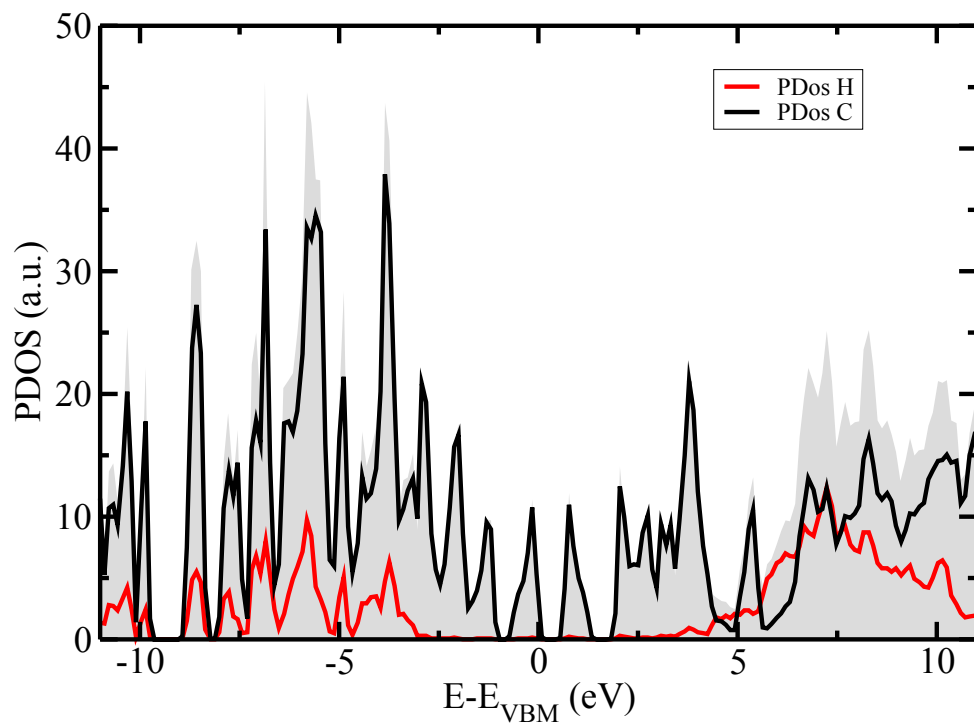


Figure 3.24: Species projected density of states for thin-film Pentacene calculated using MBD@PBE. The red curve shows the Hydrogen contribution the black line the Carbon contribution to the total DOS (grey shaded area).

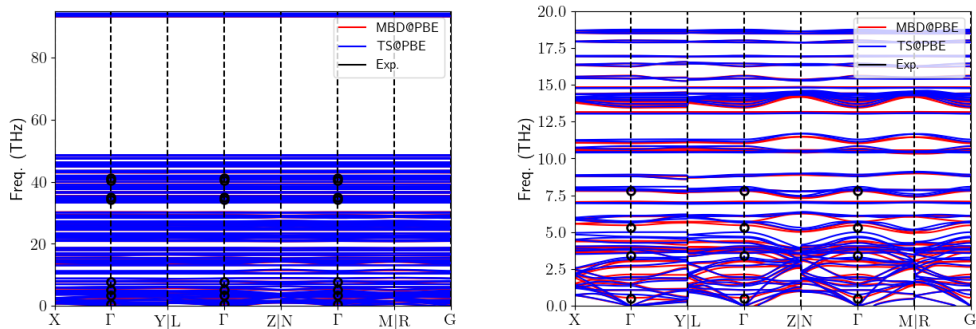


Figure 3.25: Phonon band structure of thin-film pentacene calculated using MBD@PBE (blue) and TS@PBE (red) and results from Raman spectroscopy taken from Ref. [157].

is also mirrored in the TF-DOS in Fig. 3.27. Investigating the species projected density of states reveals that the largest contribution below 20 THz stems from the Carbon atoms. Conversely, above 20 THz we observe an increasing contribution from Hydrogen. Finally, above 90 THz the vibrations are almost exclusively dictated by Hydrogen. Comparing the results of TS@PBE and MBD@PBE shows quantitative differences below 20 THz. Conversely, at higher frequencies, both levels of theories are almost indistinguishable. Since the individual molecules are bonded by van der Waals forces this suggests that the highly localized modes above 20 THz are limited to the constituent molecule chains. For example modes between 33 and 36 THz can be attributed to bending motions of the C-H bond [158]. Since Hydrogen is much lighter than Carbon which is why Hydrogen is the dominant contributor in this frequency range. The isolated band of modes above 90 THz is almost entirely due to stretching of the C-H bonds. Comparing the phonon band structures from TS@PBE and MBD@PBE to experiments show that both levels of theory are consistent with measurements. However, below 20 THz, the MBD@PBE band structure is ever so slightly closer to experimental results. From what we have learned until this point, we can infer that modes above 20 THz will only marginally contribute to the thermal conductivity. Since thin-film Pentacene has no exploitable symmetries, the number of displacements necessary to extract the third-order force constants is in the 100dres of thousands. This makes calculating the κ -DOS prohibitively expensive. However, as we have learned in the previous sections, the frequency-resolved anharmonicity $\sigma(\omega)$ and TF-DOS allow us to proceed regardless. The approximated κ -DOS $\kappa(\omega) \sim \frac{\text{TF}(\omega)}{\sigma_{\text{PIMD}}^{\text{A}}(\omega)}$ in Fig. 3.28 reveals that the heat is mostly carried by modes below 5 THz. Compared to the TF-DOS we see a significant dampening for all higher frequency modes.

3.1.8 The Anharmonicity of Thin-Film Pentacene

For all MD simulations, we chose a $2 \times 2 \times 1$ supercell containing 288 atoms with a $3 \times 3 \times 4$ k-grid and the PBE XC-functional. The high vibrational frequencies necessitate

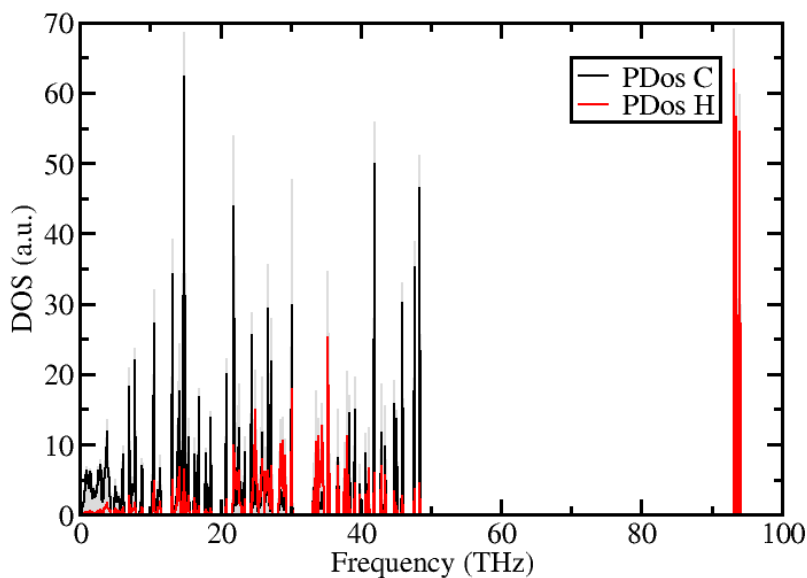


Figure 3.26: Vibrational species projected density of states for thin-film Pentacene calculated using MBD@PBE. The black curve shows the contribution from Carbon, the red curve the contribution from Hydrogen, and the grey shaded area the total density of states.

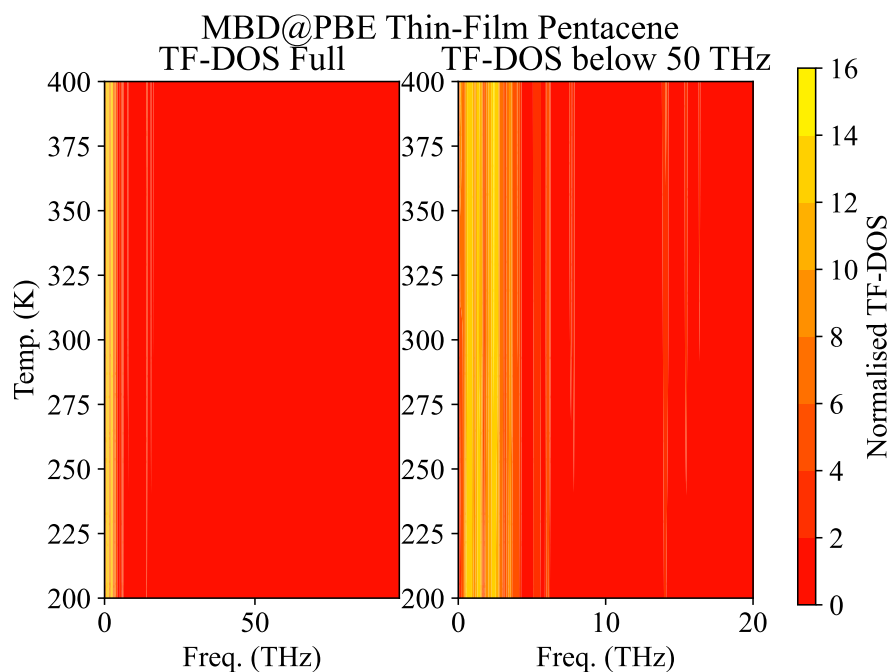


Figure 3.27: Thin-film pentacene transport function density of states from MBD@PBE (full left, below 20 THz right).

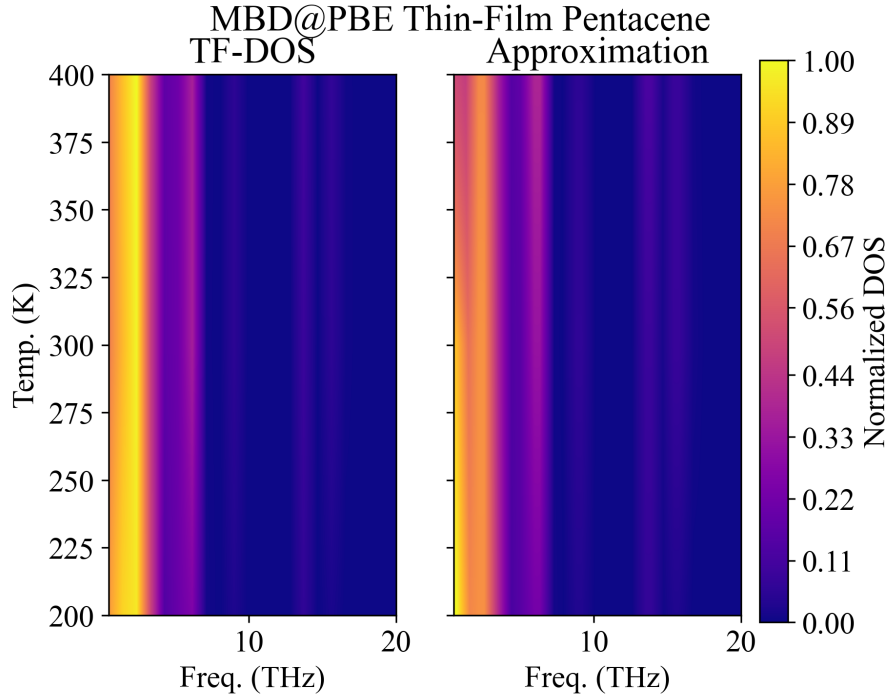


Figure 3.28: Transport function DOS and approximate κ -DOS of thin-film Pentacene calculated using MBD@PBE.

relatively small time steps of 1 fs for aiMD and 0.5 fs for PIMD. Due to the importance of van der Waals interactions in this system and the better agreement with the phonon band structure in Fig 3.25, long-range correlation effects were included using many-body dispersion [103, 104]. As expected QNFs have a pronounced effect on the degree of anharmonicity as shown in Fig. 3.29. We again observe that the inclusion of QNFs leads to a finite anharmonicity at 0 K. However, there are qualitative and quantitative differences between the previously discussed materials. Most importantly, harmonic sampling now underestimates the anharmonicity across the entire temperature range compared to aiMD and PIMD. Above 300 K we also observe a steep anharmonicity increase in aiMD and PIMD. Additionally, the highly anisotropic structure of thin-film Pentacene makes the anharmonicity score direction-dependent. The direction-dependent anharmonicity is defined as:

$$\sigma_a^A = \sqrt{\frac{\langle ((F_{I,a}) - (F_{I,a}^{\text{HA}}))^2 \rangle}{\langle (F_{I,a})^2 \rangle}}. \quad (3.18)$$

Here a denotes the direction and σ^A is given by the trace of σ_a^A . The anharmonicity in x, y, and z-direction are shown in Fig. 3.30. While the values for σ_x^A and σ_y^A are qualitatively and quantitatively similar, quantum nuclear fluctuations are more pronounced in the y direction. The degree of anharmonicity along the z axis, which is roughly parallel to the molecule chains, is smaller compared to other directions. However, it experiences the highest, relative to the other directions, between 300 K and 400 K. The sudden anharmonicity increase

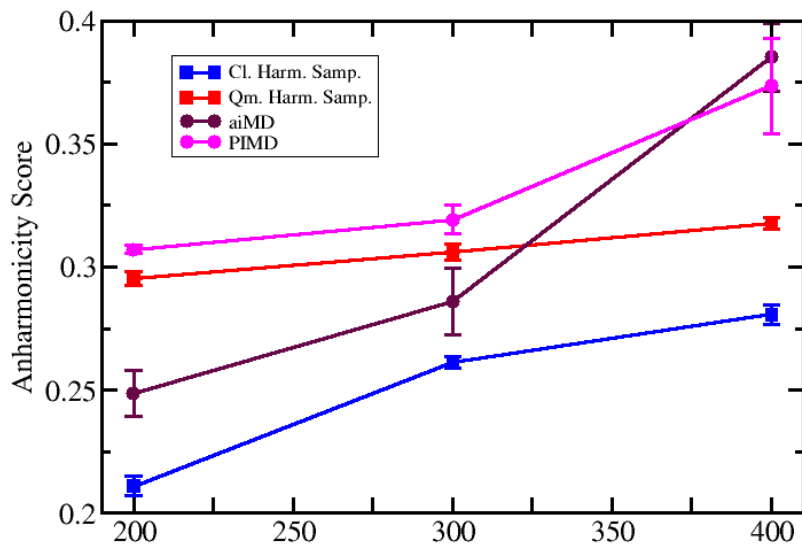


Figure 3.29: Anharmonicity score of thin-film pentacene calculated using classical harmonic sampling (blue), quantum harmonic sampling (red), aiMD (maroon), and PIMD (magenta).

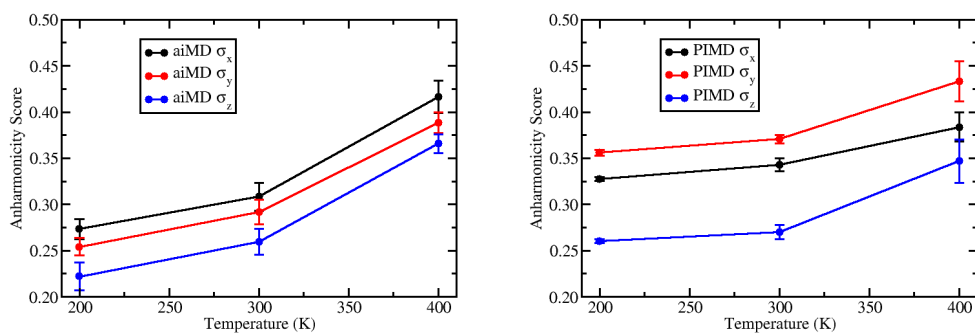


Figure 3.30: Anharmonicity score of thin-film Pentacene in x (black), y (red), and z-direction (blue) from aiMD (left) and PIMD (right).

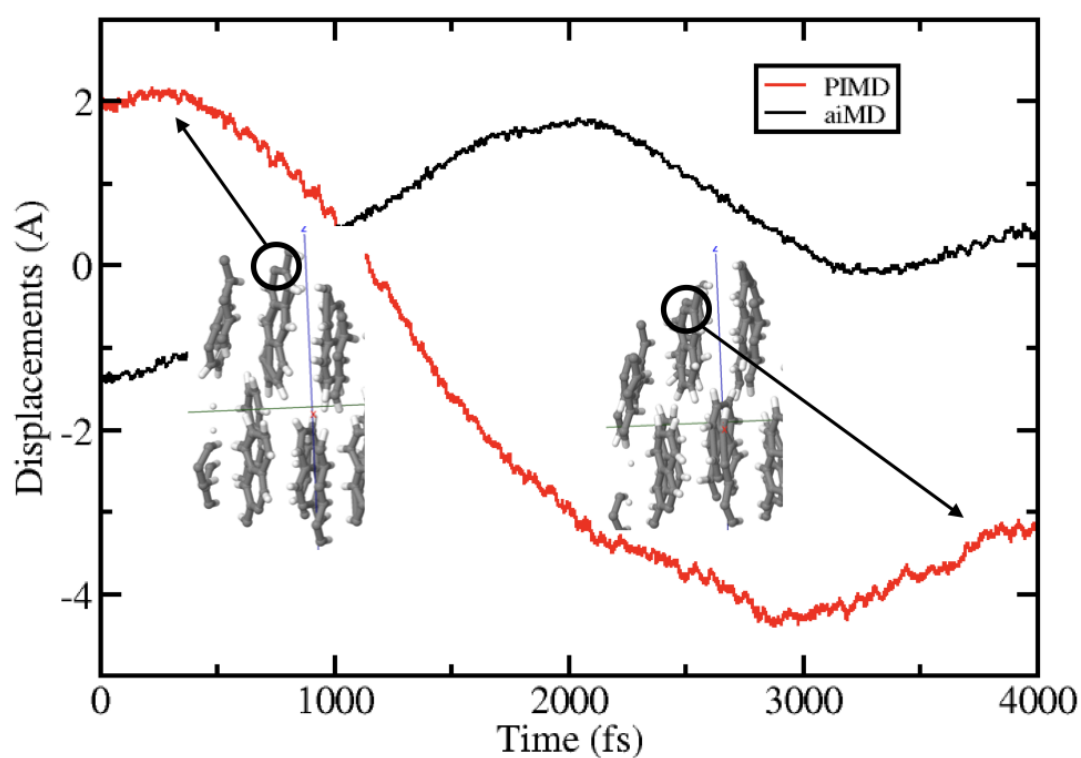


Figure 3.31: Displacements of a Carbon atom in z-Direction at 400 K from PIMD (red) and aiMD (black).

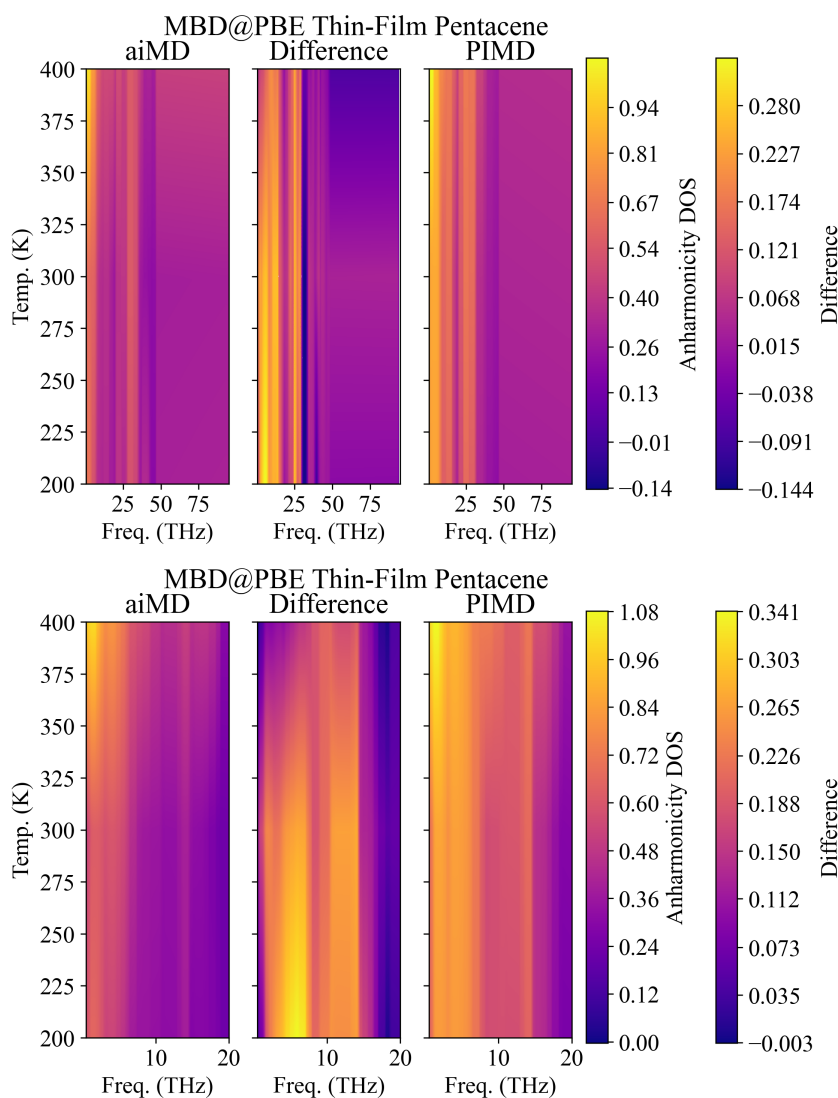


Figure 3.32: The anharmonicity density of states extracted from aiMD (left), PIMD (right), and the difference between both (middle) up to 95 THz (top) and below 20 THz (below).

above 300 K is caused by periodic shifts of the molecule chains in the z -direction, which increases the atomic displacements (see Fig. 3.31). In experiments, it was shown that the α and β angles begin to decrease above 350 K before thin-film Pentacene undergoes a phase transition at 480 K [163]. Conversely, the γ , i.e. the angle between x and y , was shown to remain constant up to 480 K, which is consistent with our simulations. However, at 400 K, we also observe that aiMD and PIMD show the same anharmonicity. For deeper insights, we investigated the anharmonicity density of states $\sigma^{\text{ai/PIMD}}(\omega)$ and their difference, shown in Fig. 3.32. This reveals that QNFs increase the anharmonicity mostly below 15 THz, for all temperatures. Importantly, increased anharmonicity is significant at 400 K. Conversely, above 15 THz, we observe frequency ranges, where aiMD exhibits a higher anharmonicity than PIMD. This is especially pronounced for the high frequent C-H stretch above 90 THz. However, the TF-DOS in Fig. 3.33 and the approximate κ -DOS ins Fig. 3.28 show that the

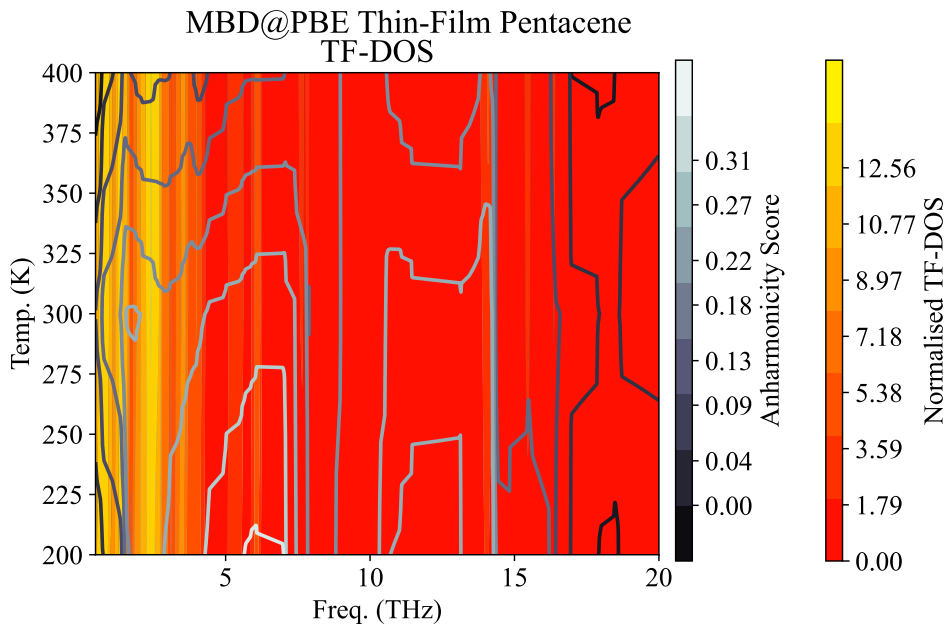


Figure 3.33: Transport function density of states of thin-film Pentacene overlaid with the difference between $\sigma_{\text{aiMD}}^{\text{A}}(\omega)$ and $\sigma_{\text{PIMD}}^{\text{A}}(\omega)$ below 20 THz.

bulk of the heat will be carried by modes below 5 THz. At this frequency range, quantum nuclear fluctuations are highly active for all temperatures.

Results Thin-Film Pentacene

Below 400 K, zero-point motion drives the anharmonicity increased quantum harmonic sampling since classical qualitative similar to PIMD. However, at 400 K we observe a much more complex interplay between anharmonic and quantum nuclear fluctuations. Here, aiMD appeared as anharmonic than PIMD, however, by investigating the frequency resolved anharmonicity, we found that quantum nuclear fluctuations remain active at 400 K below 15 THz. Conversely, at higher frequencies, aiMD appeared as anharmonic as PIMD. However, the frequency-resolved anharmonicity revealed that quantum nuclear fluctuations are active at all temperatures. Comparing the modes that carry the bulk of the heat to those that exhibit the largest increase in anharmonicity due to quantum nuclear fluctuations demonstrates the importance QNFs have on heat transport even at 400 K.

4 Going Beyond what is Currently Possible: Thermal Conductivity from Path Integral Based Methods

As the previous chapter demonstrated QNFs can have a profound impact on the degrees of anharmonicity massively influencing the thermal conductivity. This is further supported by a study conducted, using Temperature Dependent Effective (TDEP) Force Constants, in which it was demonstrated that the thermal conductivity changes massively by accounting for the zero point motion in the Force Constants [140]. While only second and third-order Force Constants were considered, higher orders of anharmonicity are partially accounted for due to the renormalization of Force Constants fitted at a finite temperature. Accordingly, as a suitable (T)RPMD or CMD estimator, accounting for all accessible degrees of anharmonicity and also including quantum nuclear dynamics QNDs beyond ZPM, has been a topic of interest for some time. Partially successful full attempts have been made to find a CMD estimator [?]. However, in the cases cited here, ad-hoc assumptions have been made.

4.1 Deriving the Heat-Flux Estimator

As introduced in Sec 2.2.7, several methods exist to approximate the (Kubo-transformed) correlation function. Likewise, some attempts have been made to find a suitable heat flux estimator for (T)RPMD [120] and CMD [121]. However, in previous publications, known to the author, approximations, such as ignoring all but the centroid variables [120] in RPMD, or not properly accounting for the potential of mean force [121] in CMD. Our focus is primarily on developing a (T)RPMD estimator but the derivation of a CMD heat flux estimator is outlined too.

4.1.1 The Heatflux

Starting from the heat flux definition:

$$\mathbf{J} = \frac{1}{V} \frac{d}{dt} \sum_I \mathbf{R}_I E_I. \quad (4.1)$$

Where \mathbf{R}_I represents the Cartesian vector of the atomic positions of atom I and E_I is formally a “per-atom” energy. Working on the chain rule of the time derivative it is easy to see that:

$$\mathbf{J} = \frac{1}{V} \underbrace{\sum_I \mathbf{v}_I E_I}_{\text{Convective}} + \underbrace{\sum_I \mathbf{R}_I \dot{E}_I}_{\text{Conductive}} \quad (4.2)$$

The convective heat flux mainly occurs due to mass transport, conversely, the conductive heat flux is caused by energy transport. Since the focus of this thesis is on solids the assumption that the convective heat flux is 0 is justified as mass transport at incandescent temperatures is negligible for most systems. Accordingly, we approximate the heat flux as:

$$\mathbf{J} \approx \frac{1}{V} \sum_I \mathbf{R}_I \dot{E}_I. \quad (4.3)$$

4.1.2 The (T)RPMD Heat Flux Estimator

To derive the (T)RPMD heat flux estimator the primitive energy estimator is first written as a per replica and (effective) per atom quantity:

$$E_{I,\alpha} = T_{I,\alpha} - \underbrace{\frac{1}{4} M_I \omega_P^2 [(\mathbf{R}_{I\alpha} - \mathbf{R}_{I\alpha+1})^2 + (\mathbf{R}_{I\alpha-1} - \mathbf{R}_{I\alpha})^2]}_{C_{I,\alpha}} + V_{I,\alpha} \quad (4.4)$$

With the kinetic energy $T_{I,\alpha}$, the coupling energy between different replicas $C_{I,\alpha}$, and the potential energy $V_{I,\alpha}$. Accordingly the complete heat flux estimator reads:

$$\mathbf{J} = \frac{1}{P} \sum_{I,\alpha} \mathbf{R}_{I,\alpha} (\dot{T}_{I,\alpha} - \dot{C}_{I,\alpha} + \dot{V}_{I,\alpha}). \quad (4.5)$$

Since there is no coupling between the different contributions the time derivative of each term can be taken individually, starting with the kinetic energy:

$$\dot{T}_{I,\alpha} = \frac{\mathbf{p}_{I\alpha}}{M_I} \dot{\mathbf{p}}_{I\alpha} = \mathbf{p}_{I\alpha} \mathbf{F}_{I,\alpha}, \quad (4.6)$$

where the force $\mathbf{F}_{I\alpha}$ is given by:

$$\mathbf{F}_{I,\alpha} = -M_I \omega_P^2 [2\mathbf{R}_{I\alpha} - \mathbf{R}_{I\alpha+1} - \mathbf{R}_{I\alpha-1}] - \nabla_{\mathbf{R}_{I,\alpha}} V_\alpha. \quad (4.7)$$

For the coupling terms featuring ω_P , the time derivative yields:

$$\dot{C}_{I,\alpha} = \frac{M_I}{2} \omega_P^2 [(\mathbf{R}_{I\alpha} - \mathbf{R}_{I\alpha+1})(\mathbf{p}_{I\alpha} - \mathbf{p}_{I\alpha+1}) + (\mathbf{R}_{I\alpha-1} - \mathbf{R}_{I\alpha})(\mathbf{p}_{I\alpha-1} - \mathbf{p}_{I\alpha})]. \quad (4.8)$$

Finally, the potential energy time derivative is:

$$\dot{V}_{I,\alpha} = \sum_J \frac{\partial V_{I,\alpha}}{\partial \mathbf{R}_{J,\alpha}} \frac{\mathbf{p}_{J\alpha}}{m'} \quad (4.9)$$

By inserting all derivatives into Eq. 4.5 it becomes immediately obvious that the heat flux estimator decomposes into two main parts, the heat flux originating from the physical potential $V_{I,\alpha}$ \mathbf{J}^{Phys} , which describes the heat flux within each replica, and the heat flux along with the ring polymer \mathbf{J}^{Ring} . We start by analysing \mathbf{J}^{Ring} by adding up the contribution of Eq. 4.7 and 4.8 which yields:

$$\begin{aligned} \mathbf{J}^{\text{Ring}} &= -\frac{1}{2P} \sum_{I\alpha} \omega_P^2 (6\mathbf{R}_{I\alpha}\mathbf{R}_{I\alpha} - 3\mathbf{R}_{I\alpha}\mathbf{R}_{I\alpha+1} - 3\mathbf{R}_{I\alpha}\mathbf{R}_{I\alpha-1} - \mathbf{R}_{I\alpha+1}\mathbf{R}_{I\alpha+1} \\ &\quad - \mathbf{R}_{I\alpha-1}\mathbf{R}_{I\alpha-1} + \mathbf{R}_{I\alpha+1}\mathbf{R}_{I\alpha} + \mathbf{R}_{I\alpha-1}\mathbf{R}_{I\alpha}) \cdot \mathbf{p}_{I\alpha} \end{aligned} \quad (4.10)$$

Here we exploited the cyclic boundary conditions $P+1=0$ of the (T)RPMD Hamiltonian to simplify the expression for \mathbf{J}^{Ring} .

The remaining part can be treated analogously to the classical heat flux expression and \mathbf{J}^{Phys} reads:

$$\begin{aligned} \mathbf{J}^{\text{Phys}} &= \frac{1}{P} \sum_{I\alpha} \mathbf{R}_{I\alpha} \frac{-\partial U_\alpha}{\partial \mathbf{R}_{I\alpha}} \cdot \frac{\mathbf{p}_{I\alpha}}{m'_I} + \sum_{IJ\alpha} \mathbf{R}_{I\alpha} \frac{\partial U_{I\alpha}}{\partial \mathbf{R}_{J\alpha}} \cdot \frac{\mathbf{p}_{J\alpha}}{m'_J} \\ &= \frac{1}{P} \sum_{IJ\alpha} (\mathbf{R}_{J\alpha} - \mathbf{R}_{I\alpha}) \left(\frac{\partial U_{J\alpha}}{\partial \mathbf{R}_{I\alpha}} \cdot \frac{\mathbf{p}_{I\alpha}}{m'_I} \right) \\ &= \frac{1}{P} \sum_{I\alpha} \sigma_{J\alpha} \mathbf{v}_{I\alpha} \end{aligned} \quad (4.11)$$

Here we introduced the index J into the first term and thus were able to rewrite it in terms of the virial stress σ . Finally the sum of both contribution

$$\mathbf{J} = \mathbf{J}^{\text{Bead}} + \mathbf{J}^{\text{Phys}}, \quad (4.12)$$

yields the full heat flux. However, the contribution from the ring heat flux has to vanish. Since the heat flux is defined via Fouriers Law

$$\mathbf{J} = \kappa \nabla T, \quad (4.13)$$

it is a conservative vector field. To calculate the autocorrelation function. Let $\phi : t \rightarrow \mathcal{R}^+$ with $\phi \in [0, 2\pi]$ be a parametrisation along the ring polymer. Then we can write the autocorrelation function of \mathbf{J}^{Bead} as:

$$\langle \mathbf{J}^{\text{Bead}}(\phi(t=0)), \mathbf{J}(\phi(t)) \rangle \propto \lim_{t \rightarrow \infty} \mathbf{J}^{\text{Bead}}(\phi(t=0)) \cdot \int_0^t \mathbf{J}^{\text{Bead}}(\phi(t)) dt = 0. \quad (4.14)$$

Here we exploited that the heat flux is a conservative vector field for which any closed line integral vanishes.

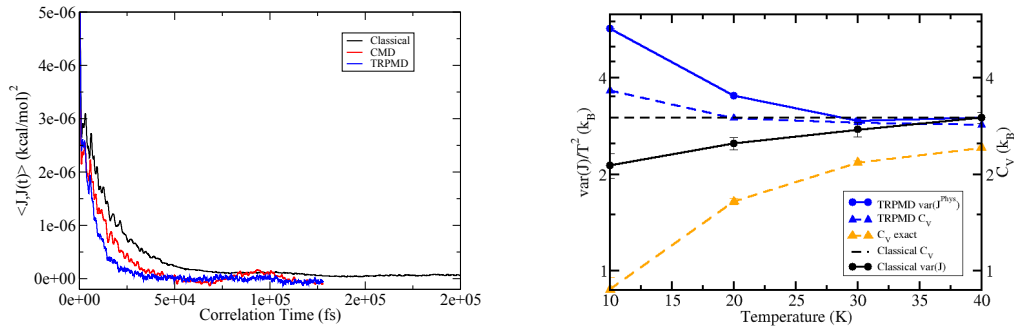


Figure 4.1: Autocorrelation function of J^{Phys} for Lennard-Jones argon calculated from (T)RPMD and clMD at 10 K.

4.1.3 The CMD Heat Flux Estimator

To derive an CMD estimator for the heat flux we need to express the heat flux in terms of the centroid variables $(\mathbf{R}^c, \mathbf{p}^c)$ given by.

$$\mathbf{R}^c = \frac{1}{P} \sum_{\alpha} \mathbf{R}_{\alpha} \quad (4.15)$$

$$\mathbf{p}^c = \frac{1}{P} \sum_{\alpha} \mathbf{p}_{\alpha} \quad (4.16)$$

Thus the centroid heat flux $\mathbf{J}^c = \mathbf{J}(\mathbf{R}^c, \mathbf{p}^c)$ would read

$$\mathbf{J}^c = \sum_I \mathbf{R}_I^c \dot{E}_I^c. \quad (4.17)$$

For all (linear) position dependent quantities this is straight forward. The main question now (at least for me) is how to determine \dot{E}_I^c . I start by defining the energy at the centroid.

$$E_I^c = \frac{\mathbf{p}_I^c \cdot \mathbf{p}_I^c}{2m_I} + U^c(\mathbf{R}_I^c) \quad (4.18)$$

Essentially following the steps from eq. 4.11

$$\mathbf{J}^c = \sum_{IJ} (\mathbf{R}_J^c - \mathbf{R}_I^c) \frac{\partial U^c(\mathbf{R}_J^c)}{\partial \mathbf{R}_I^c} \cdot \dot{\mathbf{R}}_I^c \quad (4.19)$$

Here U^c is the effective potential acting on the centroid. Note that assuming $V^c(\mathbf{R}_C) = V(\mathbf{R}_C)$ would be a significant approximation. The derivation of the CMD heat flux presented above does not include the actual effective potential U^c but rather the physical potential

reevaluated at the centroid position. Thus the energy we use is:

$$E_I^c = \frac{\mathbf{P}_I^c \cdot \mathbf{P}_I^c}{2m_I} + V(\mathbf{R}_I^C) \quad (4.20)$$

In contrast to (T)RPMD, the relevant potential in CMD is the potential of mean force. To write it in the simplest possible way we use the normal mode representation, introduced in Sec 2.2.5, to write the partition function:

$$Z = \int d\tilde{q}_0 dp_c e^{-\beta(T^c + U^c(\tilde{q}_0))} \quad (4.21)$$

Here $U^c(\tilde{q}_0)$ is the mean effective potential as defined in Eq. 2.156 acting on the centroid. We need to compute the time derivative of U^c . To derive the correct CMD heat flux estimator, we have to take the time derivative of $U^c(\tilde{q}_0)$:

$$\begin{aligned} \frac{\partial}{\partial t} U^c(\tilde{q}_0) &= \frac{\partial U^c(\tilde{q}_0)}{\partial t} \\ &= \frac{\partial U^c(\tilde{q}_0)}{\partial \tilde{q}_0} \frac{\partial \tilde{q}_0}{\partial t} \\ &= \frac{1}{P} \sum_{\alpha} \frac{\partial U(\mathbf{R}_{\alpha}(\tilde{q}))}{\partial \tilde{q}_0} \frac{\partial \tilde{q}_0}{\partial t} \\ &= \frac{1}{P} \sum_{\alpha} \frac{\partial U(\mathbf{R}_{\alpha}(\tilde{q}))}{\partial \mathbf{R}_{\alpha}} \frac{\partial \mathbf{R}_{\alpha}}{\partial \tilde{q}_0} \frac{\partial \tilde{q}_0}{\partial t} \\ &= \frac{1}{P} \sum_{\alpha} \frac{\partial U(\mathbf{R}_{\alpha}(\tilde{q}))}{\partial \mathbf{R}_{\alpha}} C_{\alpha 0}^T \frac{\partial \tilde{q}_0}{\partial t} \\ &= \frac{1}{P} \sum_{\alpha} \frac{\partial U(\mathbf{R}_{\alpha})}{\partial \mathbf{R}_{\alpha}} \frac{\partial \mathbf{R}^c}{\partial t} \end{aligned} \quad (4.22)$$

Here $C_{\alpha 0}^T$ is the transposed normal mode transformation. The spring term has no contribution to this derivative as it is taken with respect to the centroid mode alone. Accordingly, the CMD heat flux becomes:

$$\begin{aligned} \mathbf{J}^C &= \sum_{IJ} (\mathbf{R}_J^c - \mathbf{R}_I^c) \frac{1}{P} \sum_{\alpha} \frac{\partial U(\mathbf{R}_{\alpha J})}{\partial \mathbf{R}_{\alpha I}} \cdot \dot{\mathbf{R}}_I^c \\ &= \frac{1}{P^3} \sum_{IJ\alpha\beta\gamma} (\mathbf{R}_{J\beta} - \mathbf{R}_{I\beta}) \frac{\partial U(\mathbf{R}_{\alpha J})}{\partial \mathbf{R}_{\alpha I}} \cdot \dot{\mathbf{R}}_{I\gamma} \end{aligned} \quad (4.23)$$

4.1.4 Outlook

More information can be gathered from the heat flux variance which is roughly proportional to the heat capacity. This is best illustrated by the already introduced microscopic heat

flux:

$$\mathbf{J} = \frac{1}{V_0} \sum_{\mathbf{sq}} E_s(\mathbf{q}, t) \mathbf{v}_s(\mathbf{q}). \quad (4.24)$$

$$\begin{aligned} \text{var}(\mathbf{J}) &= \frac{1}{V_0} \sum_{\mathbf{sq}} \text{var}(E_s(\mathbf{q}, t)) \mathbf{v}_s(\mathbf{q}) \\ &= \frac{k_B T^2}{V_0} \sum_{\mathbf{sq}} C_s(\mathbf{q}) \mathbf{v}_s(\mathbf{q}) \\ C_V(T) &\propto \frac{\text{var}(\mathbf{J})}{k_B T^2}. \end{aligned} \quad (4.25)$$

Here the group velocity is assumed to neither depend on time nor on the temperature. Indeed the classical heat flux exhibits the expected behavior. Conversely, the TRPMD heat flux does not, and increases with decreasing temperature. here the group velocity is assumed to neither depend on time nor on the temperature. Accordingly, the $\text{var}(\mathbf{J})$ has a temperature dependency proportional to the heat capacity. This is exemplified in Fig. 4.1. Indeed the classical heat flux exhibits the expected behavior. Conversely, the TRPMD heat flux does not, and increases with decreasing temperature. For that purpose we tested an ad-hoc correction scheme by defining a (T)RPMD heat capacity:

$$k_B T^2 C_V^{\text{TRPMD}} = \frac{\text{var}(T_{\text{MD}})}{P} + \text{var}(V). \quad (4.26)$$

Here P denotes the total number of replicas. Indeed we find that the TRPMD heat capacity fulfills $C_V^{\text{TRPMD}} \sim \text{var}(\mathbf{J}^{\text{TRPMD}})$. Using the exact PIMD and our TRPMD heat capacity, we then define the following correction scheme:

$$\kappa_{\text{Corrected}} = \kappa^{\text{TRPMD/CMD}} \frac{C_V^{\text{exact}}}{C_V^{\text{TRPMD/CMD}}}. \quad (4.27)$$

This firstly renormalizes the thermal conductivity and secondly enforces the correct variance.

The results are shown in Fig. 4.2. We find that rescaling the thermal conductivity leads to the correct qualitative behavior, i.e, that κ exhibits a finite maximum. However, globally rescaling the thermal conductivity evidently is a blunt tool. Accordingly, the development of a more precise mode-dependent correction is the way forward. The foundation, i.e. a harmonic analysis scheme for the internal ring polymer modes, is defined in Appendix B.

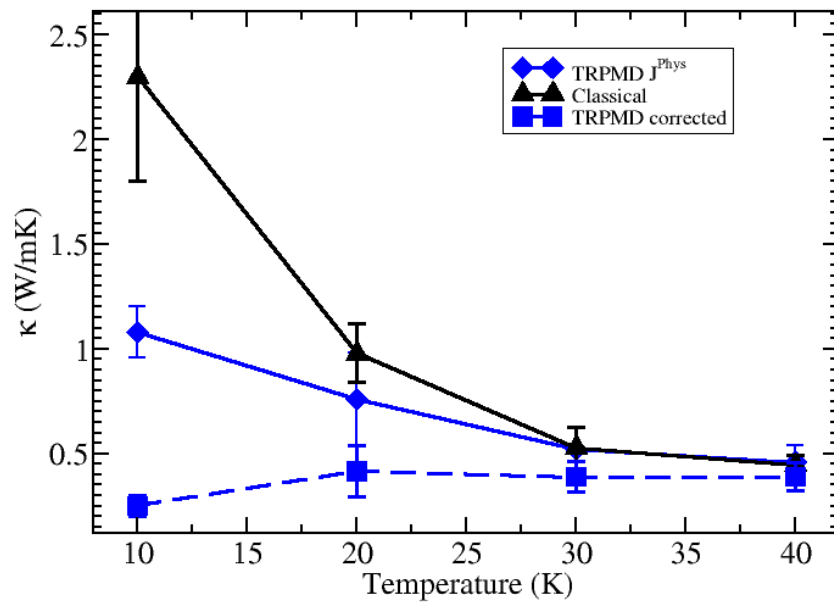


Figure 4.2: Thermal conductivity of Lennard-Jones Argon from cMD, TRPMD, and corrected TRPMD.

5 Conclusion

In this work, we studied the interplay between quantum nuclear fluctuations and anharmonic effects as well as the possible implication for heat transfer problems. As discussed in the introduction, see Sec. 1, quantum-nuclear effects are often assumed to be important in the low-temperature regime, but negligible at higher temperatures. Conversely, anharmonic effects are often thought to be essential to describe the high-temperature limit but to be irrelevant at low temperatures. This work shows that these assumptions are indeed qualitative correct, but that they do not imply that QNFs and anharmonic effects are mutually exclusive. Rather, our research could show that there can be a wide thermodynamic range in which both effects are active and non-negligible. In particular, we could show that there can be a strong interplay between these two effects, e.g., strong QNFs can boost the anharmonicity and vice versa.

To this end, we have used and extended the anharmonicity score σ^A to quantify the strength of anharmonic effects in various solids. As discussed in detail in Sec. 2.3, the anharmonicity measure [112] quantifies the degree of anharmonicity exhibited by a material at finite temperatures. Its definition is derived from the probability distribution of the forces and is the normalized root mean square error of the harmonic model compared to the observed anharmonic forces. By subtracting the harmonic forces from the anharmonic forces In this work, we have extended the original classical definition to also cover quantum-nuclear effects, so as to be applicable to *ab initio* MD and path-integral MD simulations on equal footing.

In a first step, we tested the developed approach using semi-empirical potentials for Tersoff Silicon and Lennard-Jones Argon, two test cases known for being particularly harmonic and anharmonic, respectively. For the more harmonic silicon, anharmonic effects are generally small throughout the whole inspected temperature regime. At and below room temperature, QNFs are significant, though, and lead to a noticeable increase in anharmonicity compared to classical aiMD simulations. In particular, a finite anharmonicity is retained even in the $T \rightarrow 0$ K limit due to quantum nuclear fluctuations. In the high-temperature limit, the classical MD and quantum-mechanical path-integral MD calculations coincide as expected in this very harmonic system. Conversely, much more complex behavior is found for Lennard-Jones Argon. Here, both anharmonicity and QNFs are non-negligible throughout the whole inspected temperature range, so that MD and PIMD never coincide. In this more anharmonic material, already the zero-point motion at 0K induces an anharmonicity in the order of $\sigma^A = 0.4$, which implies that 40% of the interactions are driven by

5 Conclusion

anharmonic effects. Even at these vanishing temperatures, at which anharmonicity would vanish in a classical picture, QNFs lead to a strength in anharmonic effects that is comparable with that of the harmonic ones. In turn, this suggests that perturbative approximations for the anharmonicity – which require $\sigma^A \ll 0.2$ – are inapplicable to this material.

Furthermore, a frequency-resolved analysis of the anharmonicity allowed us to shed light on the nature of these effects. While the anharmonicity in Tersoff Silicon is increased for all modes in an almost uniform fashion, quantum nuclear fluctuations increase the anharmonicity predominantly at low-frequency modes in Lennard-Jones Argon. This is a consequence of the $\sqrt{\frac{1}{\omega}}$ frequency dependence exhibited by zero-point motion. Eventually, a comparison with thermal conductivity calculations and the involved transport kernels, i.e., the thermal conductivity density of states resolved by frequency, allowed us to develop a qualitative model that allows judging when and if QNFs and the associated change in anharmonicity influence thermal conductivity.

In a second step, we applied the developed methodology to DFT-based simulations of Lithium Hydride and thin-film Pentacene, so to clarify if the drawn conclusions hold also for realistic materials. For Lithium Hydride, we indeed observe a similar behavior as in Lennard-Jones Argon: While Lithium Hydride exhibits only a moderate degree of anharmonicity in the classical description, QNFs lead to a significant increase in anharmonicity, leading to an anharmonicity $\sigma^A > 0.2$ that lies beyond the perturbative regime even for very low temperatures. The fact that this QNF-driven increase in anharmonicity is mostly due to those low-frequency modes that are also responsible for heat transport suggest a pronounced impact of QNFs and anharmonicity on thermal conductivity calculations. Qualitatively, similar observations were made also in the simulation of (thin-film) Pentacene, for which again an overall anharmonicity increase is obtained due to quantum nuclear fluctuations. Microscopic analysis reveals that the physical origin of these effects is remarkably different, though. In this case, strongly anharmonic effects related to the phase transition of pentacene at 480 K are already observed at much lower temperatures.

To summarize, these investigations have shown that quantum nuclear fluctuations and anharmonicity can exhibit a strong interplay, both in the low and the high-temperature regime. Particular care has thus to be taken before ruling out either one of these effects due to simple thermodynamic arguments. This is particularly important in the calculation of thermal conductivities since our calculations suggest that the anharmonicity of low-frequency modes, which typically predominantly determine thermal transport, is most affected by QNFs. In the future, this calls for the development of advanced simulation strategies to account for strong anharmonic and quantum nuclear fluctuations on the same footing. The first steps in this direction have been laid out in Sec. 4. There, we have derived the necessary formulas to evaluate the heat flux in path-integral MD simulations. At the current stage, a direct application of this formalism in fully *ab initio* PIMD calculations is hindered by the huge computational cost, since it involves running several large-scale MD

simulations concurrently for a long trajectory length. In this regard, ongoing developments in the field of machine learning might be highly beneficial. Especially regarding machine-learning potentials which have seen impressive results. Kernel-Based potentials have been successfully used to access time and length scales in *ab-initio* simulations that allow for accurate calculations of the thermal conductivity of PBEsol Zirconia [10]. Compared to similarly accurate machine-learning potentials [9] based on artificial neural networks this allows for easy error estimation. Accordingly, the adoption of the Kernel-based method presented in Ref [10] would enable the calculation of the thermal conductivity of multiple materials at different temperatures with near or at *ab initio* Green Kubo levels of accuracy. The benefits would also extend beyond the prediction of the thermal conductivity and make anharmonicity screening or predictions of the relative stability of polymorphs possible at a large scale when combined with the finite time and size correction method demonstrated in Ref. [?]. However, the artificial neural networks method proposed in Ref. [9] is reported to be more accurate for smaller data sets and offered as a python package which means that it would allow for a faster adoption into existing *ab initio* packages as FHI-aims. Especially the small data set size required could prove beneficial and possibly open up even larger time scales at near *ab initio* levels of accuracy.

Bibliography

- [1] E. Schrödinger, *Ann.d.Phys.* 44 916 (1914).
- [2] R. Peierls, *Ann. Phys.* 395, 1055 (1929).
- [3] A. Shakouri *Proceedings of the IEEE*, Vol. 94, No. 8 (2006).
- [4] G. J. Snyder and E. S. Toberer, *Nature Materials* 7, 105 (2008).
- [5] A. G. Evans, D. R. Clarke, and C. G. Levi, *J. Eur. Ceram. Soc.* 28, 1405 (2008).
- [6] A. Jain, et.al., *APL Materials*, 1(1), 011002. (2013).
- [7] R. Ouyang, et.al., *Phys. Rev. Materials* 2, 083802 (2017).
- [8] C. J. Bartel, et. al., *Sci. Adv.* 5, 2 (2019).
- [9] S.Batzner, et.al.,*arXiv:2101.03164* (2021).
- [10] C. Verdi, et.al., *Npj Comput. Mater.* 7, 156 (2021).
- [11] L. de Broglie, *Ann. Phys. (Paris)* 3, 22 (1925).
- [12] M. Born, R. Oppenheimer, *Ann Phys-berlin* 389, 457 (1927).
- [13] R. M. Martin, *Electronic Structure Basic Theory and Practical Methods*, Cambridge University Press, Cambridge (2010)
- [14] F. Jensen, *Introduction to Computational Chemistry*, Wiley (2017).
- [15] P. Hohenberg and W. Kohn. *Phys. Rev.* 136, B864 (1964).
- [16] R.Parr and W. Yang, *Density Functional Theory of Atoms and Molecules*, Oxford University Press, Oxford (1989).
- [17] W. Kohn and L. J. Sham, *Phys. Rev.* 140, A1133 (1965).
- [18] E. Fermi, *Rend. Accad. Naz. Lincei* 6, 32 (1927).
- [19] L. Thomas, *Math. Proc. Cambridge Philos. Soc.* 23, 542 (1927).
- [20] C.F. von Weizsäcker, *Z. Phys.* 96, 431 (1935).
- [21] E. Teller, *Rev. Mod. Phys.* 34, 627 (1962)

Bibliography

- [22] P. K. Acharya, et.al., Proc. Nati. Acad. Sci. USA, 77, 12 (1980).
- [23] Y. A. Wang, Niranjana Govind, and Emily A. Carter Phys. Rev. B 60, 16350 (1999).
- [24] W.C.Witt, et.al. Orbital-free density functional theory for materials research, Cambridge University Press: 02 January (2018).
- [25] H. Chen and A. Zhou, Numer. Math. Theor. Meth. Appl. 1, 1 (2008).
- [26] D. Dickel, M. Nitol, and C. Barrett, arXiv:2102.02345, (2021).
- [27] A.P. Bartok, et.al. Phys. Rev. Lett., 104, 136403 (2010).
- [28] J. P. Perdew and Y. Wang, Phys. Rev. B 45, 13244 (1992).
- [29] P. J. Perdew, et.al., Phys. Rev. Lett., 77, 3865 (1996), Erratum: Phys. Rev. Lett., 78, 1396 (1997).
- [30] P. J. Perdew, et.al., Phys. Rev. Lett, 100 ,136407 (2008).
- [31] Aron J. Cohen, et.,al., Science 321, 5890, 792-794 (2008).
- [32] P. J. Perdew, et.al., J. Chem. Phys., 105, 9982 (1996).
- [33] P. J. Perdew, et.al., Phys. Rev. Lett. 100, 136406 (2008), Erratum: Phys. Rev. Lett. 102, 039902 (2009).
- [34] J. Heyd, G. E. Scuseria, and M. Ernzerhof, J. Chem. Phys. 118, 8207 (2003).
- [35] T. Auckenthaler, et.al, Parallel Comput., vol. 27, no. 12, pp. 783–794, (2011).
- [36] [2] A. Marek, et.al., J. Phys. Condens. Matter, vol. 26, no. 21, p. 213201, (2014).
- [37] P. Kus, et.al. Parallel Computing, 85, 167-177, (2019).
- [38] H.-J. Bungartz, et.al., Parallel Computing: Technology Trends 647-668, (2020).
- [39] P. Pulay, Mol. Phys. 17, 197 (1969).
- [40] K. Esfarjani and H.T. Stokes, Phys. Rev. B 77, 144112 (2008).
- [41] O. Christiansen, J. Chem. Phys., 120, 2149–2159, (2004).
- [42] N. K. Madsen, I. H. Godtlielsen, S. A. Losilla, and O. Christiansen, J. Chem. Phys. 148, 024103 (2018).
- [43] J. M. Bowman, K. Christoffel, and F. Tobin, J. Phys. Chem. 83, 905 (1979).
- [44] 2K. M. Christoffel and J. M. Bowman, Chem. Phys. Lett. 85, 220 (1982).
- [45] Y. Shao, et.al. Mol. Phys, 113, 2, 184–215, (2015).
- [46] Gonze and J.-P. Vigneron, Phys. Rev. B 49, 13 120 (1989).

- [47] R. P. Feynman, *Phys. Rev.* 56, 340 (1939).
- [48] D. Frenkel and B. Smit, *Understanding Molecular Simulation From Algorithms to Applications*, Academic Press, New York, (2002).
- [49] M.E.Tuckerman, *Statistical Mechanics: Theory and Molecular Simulation*, Oxford University Press Inc., New York , (2010).
- [50] J.L. Lebowitz, J.K. Percus, and L. Verlet, *Phys. Rev.*, 153:250–254, (1967).
- [51] J E Lennard-Jones, *Proc. Phys. Soc.*, 43, 461 (1931).
- [52] J. Tersoff, *Phys. Rev. B*, 37, 6991 (1988).
- [53] J. Tersoff, *Phys. Rev. B* 41, 3248 (1990).
- [54] T. Hammerschmidt, P. Kratzer, and M. Scheffler, *Phys. Rev. B* 77, 235303 (2008).
- [55] D. W. Brenner, *Phys. Rev. B*, 42, 9458 (1990).
- [56] S. J. Stuart, A. B. Tutein, and J. A. Harrison, *J. Chem. Phys.* 112, 6472 (2000).
- [57] T. Senftle, S. Hong, and M. Islam, et al., *npj Comput Mater* 2, 15011 (2016).
- [58] A. P. Bartók, M. C. Payne, R. Kondor, and G. Csányi, *Phys. Rev. Lett.* 104, 136403 (2010).
- [59] A. Singraber, J. Behler, and C. Dellago, *J. Chem. Theory Comput.*, 15, 3 (2019).
- [60] T. Tadano and S. Tsuneyuki, *Phys. Rev. B* 92, 054301 (2015).
- [61] G. Bussi, D. Donadio, and M. Parrinello, *J.ChemF.Phys* . 126, 01p4101 (2007).
- [62] P.Dirac, *Physikalische Zeitschrift der Sowjetunion.* 3: 64–72. (1933).
- [63] R P Feynman and A R Hibbs. *Quantum Mechanics and Path Integrals*. McGraw- Hill, New York, (1964).
- [64] G. C. Wick, *Phys. Rev.* 96, 1124 (1954).
- [65] H. F. Trotter, *Proc. Am. Math. Soc.* 10, 545 (1959).
- [66] *Trans. Am. Math. Soc.* 70, 2, 195-211 (1951).
- [67] David Chandler and Peter G Wolynes., *J. Chem. Phys.*, 74(7):4078–4095, (1981).
- [68] M. Parrinello and A. Rahman, *A. J. Chem. Phys.*, 80, 860–867 (1984).
- [69] N. Makri, *Comput. Phys. Commun.* 63, 389 (1991).
- [70] I. H. Duru, H. Kleinert, *Phys. Lett. B*, 84, 2 (1979).
- [71] R. Luo and K. Yu, *J. Chem. Phys.* 153, 194105 (2020).

Bibliography

- [72] R. Kubo, J. Phys. Soc. Jpn. 12, 570 (1957).
- [73] P. C. Howell, J. Chem. Phys. 137, 224111 (2012).
- [74] I. R. Craig and D. E. Manolopoulos, J. Chem. Phys. 121, 3368 (2004).
- [75] I. R. Craig and D. E. Manolopoulos, J. Chem. Phys. 122, 084106 (2005).
- [76] I. R. Craig and D. E. Manolopoulos, J. Chem. Phys. 122, 184503 (2005).
- [77] M. Rossi, M. Ceriotti and D. E. Manolopoulos, J. Chem. Phys. 140, 234116 (2014).
- [78] J. Cao, G.A. Voth, J. Chem. Phys. 100, 5093 (1994).
- [79] J. Cao and G. A. Voth, J. Chem. Phys. 100, 5106 (1994).
- [80] S. Jang and G. A. Voth, J. Chem. Phys. 111, 2371 (1999).
- [81] A. Witt, et.al., J. Chem. Phys. 130, 194510 (2009).
- [82] T. J. H. Hele, et.al., J. Chem. Phys. 142, 134103 (2015).
- [83] D. West and S. K. Estreicher, Phys. Rev. Lett. 96, 22 (2006).
- [84] G. E. P. Box and M. E. Muller, Ann. math. stat. 29, 2 (1958).
- [85] O. Hermann and I. A. Abrikosov, Phys. Rev. B 88 , 144301 (2013).
- [86] S. Biernacki and M. Scheffler, Phys. Rev. Lett. 63, 290 (1989).
- [87] S. Baroni, et.al., Rev. Mod. Phys. 73, 515 (2001).
- [88] X. Gonze and J.-P. Vigneron, Phys. Rev. B 39, 13120 (1989).
- [89] A. Cepellotti, et.al., Nat. Commun., 6, 6400 (2015).
- [90] K. Parlinski, Z.Q. Li, and Y. Kawazoe, Phys. Rev. Lett. 78 (1997).
- [91] A. Togo and I. Tanaka, Scr. Mater., 108, 1-5 (2015).
- [92] A. Togo, L. Chaput, and I. Tanaka, Phys. Rev. B, 91, 094306 (2015).
- [93] J. Garg, et.al., Phys. Rev. Lett. 106, 045901 (2011).
- [94] A. Chernatynskiy and S. R. Phillpot, Phys. Rev. B 82, 134301 (2010).
- [95] C. Carbogno, et.al., Phys. Rev. Lett. 118, 175901 (2017).
- [96] Kubo, M. Yokota, and S. Nakajima, J. Phys. Soc. Japan 12, 1203 (1957).
- [97] E. Helfand, Phys. Rev. 119, 1 (1960).
- [98] Fei Zhou, et.al., Phys. Rev. Lett. 113, 185501 (2014).
- [99] D. C. Wallace, Thermodynamics of Crystals, Dover Publishing Inc., New York (1972).

- [100] V. Blum, et.al., *Comput. Phys. Commun.* 180, 2175-2196 (2009).
- [101] Q. Wu and W. Yang, *J. Chem. Phys.* 116, 515 (2002).
- [102] A. Tkatchenko and M. Scheffler. *Phys. Rev. Lett.*, 102:073005 (2009).
- [103] A. Tkatchenko R.A. DiStasio Jr., R. Car, and M. Scheffler, *Phys. Rev. Lett.* 108, 236402 (2012).
- [104] A. Ambrosetti, A.M. Reilly, R.A. DiStasio Jr., and A. Tkatchenko, *J. Chem. Phys.* 140, 18A508 (2014).
- [105] M.Akasaka, et. al., *J. Cryst. Growth*, 304, 196-201 (2007).
- [106] N. W. Ashcroft, N. D. Mermin, *Solid State Physics*, Saunders College Publishing, New York, (1976).
- [107] G. P. Srivastava, *The Physics of Phonons*, Adam Hilger, Bristol, (1990).
- [108] L. Chaput, *Phys. Rev. Lett.* 110, 265506 (2013).
- [109] A. A. Maradudin and A. E. Fein, *Phys. Rev.*128, 2589 (1962).
- [110] J. Behler, B. Delley, S. Lorenz, K. Reuter, and M. Scheffler, *Phys. Rev. Lett.* 94, 036104 (2005).
- [111] C. Carbogno, J. Behler, A. Groß, and K. Reuter, *Phys. Rev. Lett.* 101, 096104 (2008).
- [112] F. Knoop, et.al., *Phys. Rev. Materials* 4, 083809, (2020).
- [113] F. Birch, *Phys Rev* 71, 809 (1947).
- [114] F. Murnaghan, *Proc. Natl. Acad. Sci.* 30, 244 (1944).
- [115] A. M. Wodtke, J. C. Tully, and D. J. Auerbach, *International Reviews in Physical Chemistry* 23, 513 (2004).
- [116] N. Shenoi, S. Roy, and J. Tully, *Science* 326, 829 (2009).
- [117] M. Akasaka, et.al., *J. Cryst. Growth* 304, 196 (2007).
- [118] T.M. Yamamoto, *J. Chem. Phys.* 123, 104101 (2005).
- [119] R. J. Hardy, *Phys. Rev.* 132, 168 (1963).
- [120] R.Luo, and K. Yu, *J. Chem. Phys.* 153, 194105 (2020).
- [121] Y. Yonetani, K. Kinugawa, *J. Chem. Phys.* 120, 10624 (2004).
- [122] D. S. Kim, et.al., *Proc. Natl. Acad. Sci. U.S.A.*, 115, 9 (2018).
- [123] M. Rossi, P. Gasparotto, M. Ceriotti, *PRL* 117, 115702 (2016).
- [124] M. Ceriotti, et.al., *Chem. Rev.* 2016, 116, 13 (2016).

Bibliography

- [125] G. Nilsson and G. Nelin, *Physical Review B* 6, 3777 (1972).
- [126] T. Middelmann, A. Walkov, G. Bartl, R. Schödel *Phys. Rev. B* 92, 174113, (2015).
- [127] Y. Okada, Y. Tokumaru, *Journal of Applied Physics* 56, 314 (1984).
- [128] L.A. Rowley, D. Nicholson, N.G. Parsonage, *J. Comput. Phys.* 17, 401-414 (1975).
- [129] M. Räsänen, *Nat. Chem.*, 6, 82 (2014).
- [130] A. Cohen, J. Lundell, and R. B. Gerber, *J. Chem. Phys.* 119, 6415 (2003)
- [131] D. N.Batchelder, et.al., *J. Phys. C. Solid State Phys.* 3 249 (1970)
- [132] C. R. Tilford and C. A. Swenson, *Phys. Rev. B* 5, 719 (1972).
- [133] RC Tolman, *Statistical Mechanics, with Applications to Physics and Chemistry.* Chemical Catalog Company, 76-77 (1927).
- [134] R. L. Smith and J. W. Miser *Compilation of the properties of lithium hydride, NASA* (1963).
- [135] S. Baroni, G. P. Parravicini, and G. Pezzica *Phys. Rev. B* 32, 4077 (1985).
- [136] T.Miki,et.al., *Solid State Communications* 39, 5, (1981)
- [137] R.Jaradat, et.al., *A Multinational Journal*, 90, 9, 914-927 (2017).
- [138] J. L. Verble, J. L. Warren, and J. L. Yarnell, *Phys. Rev.*, 168, 3 (1968).
- [139] H. Dammak, E. Antoshchenkova, M. Hayoun, F. Finocchi, *J. Condens. Matter Phys.*,435402, 24 (2012).
- [140] N. Shulumba, O. Hellman, and A. J. Minnich *Phys. Rev. Lett.* 119, 185901 (2017).
- [141] K. R. Glaesemann and L. E. Fried, *J. Chem. Phys.* 117, 3020 (2002).
- [142] Kapil et al., *Comp. Phys. Comm.* 236, 214–223 (2018).
- [143] S. Plimpton, *J Comp Phys*, 117, 1-19 (1995).
- [144] L. Lindsay, *Phys. Rev. B*, 94, 174304 (2016).
- [145] W. Brückner, K. Kleinstück, and G. Schulze, *Phys. Status Solidi* 14, 297 (1966).
- [146] J. Anderson, J. Nasise, K. Philipson, and F. Pretzel, *J. Phys. Chem. Sol.* 31, 613 (1970).
- [147] I.Fieldhouse, J.Hedge, and J. Lang, TR-58-274, WADC, Nov, (1958).
- [148] P. Loubeyre, et.al., *Phys. Rev. B* 57, 10403 (1998).
- [149] A. J. H. McGaughey, M. Kaviany, *Phys. Rev. B* 69, 094303 (2004).

- [150] D. Knipp, et.al. *J Non Cryst Solids* 1042–1046, 99–302 (2002).
- [151] L. Zhou, et.al., *IEEE Electron Device Lett.*, 26,26 (2005).
- [152] J. Jang, *Mater. Today* 9, 4, 46-52 (2006).
- [153] M. Oxborrow, J. D. Breeze, N. M. Alford, *Nature* 488, 353-356 (2012).
- [154] H. Wu, et.al., *Phys. Rev. Applied* 14, 064017 (2020).
- [155] J. C. Mollier, J. Hardin, and J. Uebersfeld, *Rev. Sci. Instrum.* 44, 1763–1771 (1973).
- [156] H. Ishii, et.al., *Electronic Processes in Organic Electronics*, Springer 209 (2015).
- [157] A. Girlando, et.al., *Crystals* 2016, 6, 41 (2016).
- [158] A. Brillante, et.al., *Chem. Phys. Lett.*, 357, 32–36 (2002).
- [159] K. Doi, et.al., *J. Appl. Phys.* 98, 113709 (2005).
- [160] P. Parisse, et.al., *J. Phys.: Condens. Matter* 19, 106209 (2007).
- [161] D. Nabok, et.al., *Phys. Rev. B* 76, 235322 (2007).
- [162] W. F. Kuhs. *Acta Cryst.*, A48, 80-98 (1992).
- [163] A. Moser, et.al., *Appl. Phys. Lett.* 99, 221911 (2011).
- [164] O. L. Griffith, J. E. Anthony, A. G. Jones, D. L. Lichtenberger, *J. Am. Chem. Soc.*, 132, 2, 580–586 (2010)
- [165] G. Bussi, D. Donadio, and M. Parrinello, *J. Chem. Phys.* 126, 014101 (2007).
- [166] P. Turq, F. Lantelme, and H. L. Friedman, *J. Chem. Phys.* 66, 3039 (1977).
- [167] M. Ceriotti, M. Parrinello, T. E. Markland, and D. E. Manolopoulos, *J. Chem. Phys.* 133, 124104 (2010).

A New CV estimator

The most successful implementation of an C_V estimator is the double virial estimator ???. During our research we found a novel alternative formulation which yields the same results. This new estimator takes the form:

$$k_B T^2 C_V = \text{var}(e_{CV} + V_C) + \frac{\langle T_{\text{md}} \rangle}{P\beta} - (\langle e_{CV} \rangle - \frac{\langle T_{\text{md}} \rangle}{P}) \frac{2}{\beta}. \quad (\text{A.1})$$

Here P is the number of beads $V_C = \frac{1}{P} \sum_{\alpha} V_{\alpha}$ and e_{CV} is the virial kinetic energy estimator. In contrast to the double virial estimator no coordinate re-scaling or hessian is required. While this formulation mimics the primitive heat capacity estimator it does not suffer from the same variance problems. However while our new formulation converges slower with respect to the number of replicas, it is best applied to ab-initio PIMD where the computational impact of the coordinate re-scaling and the repeated calculation of the hessian can lead to significant bottlenecks.

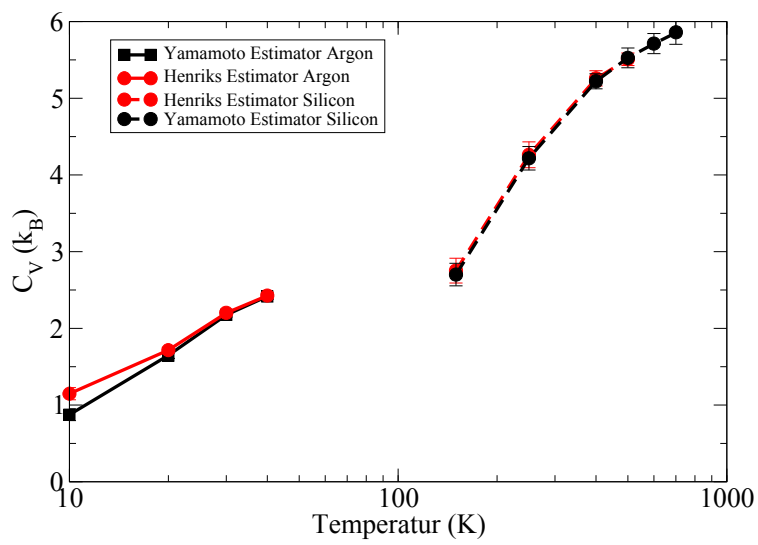


Figure A.1: Our estimator in comparisons with Yamamotos double virial estimator for Lennard-Jones argon and Tersoff silicon

B Harmonic Analysis for Path Integral MD

Based on harmonic analysis, introduced in Sec. 2.3 can be generalized to be applicable to PIMD, (T)RPMD, and other Path Integral based methods. To generalize the concept of harmonic analysis to PI and (T)RPMD it is necessary to account for the "spring" contribution to the potential energy. To form a complete hessian of the system described by the ring polymer Hamiltonian from Eq. 2.131 we rewrite the Hessians of the ring polymer S and of the physical system Φ so that they both have the same dimensions of $3 \times N \times P$ $S_{IJ} = S_I \delta_{IJ}$ ring

$$\begin{aligned} H_P &= \sum_{\alpha} \sum_I \frac{\mathbf{p}_I^{\alpha} \cdot \mathbf{p}_I^{\alpha}}{2M_I} + \frac{1}{2} \sum_{\alpha} \sum_{IJ} \mathbf{R}_I^{T\alpha} \frac{1}{2} S_{IJ}^{\alpha} \mathbf{R}_J^{\alpha} + \frac{1}{2} \sum_{\alpha} \sum_{IJ} \mathbf{R}_I^{T\alpha} \Phi_{IJ}^{\alpha} \mathbf{R}_J^{\alpha} \\ &= \sum_I \frac{\mathbf{p}_I^{\alpha} \cdot \mathbf{p}_I^{\alpha}}{2M_I} + \sum_{\alpha} \sum_{IJ} \mathbf{R}_I^{T\alpha} \left(\frac{1}{2} S_{IJ}^{\alpha} + \frac{1}{2} \Phi_{IJ}^{\alpha} \right) \mathbf{R}_J^{\alpha} \end{aligned} \quad (\text{B.1})$$

We now employ an ansatz similar to the one introduced in Eq. 2.55 but also account for the coordinates of the replicas α however we intend to only Fourier transform the hessian of the physical hessian and leave the ring polymer hessian in real space:

$$\mathbf{R}_{n\hat{I}}^{\alpha} = \frac{1}{\sqrt{M_{\hat{I}}}} \sum_{\gamma \mathbf{q}} A_{\gamma}(\mathbf{q}) e^{i\xi_{\gamma}^{\alpha}(\mathbf{q})} \epsilon_{\gamma}^{\hat{I}\alpha}(\mathbf{q}) e^{i(\mathbf{q} \cdot \mathbf{T}_n - \omega t)} \quad (\text{B.2})$$

The index γ corresponds to the vibrational mode index s from the previous section generalized to include the modes introduced by the ring polymer. Again the eigenvectors ϵ and eigenvalues ω^2 are determined by solving an eigenvalue problem but to account for the "spring" contribution we define a generalised dynamical matrix.

$$\begin{aligned} \text{DS}_{\alpha\hat{I}\beta\hat{J}}(\mathbf{q}) &= \sum_{mn} \left(\frac{S_{\alpha m \hat{I} \beta n \hat{J}}}{\sqrt{M_{\hat{I}} M_{\hat{J}}}} + \frac{\Phi_{\alpha m \hat{I} \beta n \hat{J}}}{\sqrt{M_{\hat{I}} M_{\hat{J}}}} \right) e^{i\mathbf{q} \cdot (\mathbf{T}_m - \mathbf{T}_n)} \\ &= \sum_{mn} \left(\frac{S_{\alpha m \hat{I} \beta n \hat{J}}}{\sqrt{M_{\hat{I}} M_{\hat{J}}}} + \frac{\Phi_{\alpha m \hat{I} \beta n \hat{J}}}{\sqrt{M_{\hat{I}} M_{\hat{J}}}} e^{i\mathbf{q} \cdot (\mathbf{T}_m - \mathbf{T}_n)} \right) \end{aligned} \quad (\text{B.3})$$

Similar to the index α β denotes a replica of the classical system. Strictly speaking, β is not completely independent of α as the interaction between different replicas is limited to the nearest neighbor and thus β could be rewritten in terms of α using Eq. 2.135 but was introduced nonetheless for ease of notation. Furthermore, it is imperative to realize that while the Fourier transform acts on both Hessians (S and Φ) however as the interaction described by S is only between different replicas and not between different nuclei within the

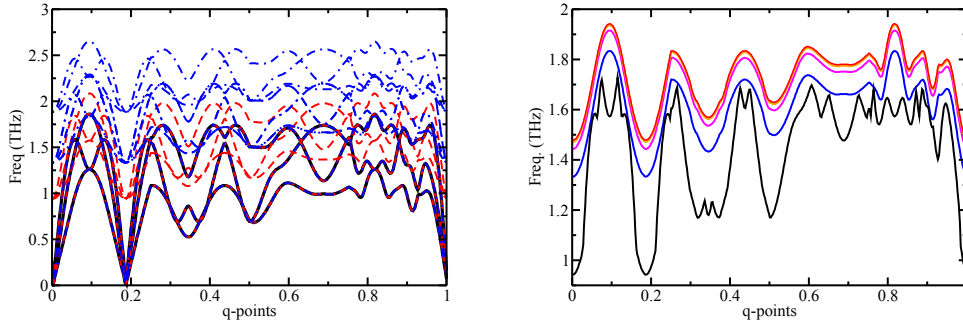


Figure B.1: Both figures show the phonon band structure as obtained from the generalized eigenvalue equation B.3 for Lennard-Jones Argon. The Solid black curves show the results with one replica, the dashed red curves show the results for 2 replicas, and the mixed blue curves show the results for 4 replicas all at a temperature of 10 K. The right figure shows the convergence of the lowest ring polymer mode for different q-points with respect to the number of replicas also at 10 K. Black denotes two replicas, blue denotes four, magenta eight, orange 16, and red 32. Convergence is reached with a number of 16 replicas.

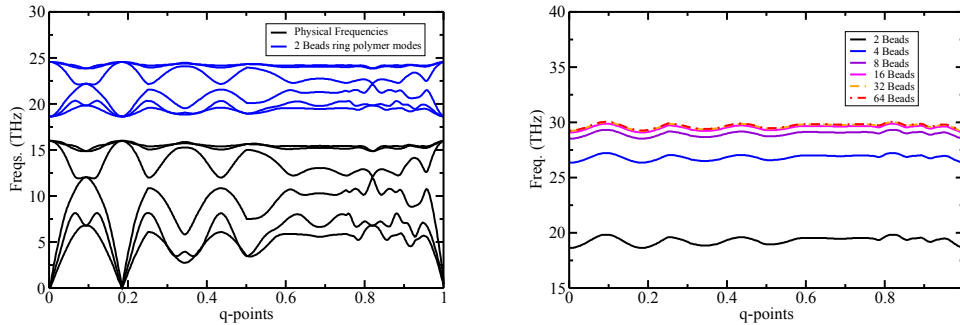


Figure B.2: The left figure shows the phonon band structure as obtained from the generalized eigenvalue equation B.3 for Tersoff silicon. The Solid black curves denote the physical frequencies and the blue curves show the ring polymer modes for a system with two replicas at 100 K. Using only two replicas in the simulation already shows a clean separation between ring polymer and physical modes. The right figure shows the convergence of the lowest ring polymer mode for different q-points with respect to the number of replicas also at 100 K. As can be seen convergence is reached with 32 replicas.

same replica S remains unchanged by the Fourier transform. The corresponding eigenvalue problem now takes the form:

$$\sum_{\beta\hat{J}} DS_{\alpha\hat{I}\beta\hat{J}}(\mathbf{q})\epsilon_{\gamma}^{\beta\hat{J}}(\mathbf{q}) = \omega_{\gamma}^2(\mathbf{q})\epsilon_{\gamma}^{\alpha\hat{I}}(\mathbf{q}). \quad (\text{B.4})$$

An important note about the eigenvectors of the generalized dynamical Matrix shall be proven here

Theorem B.0.1. *Any eigenvector of the generalized dynamical matrix $DS_{\alpha\hat{I}\beta\hat{J}}$ is also an eigenvector of $S_{\alpha\hat{I}\beta\hat{J}}$ and $D_{\alpha\hat{I}\beta\hat{J}}(\mathbf{q})$.*

Proof. Any two symmetric matrices that commute have the same eigenvectors that is the case for $S_{\alpha\hat{I}\beta\hat{J}}$ and $D_{\alpha\hat{I}\beta\hat{J}}(\mathbf{q})$ as they both are symmetric and commute with each other since both are acting on different domains (S describes interaction between the same atoms in different replicas and D describes the interaction within a single replica but between different atoms). Thus the eigenvectors of the generalized dynamical matrix $DS_{\alpha\hat{I}\beta\hat{J}} = S_{\alpha\hat{I}\beta\hat{J}} + D_{\alpha\hat{I}\beta\hat{J}}(\mathbf{q})$ are also eigenvectors of $S_{\alpha\hat{I}\beta\hat{J}}$ and $D_{\alpha\hat{I}\beta\hat{J}}(\mathbf{q})$ ■. \square

Corollary B.0.1.1. *Using Theorem B.0.1 we can conclude that the eigenvalues of the generalized dynamical matrix $DS_{\alpha\hat{I}\beta\hat{J}}$ is the sum of the eigenvalues of $S_{\alpha\hat{I}\beta\hat{J}}$ and $D_{\alpha\hat{I}\beta\hat{J}}(\mathbf{q})$.*

Using this formulation the potential part of the Ring polymer hamiltonian can be written as

$$\begin{aligned} V^{\text{HA}} &= \sum_{m\hat{I}n\hat{J}} \frac{1}{\sqrt{M_{\hat{I}}M_{\hat{J}}}} \sum_{\gamma\mathbf{q}} e^{i\mathbf{q}\cdot\mathbf{T}_n - \mathbf{T}_m} A_{\gamma}^*(\mathbf{q})\epsilon_{\gamma}^{*\alpha\hat{I}}(\mathbf{q}) \frac{1}{2} S_{\alpha m\hat{I}\beta n\hat{J}} A_{\gamma}(\mathbf{q})\epsilon_{\gamma}^{\beta\hat{J}}(\mathbf{q}) \\ &+ \frac{1}{2} \sum_{m\hat{I}n\hat{J}} \frac{1}{\sqrt{M_{\hat{I}}M_{\hat{J}}}} \sum_{\gamma\mathbf{q}} e^{i\mathbf{q}\cdot\mathbf{T}_m - \mathbf{T}_n} A_{\gamma}^*(\mathbf{q})\epsilon_{\gamma}^{*\alpha\hat{I}}(\mathbf{q}) \Phi_{\alpha m\hat{I}\beta n\hat{J}} A_{\gamma}(\mathbf{q})\epsilon_{\gamma}^{\beta\hat{J}}(\mathbf{q}) \\ &= \frac{1}{2} \sum_{\hat{I}\hat{J}} \sum_{\gamma\mathbf{q}} A_{\gamma}^*(\mathbf{q})\epsilon_{\gamma}^{*\alpha\hat{I}}(\mathbf{q}) DS_{\alpha\hat{I}\beta\hat{J}}(\mathbf{q}) A_{\gamma}(\mathbf{q})\epsilon_{\gamma}^{\beta\hat{J}}(\mathbf{q}) \\ &= \frac{1}{2} \sum_{\gamma\mathbf{q}} A_{\gamma}^2(\mathbf{q})\omega_{\gamma}^2(\mathbf{q}) \end{aligned}$$

(B.5)

Here $*$ denotes the complex conjugate. This provides us with a formulation in which we diagonalized total potential. This can largely be replicated for the kinetic energy

$$\begin{aligned} T(\mathbf{q}) &= \sum_{n\hat{I}} \frac{1}{2M_{\hat{I}}} \frac{\partial \mathbf{u}_{n\hat{I}}^*}{\partial t} \frac{\partial \mathbf{u}_{n\hat{I}}}{\partial t} \\ &= \frac{1}{2} \sum_{\gamma\mathbf{q}} \omega_{\gamma}^2(\mathbf{q}) A_{\gamma}^2(\mathbf{q}) \end{aligned} \quad (\text{B.6})$$

Accordingly the total hessian reads

$$\begin{aligned} H &= \sum_{\gamma \mathbf{q}} \omega_{\gamma}^2(\mathbf{q}) A_{\gamma}^2(\mathbf{q}) \\ &= \sum_{\gamma \mathbf{q}} (\omega_{S_{\gamma}}^2 + \omega_{\Phi_{\gamma}}^2(\mathbf{q}))(\mathbf{q}) A_{\gamma}^2(\mathbf{q}) \end{aligned} \quad (\text{B.7})$$

It has to be noted that the (T)RPMD energy is not given by the corresponding Hamiltonian instead the derivative

$$E = \frac{\partial_{\beta} Z}{Z} \quad (\text{B.8})$$

Thus the energy is given by

$$\begin{aligned} E &= \sum_{\gamma \mathbf{q}} \partial_{\beta} (\omega_{S_{\gamma}}^2 + \omega_{\Phi_{\gamma}}^2(\mathbf{q}))(\mathbf{q}) A_{\gamma}^2(\mathbf{q}) \\ &= \sum_{\gamma \mathbf{q}} (\omega_{\gamma}^2(\mathbf{q}) - \omega_{S_{\gamma}}^2)(\mathbf{q}) A_{\gamma}^2(\mathbf{q}) \end{aligned} \quad (\text{B.9})$$

The amplitudes are obtained in a similar way to Eq. ??

$$\begin{aligned} \text{abs}(\mathbf{u}_{\gamma}(\mathbf{q}))^2 + \frac{\text{abs}(\mathbf{v}_{\gamma}(\mathbf{q}))^2}{\omega_{\gamma}^2(\mathbf{q})} &= \frac{A_{\gamma}(\mathbf{q}) \epsilon_{\gamma}^{*\hat{I}}(\mathbf{q}) e^{-i(\mathbf{q} \cdot \mathbf{T}_m - \omega_{\gamma}(\mathbf{q})t + \xi_{\gamma}(\mathbf{q}))} \cdot A_{\gamma}(\mathbf{q}) \epsilon_{\gamma}^{\hat{I}}(\mathbf{q}) e^{i(\mathbf{q} \cdot \mathbf{T}_m - \omega_{\gamma}(\mathbf{q})t + \xi_{\gamma}(\mathbf{q}))}}{\omega_{\gamma}^2(\mathbf{q})} \\ &+ \frac{\omega_{\gamma}^2(\mathbf{q}) A_s(\mathbf{q}) \epsilon_{\gamma}^{*\hat{I}}(\mathbf{q}) e^{-i(\mathbf{q} \cdot \mathbf{T}_m - \omega_{\gamma}(\mathbf{q})t + \xi_{\gamma}(\mathbf{q}))} \cdot A_{\gamma}(\mathbf{q}) \epsilon_{\gamma}^{\hat{I}}(\mathbf{q}) e^{i(\mathbf{q} \cdot \mathbf{T}_m - \omega_{\gamma}(\mathbf{q})t + \xi_{\gamma}(\mathbf{q}))}}{\omega_{\gamma}^2(\mathbf{q})} \\ &= 2A_{\gamma}^2(\mathbf{q}) \epsilon_{\gamma}^{*\hat{I}}(\mathbf{q}) \cdot \epsilon_{\gamma}^{\hat{I}}(\mathbf{q}) \end{aligned} \quad (\text{B.10})$$

Again to obtain the needed we replicate the steps from Eq. ?. Again we can project the positions and velocities along the (T)RPMD trajectory into reciprocal space similar as we have done in Eq. 2.176 and 2.177 with only minor adjustments

$$\mathbf{u}_{\gamma}(\mathbf{q}, t) = \sum_{\alpha m \hat{I}} \frac{1}{\sqrt{M_{\hat{I}}}} e^{i\mathbf{q} \cdot \mathbf{T}_m} \epsilon_{\gamma}^{\alpha \hat{I}}(\mathbf{q}) \mathbf{u}_{m \hat{I}}^{\alpha}(t) \quad (\text{B.11})$$

$$\mathbf{v}_{\gamma}(\mathbf{q}, t) = \sum_{\alpha m \hat{I}} \frac{1}{\sqrt{M_{\hat{I}}}} e^{i\mathbf{q} \cdot \mathbf{T}_m} \epsilon_{\gamma}^{\alpha \hat{I}}(\mathbf{q}) \mathbf{v}_{m \hat{I}}^{\alpha}(t) \quad (\text{B.12})$$

The only difference is that one also carries the index α denoting the respective replica. has to be taken. If we first take a look at the (T)RPMD Hamiltonian in normal mass-weighted

(projected) modes we get

$$\begin{aligned}
H &= \sum_{\gamma\mathbf{q}} \frac{1}{2} \mathbf{v}_\gamma(\mathbf{q}) \mathbf{v}_\gamma(\mathbf{q}) + \sum_{\gamma\mathbf{q}} \frac{1}{2} \omega_{S_\gamma}^2 \mathbf{u}_\gamma(\mathbf{q}) \mathbf{u}_\gamma(\mathbf{q}) + \sum_{\gamma\mathbf{q}} \frac{1}{2} \omega_{\Phi_\gamma}^2(\mathbf{q}) \mathbf{u}_\gamma(\mathbf{q}) \mathbf{u}_\gamma(\mathbf{q}) \\
&= \sum_{\gamma\mathbf{q}} \frac{1}{2} \mathbf{v}_\gamma(\mathbf{q}) \mathbf{v}_\gamma(\mathbf{q}) + \sum_{\gamma\mathbf{q}} \frac{1}{2} (\omega_{S_\gamma}^2 + \omega_{\Phi_\gamma}^2(\mathbf{q})) \frac{1}{2} \mathbf{u}_\gamma(\mathbf{q}) \mathbf{u}_\gamma(\mathbf{q}) \\
&= \sum_{\gamma\mathbf{q}} \frac{\omega_{S_\gamma}^2 + \omega_{\Phi_\gamma}^2(\mathbf{q})}{2} \left(\frac{\mathbf{v}_\gamma(\mathbf{q}) \mathbf{v}_\gamma(\mathbf{q})}{\omega_{S_\gamma}^2 + \omega_{\Phi_\gamma}^2(\mathbf{q})} + \mathbf{u}_\gamma(\mathbf{q}) \mathbf{u}_\gamma(\mathbf{q}) \right) \\
&= \sum_{\gamma\mathbf{q}} (\omega_{S_\gamma}^2 + \omega_{\Phi_\gamma}^2(\mathbf{q})) A_\gamma^2(\mathbf{q}) \tag{B.13}
\end{aligned}$$

The Φ and the S denote the eigenvalues of the physical and spring hessian respectively. The corresponding energy estimator can be obtained from Eq. ?? and is

$$\begin{aligned}
E_{\gamma\mathbf{q}} &= \partial_\beta \beta \frac{\omega_{S_\gamma}^2 + \omega_{\Phi_\gamma}^2(\mathbf{q})}{2} \left(\frac{\mathbf{v}_\gamma(\mathbf{q}) \mathbf{v}_\gamma(\mathbf{q})}{\omega_{S_\gamma}^2 + \omega_{\Phi_\gamma}^2(\mathbf{q})} + \mathbf{u}_\gamma(\mathbf{q}) \mathbf{u}_\gamma(\mathbf{q}) \right) \\
&= \frac{\omega_{S_\gamma}^2 + \omega_{\Phi_\gamma}^2(\mathbf{q})}{2} \left(\frac{\mathbf{v}_\gamma(\mathbf{q}) \mathbf{v}_\gamma(\mathbf{q})}{\omega_{S_\gamma}^2 + \omega_{\Phi_\gamma}^2(\mathbf{q})} + \mathbf{u}_\gamma(\mathbf{q}) \mathbf{u}_\gamma(\mathbf{q}) \right) + \beta \partial_\beta \frac{\omega_{S_\gamma}^2 + \omega_{\Phi_\gamma}^2(\mathbf{q})}{2} \left(\frac{\mathbf{v}_\gamma(\mathbf{q}) \mathbf{v}_\gamma(\mathbf{q})}{\omega_{S_\gamma}^2 + \omega_{\Phi_\gamma}^2(\mathbf{q})} + \mathbf{u}_\gamma(\mathbf{q}) \mathbf{u}_\gamma(\mathbf{q}) \right) \\
&= \frac{\omega_{S_\gamma}^2 + \omega_{\Phi_\gamma}^2(\mathbf{q})}{2} \left(\frac{\mathbf{v}_\gamma(\mathbf{q}) \mathbf{v}_\gamma(\mathbf{q})}{\omega_{S_\gamma}^2 + \omega_{\Phi_\gamma}^2(\mathbf{q})} + \mathbf{u}_\gamma(\mathbf{q}) \mathbf{u}_\gamma(\mathbf{q}) \right) + \beta \partial_\beta \left(\frac{\omega_{S_\gamma}^2 + \omega_{\Phi_\gamma}^2(\mathbf{q})}{2} \right) \left(\frac{\mathbf{v}_\gamma(\mathbf{q}) \mathbf{v}_\gamma(\mathbf{q})}{\omega_{S_\gamma}^2 + \omega_{\Phi_\gamma}^2(\mathbf{q})} + \mathbf{u}_\gamma(\mathbf{q}) \mathbf{u}_\gamma(\mathbf{q}) \right) \\
&+ \beta \left(\frac{\omega_{S_\gamma}^2 + \omega_{\Phi_\gamma}^2(\mathbf{q})}{2} \right) \partial_\beta \left(\frac{\mathbf{v}_\gamma(\mathbf{q}) \mathbf{v}_\gamma(\mathbf{q})}{\omega_{S_\gamma}^2 + \omega_{\Phi_\gamma}^2(\mathbf{q})} + \mathbf{u}_\gamma(\mathbf{q}) \mathbf{u}_\gamma(\mathbf{q}) \right) \\
&= \frac{\omega_{S_\gamma}^2 + \omega_{\Phi_\gamma}^2(\mathbf{q})}{2} \left(\frac{\mathbf{v}_\gamma(\mathbf{q}) \mathbf{v}_\gamma(\mathbf{q})}{\omega_{S_\gamma}^2 + \omega_{\Phi_\gamma}^2(\mathbf{q})} + \mathbf{u}_\gamma(\mathbf{q}) \mathbf{u}_\gamma(\mathbf{q}) \right) + \left(\frac{-2\omega_{S_\gamma}^2}{2} \right) \left(\frac{\mathbf{v}_\gamma(\mathbf{q}) \mathbf{v}_\gamma(\mathbf{q})}{\omega_{S_\gamma}^2 + \omega_{\Phi_\gamma}^2(\mathbf{q})} + \mathbf{u}_\gamma(\mathbf{q}) \mathbf{u}_\gamma(\mathbf{q}) \right) \\
&- \left(\frac{-2\omega_{S_\gamma}^2}{2} \right) \left(\frac{\mathbf{v}_\gamma(\mathbf{q}) \mathbf{v}_\gamma(\mathbf{q})}{\omega_{S_\gamma}^2 + \omega_{\Phi_\gamma}^2(\mathbf{q})} \right) \\
&= \frac{\omega_{S_\gamma}^2 + \omega_{\Phi_\gamma}^2(\mathbf{q})}{2} \left(\frac{\mathbf{v}_\gamma(\mathbf{q}) \mathbf{v}_\gamma(\mathbf{q})}{\omega_{S_\gamma}^2 + \omega_{\Phi_\gamma}^2(\mathbf{q})} + \mathbf{u}_\gamma(\mathbf{q}) \mathbf{u}_\gamma(\mathbf{q}) \right) + \left(\frac{-2\omega_{S_\gamma}^2}{2} \right) (\mathbf{u}_\gamma(\mathbf{q}) \mathbf{u}_\gamma(\mathbf{q})) \\
&= \frac{\omega_{S_\gamma}^2 + \omega_{\Phi_\gamma}^2(\mathbf{q})}{2} \frac{\mathbf{v}_\gamma(\mathbf{q}) \mathbf{v}_\gamma(\mathbf{q})}{\omega_{S_\gamma}^2 + \omega_{\Phi_\gamma}^2(\mathbf{q})} + \frac{\omega_{\Phi_\gamma}^2(\mathbf{q}) - \omega_{S_\gamma}^2}{2} \mathbf{u}_\gamma(\mathbf{q}) \mathbf{u}_\gamma(\mathbf{q})
\end{aligned}$$

Here we have used that $\beta \partial_\beta \omega_{S_\gamma}^2 = -2\omega_{S_\gamma}^2$ as $\omega_{S_\gamma}^2$ depends inversely on β^2 due to the definition of $\omega_P = \frac{P}{\hbar\beta}$ which is always a prefactor to any eigenvalue of the spring hessian. The single contribution to the energy can easily be decomposed into the "classical" kinetic energy $T_\gamma^{\text{MD}}(\mathbf{q})$, the quantum kinetic energy $T_\gamma^{\text{QM}}(\mathbf{q})$, and the potential energy of the physical system $V_\gamma(\mathbf{q})$. They are given by

$$T_\gamma^{\text{MD}}(\mathbf{q}) = \frac{\mathbf{v}_\gamma^2(\mathbf{q})}{2} \tag{B.15}$$

$$T_\gamma^{\text{QM}}(\mathbf{q}) = -\frac{\omega_{S_\gamma}^2 \mathbf{u}_\gamma^2(\mathbf{q})}{2} \tag{B.16}$$

$$V_\gamma(\mathbf{q}) = \frac{\omega_{\Phi_\gamma}^2(\mathbf{q}) \mathbf{u}_\gamma^2(\mathbf{q})}{2} \tag{B.17}$$

Using this the mode projected lifetimes were calculated for two different cases one where the quantum kinetic energy is included and one where it is omitted. From there we calculated the average vibrational Lifetime to compare them to the results obtained from the autocorrelation function of \mathbf{J}^{Phys} . The results are shown in Fig ?? and while the average lifetime calculated from the energy including the quantum kinetic energy agrees well with the average lifetime obtained from \mathbf{J}^{Phys} qualitative and quantitatively the average lifetime obtained while omitting the quantum kinetic energy show major quantitative deviation from the results based on \mathbf{J}^{Phys} .

Correcting the Erroneous Heat-flux Variance with Surgical Precision: A Peek into the not so Distend Future

Using harmonic analysis the erroneous heat capacity can be corrected much more precisely.

C Publications

C.1 Optimizations of the Eigensolvers in the ELPA Library: Testing Autotuning under Production Conditions

This publication focused on CPU and GPU optimizations of the ELPA library e.g. the then-new Intel Xeon Skylake architecture and its AVX-512 instruction set as well as on the redefined API which enables the user to tune many internal parameters such as the highly hardware optimized¹ ELPA 2 kernel. Additionally, the new API allowed for the implementation of an autotuning functionality that automatically identifies the optimal parameters on the fly by repeatedly solving similar eigenvalue problems always changing the combination of parameters. Which parameters are tuned can either be set manually or via predefined autotuning "levels". To showcase the performance benefits to practical applications we performed benchmark calculations for two periodic systems, i.e. an A-DNA double helix (unit cell with 7150 atoms, 77220 basis functions) and graphene (unit cell with 5000 atoms, 70000 basis functions) using the PBE XC-functional [29]. Two different levels of autotuning were tested: FAST which only tunes with respect to the ELPA Kernel and MEDIUM which also optimizes the blocking parameter of the back transformation. Since ELPA 2 is superior for these specific problems we excluded ELPA 1 from the autotuning procedure. The calculations were performed on 32 nodes with 2 CPUs each (20 cores per CPU @2.4 THz). The accumulated run times for A-DNA in Fig. C.1 compare three different scenarios, the GENERIC kernel to which FHI-aims defaults if not specified otherwise, MEDIUM level autotuning, and the optimal setting of MEDIUM level autotuning as if they were known from the beginning. To this end three different scenarios While autotuning introduces a slight computational overhead at the start the overall run time is reduced by about 5%. Similar performance gains are observed in graphene where autotuning MEDIUM leads to a 10% reduction in run time after 160 SCF steps. Tuning only the Kernel (autotuning FAST) leads to similar results but requires significantly fewer steps to find the optimal settings (see Tab. C.1). However even the 15 steps necessary for FAST autotuning makes is unsuited for most single point calculation which typically require 15-30 SCF steps. However most DFT calculation require more than just one SCF-cycle. Relaxations typically require several 100 SCF-steps while for ab initio MD this number can even be in the millions. Since the structure is slightly changed we used the default

¹Different version exist optimized e.g. for different versions of the AVX instruction set, Nvidia/AMD GPUs, and more

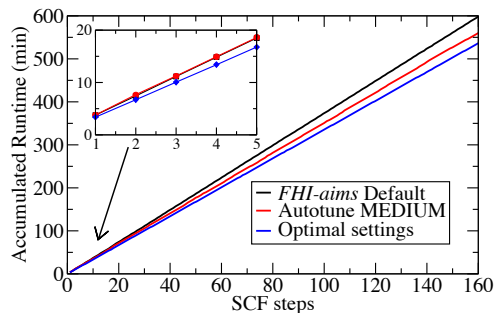


Figure C.1: Accumulated runtime (in minutes) for A-DNA (see text) in three different scenarios: Using FHI-aims’ default settings, using autotuning level MEDIUM, and using optimal settings, as if these were known from the start. There is a clear benefit of autotuned version over the FHI-aims default one. Moreover, if more SCF iterations were done, the *relative* difference between the autotuned and optimal version would be further reduced.

Table C.1: Average runtime per SCF step for the A-DNA (77220 basis functions) and Graphene (70000 basis functions) systems for different kernels and autotuning methods. Autotuning level FAST requires 15 SCF steps (20 steps performed in total) to identify the optimal kernel (AVX-512), while autotuning level MEDIUM requires 150 SCF steps (160 steps performed in total). As a reference, timings for using FHI-aims’ default settings (Generic kernel) and for using the optimal settings from the start, i.e., the ones identified by autotuning MEDIUM, are given.

System	Generic	Optimal	FAST	MEDIUM
A-DNA	221.3 s	200.5 s	209.2 s	209.6 s
Graphene	160.8 s	137.0 s	143.5 s	144.4 s

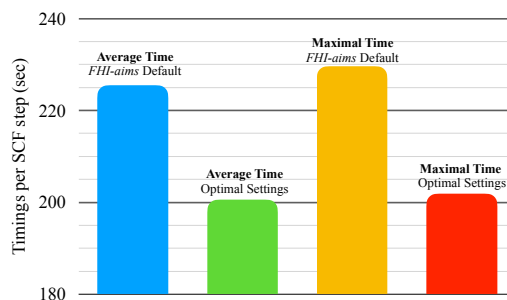


Figure C.2: Average and maximum runtime per SCF steps were observed for ten different geometries of A-DNA (see text), as they would be observed in structure relaxations or *ab initio* Molecular Dynamics simulations. Here, we compare timings for the default and the optimal settings.

and optimal settings to benchmark the average run times for configurations that are typically observed in aiMD simulations (Fig. C.2). This reveals that the performance gains stay consistent across all tested geometries demonstrating the transferability of the autotuning results. Accordingly, the procedure is especially suited for relaxations or aiMD simulations where 5-10% better performance quickly adds up potentially allowing for longer trajectories.

C.1.1 A Parallel Solver for the Generalized Eigenvalue Problem: Optimized GPU Offloading from Autotuning

In App. C.1 we demonstrated the potential performance gains that are possible with ELPAs' Autotuning functionality on CPU nodes. However, in the past years, general-purpose GPU (GPGPU) computing has become widely adopted in high-performance computation. Accordingly, GPGPU compute is also an important component in ELPAs' Autotuning functionality. This is exemplified in Fig. C.3, which shows FHI-aims [100] calculations for periodic Caesium Chloride crystals using the PBE XC-functional [29] with respect to the number of basis functions used. For this purpose, we performed calculations at different sized supercells, i.e., with differing numbers of atoms which naturally increases the total number of basis functions since FHI-aims employ local atomic orbitals. ELPA1 and ELPA2 were tested separately at all system sizes, and for both, CPU-only calculations, as well as calculations using CPUs and full GPU acceleration (for the tridiagonalization, the solution of the eigenvalue problem, and the back transformation), were performed on four Intel Skylake (Xeon Gold 6138) + Nvidia Tesla V100 nodes with two CPUs and GPUs each (20 cores/CPU @ 2.0 GHz). Fig. C.3 shows that GPU acceleration offers a sizeable performance increase for larger systems. However, the threshold number of basis functions at which GPUs accelerate the calculation compared to CPU-only calculations is essentially determined by the workload on each CPU and GPU. For too small systems the overhead, introduced by data transfers to the GPUs, is larger than the potential performance benefit. For this system, GPU acceleration is beneficial for ELPA1 above

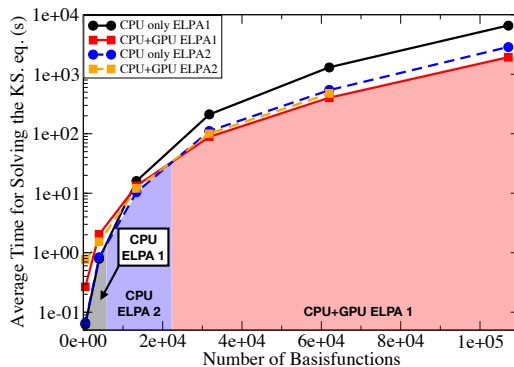


Figure C.3: Computational time per SCF step (in seconds) as function of the numbers of basis functions employed. Solid lines denote ELPA1, dashed lines ELPA2 calculations. CPU-only and CPUs+GPU calculations were performed. The shaded areas denote which setups is fastest for different system sizes. The inset shows

10000 basis functions and for ELPA2 above 20000 basis functions. We also see that for more than 100000 basis functions GPU ELPA1 outperforms GPU ELPA2, which is inverted when only pure CPU computations are considered. This is somewhat counterintuitive, as it is typically assumed that ELPA2 is superior to ELPA1 for large systems, which highlights the usefulness of Autotuning in identifying the optimal settings. We verified this by running Autotuning for 13392 and 31477 basis functions respectively whereby the CPU Kernel was fixed to AVX512. The results in Tab. C.2 reveals that in neither case CPU-only or full GPU accelerations are optimal but that it is beneficial to use GPU acceleration only for tridiagonalization and back transformation while the eigenvalue problem is best solved on the CPU.

Number of Basis functions	ELPA1	ELPA1	ELPA2	ELPA2	Optimal
	CPU-only	CPU+GPU	CPU-only	CPU+GPU	
13,392	16.03s	13.29s	10.38s	12.05s	10.38s
31,744	211.40s	89.38s	110.90s	99.72s	88.73s

Table C.2: Computational time required for solving the KS equations in seconds for ELPA1 and ELPA2 (CPU-only and CPU+GPU calculations) as well as for the optimal settings found by ELPA’s autotuning functionality.

D Thermostats

D.1 Classical

D.1.1 Nose-Hoover Thermostat

One successful approach is to extend the systems, Hamilton, by adding a fictitious oscillator to the original systems hamiltonian:

$$H_{\text{NS}} = H + \frac{p_\eta^2}{2Q} + 3Nk_B T \eta \quad (\text{D.1})$$

This requires a new set of equations of motion

$$\dot{\mathbf{R}}_I = \frac{\mathbf{P}_I}{M_I} \quad (\text{D.2})$$

$$\dot{\mathbf{p}} = \mathbf{F}_I - \frac{p_\eta}{Q} \mathbf{P}_I \quad (\text{D.3})$$

$$\dot{\eta} = \frac{p_\eta}{Q} \quad (\text{D.4})$$

$$\dot{p}_\eta = \sum_I \frac{\mathbf{P}_I^2}{M_I} - 3Nk_B T \quad (\text{D.5})$$

The momenta are damped by the fictitious oscillator. These equations are proven to generate a canonical distribution as introduced in Eq. 2.96. This way of controlling the temperature is not without its drawbacks. For example problems regarding ergodicity can occur causing the system not to explore the entire phase space. Solutions for this exist, such as attaching more fictitious oscillators. An in-depth discussion of this problem can be found in [49].

D.1.2 Langevin Thermostat

Using the Langevin thermostat [166] the time evolution of the momentum is no longer only determined by the equation of motion but by the Langevin equation:

$$M_I \ddot{\mathbf{R}}_I = \mathbf{F}_I - \frac{1}{\tau} \dot{\mathbf{R}}_I + \sqrt{\frac{2M_I}{\tau\beta}} d\xi(t). \quad (\text{D.6})$$

Here τ is the relaxation time of the thermostat and $d\xi(t)$ the Wiener measure. The first part of this equation is simply the equation of motion of the system added to this is a friction term, which exerts a dampening force on the nuclei with the frequency $1/\tau$. A Langevin thermostat has certain advantages as it is ergodic and samples the canonical ensemble. However, it strongly depends on the choice of the relaxation time τ . Additionally, the Langevin thermostat also disturbs the dynamics of the nuclei.

D.1.3 Stochastic Velocity Rescaling Thermostat

The stochastic velocity rescaling (SVR) thermostat was introduced in 2007 by Bussi, Donadio, and Parrinello [165]. They propose the following procedure:

- Evolve the system for a time step with the equation of motion, using for example Velocity Verlet.
- Calculate the temperature.
- Evolve the temperature for the length of a timestep using auxiliary continuous stochastic dynamics.
- Rescale the velocities accordingly.

The velocity rescaling factor is given by:

$$\alpha = \sqrt{\frac{\bar{T}}{T}}. \quad (\text{D.7})$$

Here T is the kinetic energy and $\bar{T} = \frac{N}{2\beta}$ the average kinetic energy and N the number of degrees of freedom. In practise, α uses the target kinetic energy T_t instead of average kinetic energy. The evolution of the kinetic energy is governed by the stochastic differential equation:

$$dT = (\bar{T} - T(t)) \frac{dt}{\tau} - 2\sqrt{\frac{T(t)\bar{T}}{3N\tau}} dW. \quad (\text{D.8})$$

Here dW is the Wiener measure and τ is the relaxation time which determines the coupling of the thermostat to the physical system. Compared to a Langevin thermostat, the SVR thermostat is far less sensitive to the choice of relaxation time and also better preserves the dynamics of the physical system.

D.2 Quantum

D.2.1 Path Integral Langevin Dynamics

Given that the different replicas are connected by harmonic springs a representation in normal modes is possible. The matrix elements associated with this transformation are given by:

$$C_{\alpha 0} = \sqrt{\frac{1}{P}} \quad (\text{D.9})$$

$$C_{\alpha\beta < \frac{P-2}{2}} = \sqrt{\frac{2}{P}} \cos(2\pi\alpha\beta/P) \quad (\text{D.10})$$

$$C_{\alpha \frac{P}{2}} = \sqrt{\frac{1}{P}} (-1)^\alpha \quad (\text{D.11})$$

$$C_{\alpha\beta > \frac{P-2}{2}} = \sqrt{\frac{2}{P}} \sin(2\pi\alpha\beta/P) \quad (\text{D.12})$$

The transformation in normal modes is given by

$$\tilde{\mathbf{q}} = \mathbf{C}\mathbf{R} \quad (\text{D.13})$$

Here it is useful to split H_P into a free and a potential part

$$H_P = H_P^0 + \sum_{\alpha}^P V(R_{\alpha}) \quad (\text{D.14})$$

This splitting provides an easy way to integrate the equations of motion. As H_P^0 describes a harmonic oscillator an exact integration scheme can be applied. The normal mode representation of H_P^0 reads

$$H_P^0 = \sum_{\alpha=0}^{P-1} \left(\frac{p_{\alpha}^2}{2m} + \frac{1}{2} m \omega_{\alpha}^2 \tilde{q}_{\alpha}^2 \right) \quad (\text{D.15})$$

Here $\omega_{\alpha} = 2\omega_P \sin(\alpha\pi/P)$ are the eigenfrequencies of the ring polymer. One way to integrate the equation is by using the following algorithm:

$$p_{\alpha} - \frac{\Delta t}{2} \frac{\partial V}{\partial R_{\alpha}} \rightarrow p_{\alpha} \quad (\text{D.16})$$

$$\mathbf{C}\mathbf{p} \rightarrow \tilde{\mathbf{p}}, \quad \mathbf{C}\mathbf{R} \rightarrow \tilde{\mathbf{q}} \quad (\text{D.17})$$

$$\begin{pmatrix} \cos(\omega_{\alpha}\Delta t) & -M\omega_{\alpha}\sin(\omega_{\alpha}\Delta t) \\ 1/M\omega_{\alpha}\sin(\omega_{\alpha}\Delta t) & \cos(\omega_{\alpha}\Delta t) \end{pmatrix} \begin{pmatrix} \tilde{p}_{\alpha} \\ \tilde{q}_{\alpha} \end{pmatrix} \rightarrow \begin{pmatrix} \tilde{p}_{\alpha} \\ \tilde{q}_{\alpha} \end{pmatrix} \quad (\text{D.18})$$

$$\mathbf{C}\tilde{\mathbf{p}} \rightarrow \mathbf{p}, \quad \mathbf{C}\tilde{\mathbf{q}} \rightarrow \mathbf{R} \quad (\text{D.19})$$

$$p_{\alpha} - \frac{\Delta t}{2} \frac{\partial V}{\partial R_{\alpha}} \rightarrow p_{\alpha} \quad (\text{D.20})$$

D Thermostats

This algorithm takes advantage of the splitting of the Hamiltonian in H_P^0 and V . First, the momenta are evolved under the influence of the potential Hamiltonian V , after transforming into the normal mode representation momenta and position are evolved under the influence of the free Hamiltonian H_P^0 , and after transforming back the momenta are again evolved under the influence of the potential Hamiltonian. This is essential for a generalization of the velocity Verlet algorithm. To efficiently sample the canonical ensemble one can introduce further steps to the algorithm before the first and after the last step. These steps are

$$\mathbf{C}\mathbf{p} \rightarrow \tilde{\mathbf{p}} \quad (\text{D.21})$$

$$c_1^\alpha \tilde{p}^\alpha + \sqrt{\frac{M}{\beta_P}} c_2^\alpha \xi^\alpha \quad (\text{D.22})$$

$$\mathbf{C}\tilde{\mathbf{p}} \rightarrow \mathbf{p} \quad (\text{D.23})$$

$$c_1^\alpha = e^{-(\Delta t/2)\gamma^\alpha} \quad (\text{D.24})$$

$$c_2^\alpha = \sqrt{1 - (c_1^\alpha)^2} \quad (\text{D.25})$$

This is called a path integral Langevin equation (PILE) thermostat [167] and is based on a combination of a Langevin thermostat with the velocity Verlet algorithm to sample the classical canonical ensemble. The reason for formulating the thermostat in the normal mode representation, is that the Langevin dynamics is that of uncoupled harmonic oscillators. Accordingly, the friction term $\gamma = 1/\tau$ can be determined analytically:

$$\gamma^{\alpha>0} = 2\omega_\alpha \quad (\text{D.26})$$

$$\gamma^0 = \frac{1}{\tau_0}. \quad (\text{D.27})$$

For the centroid mode $\alpha = 0$ a special friction constant $1/\tau_0$ needs to be defined since $2\omega_0 = 0$. While a friction constant determined using H_P^0 is not exact, it is still a good approximation since the ring-polymer mode usually vibrates at much higher frequencies than the modes of the physical system. However, in many cases, it is advantageous to attach a stochastic velocity rescaling thermostat, as described in App. D.1.3, to the centroid mode with yields the PILE-g thermostat.